

Risk-based Supervisory Guidance for Detect and Avoid involving Small Unmanned Aircraft Systems

by

© Scott Xiang Fang

A thesis submitted to the
School of Graduate Studies
in partial fulfillment of the requirements for the degree of
Doctor of Philosophy

Faculty of Engineering & Applied Science
Memorial University of Newfoundland

March 2018

St. John's

Newfoundland

Dedicated to my family

Abstract

A formidable barrier for small Unmanned Aircraft Systems (UAS) to be integrated into civil airspace is that small UAS currently lack the ability to Detect and Avoid (DAA) other aircraft during flight operations; however, this ability is an essential part of regulations governing the general operation of aircraft in civil airspace. In this way, the research described is focused on achieving an equivalent level of safety for small UAS as manned aircraft in civil airspace.

A small UAS DAA system was proposed to guide small UAS to detect nearby traffic, identify hazards, assess collision risks, perform mitigation analyses, and choose appropriate maneuvers to avoid potential collisions in mid-air encounters. To facilitate system development and performance evaluation, the proposed DAA system was designed and implemented on a fast-time simulation-based analysis platform, on which a set of quantifiable analysis metrics were designed for small UAS to improve situation awareness in hazard identification and collision risk assessment; and a learning-based Smart Decision Tree Method (SDTM) was developed to provide real-time supervisory DAA guidance for small UAS to avoid potential collisions in mitigation analysis. The theoretical research achieved was also integrated into an effort to implement an Automatic Collision Avoidance System (ACAS) to verify the short range DAA performance for small UAS in the visual-line-of-sight flight tests performed at the RAVEN test site in Argentina, NL.

Acknowledgments

I will begin by thanking my supervisor, Dr. Siu O’Young, who suggested this as my research topic, who allowed me complete freedom to try ideas and be essentially self-directed, and who gave support when it was needed. Acknowledgement must also be given to Dr. Luc Rolland for his guidance and support of my research in the last two years of completing my thesis.

I wish to show my appreciation to my colleagues and friends in the RAVEN project, Dilan Amarasinghe, Gayan Gamage, Jon Stevenson, Jesse Ross-Jones, Kevin Murrant, Yu Liu, Robert MacIsaac, Jordan Peckham, Dilhan Balage, Stephen Crewe, Noel Purcell, Brendan Harvey, Iryna Borshchova, Yake Li, Sam Sangsueng Lee, Oihane Cereceda Cantarelo, Carl Thibault, Chris Rouse, Bruno Miranda Artacho, Reza Shahidi and others, for the discussions and suggestions at various stages of the work.

I would also like to extend my thanks to the Supervisory Committee, and the Examination Committee, for their comments and feedback which have contributed to the end result of this research effort.

This work would not have been completed without the support from my parents, my wife and my daughter who were always there to accentuate the positive side of graduate studies.

Financial support from the Atlantic Innovation Fund and from the Natural Sciences and Engineering Research Council (NSERC) of Canada is greatly acknowledged.

Contents

Abstract	iii
Acknowledgments	iv
List of Tables	xi
List of Figures	xiii
List of Acronyms	xix
1 Introduction	1
1.1 Background	1
1.2 Problem Discussion	4
1.3 Perspectives and Scope	6
1.3.1 DAA History	6
1.3.2 DAA Scope	8
1.4 Contributions	9
1.5 Organization	13
2 Background and Related Work	14
2.1 Detection Sensor Technologies	14
2.1.1 Cooperative Sensors	15

2.1.1.1	ATC Transponder	15
2.1.1.2	TCAS	16
2.1.1.3	ADS-B	17
2.1.2	Non-cooperative Sensors	19
2.1.2.1	Passive Sensors: EO/IR Cameras and Acoustic Sensors	19
2.1.2.2	Active Sensors: Radar and Lidar	20
2.1.3	Summary of Sensor Performance	22
2.2	DAA Terminologies	23
2.2.1	Encounter Environment	23
2.2.2	DAA Timeline	24
2.2.3	DAA Parameters	25
2.3	Related Work	29
2.3.1	Bounded initial conditions and transitions for non-cooperative encounters in low altitude airspace	29
2.3.2	Size of encounter cylinder	30
2.3.3	Aircraft model for encounter generation	31
2.3.4	Implementation of encounter generation	33
2.4	Summary	36
3	Detection and Tracking	37
3.1	Introduction	38
3.2	Mathematical Models for Sensor Measurement	39
3.2.1	Aircraft positions from ADS-B	39
3.2.2	Aircraft positions from ground portable radar	40
3.3	Mathematical Models for Target Tracking	42
3.4	Implementation for Sensor Measurement and Target Tracking	45

3.4.1	Sensor measurement errors	46
3.4.2	Matrices initialization for EKF implementation	49
3.4.3	Results for EKF target tracking with measurement errors	51
3.5	Summary	53
4	Hazard Identification	54
4.1	Introduction	54
4.2	Mathematical Definitions for Mid-Air Encounters	55
4.3	Methodology for Hazard Identification	58
4.4	Implementation for Hazard Identification	59
4.4.1	Aircraft trajectory generation in the wind	61
4.4.2	Algorithms to determine Well Clear Alerting Threshold (WCAT) and Collision Avoidance Alerting Threshold (CAAT) boundaries	62
4.4.3	Impact of WCAT and CAAT boundaries on wind uncertainties	66
4.5	Summary	72
5	Risk Assessment	73
5.1	Introduction	74
5.2	Severity Metrics for Risk Assessment	76
5.2.1	Penetration risk level	77
5.2.2	Range risk level	82
5.3	Implementation Methodology	84
5.4	Risk Assessment Performance Analysis	88
5.4.1	Head-On	89
5.4.2	UA Overtaken	91
5.4.3	UA Overtaking	92
5.4.4	Left Oblique UA Overtaking	94

5.4.5	Left-Converging Traffic	95
5.5	Summary	97
6	Mitigation Analysis	98
6.1	Introduction	99
6.2	Mitigation Strategy	101
6.2.1	Self-separation	102
6.2.1.1	Maneuvering knowledge learning	104
6.2.1.2	Smart decision tree method	110
6.2.2	Collision avoidance	116
6.2.2.1	Horizontal maneuvering strategy in the three-dimensional evasive maneuvering algorithm	116
6.2.2.2	Vertical maneuvering strategy in the three-dimensional evasive maneuvering algorithm	119
6.3	Performance Evaluation	120
6.3.1	Risk ratio definitions	120
6.3.1.1	Self-separation performance	122
6.3.1.2	Collision avoidance performance	122
6.3.2	Performance documentation	123
6.4	Encounter Mitigation Performance Analysis	124
6.5	Summary	135
7	Experimental Work	136
7.1	RAVEN Unmanned Aircraft	137
7.1.1	Giant Big Stik Unmanned Aircraft	137
7.1.2	Vector-P Unmanned Aircraft	138
7.2	RAVEN Flight Test Site	139

7.3	UA Synchronization for Mid-air Encounters	140
7.3.1	System Schematic for UA 4D Synchronization	141
7.3.2	System Design for UA 4D Synchronization	142
7.3.3	Test Results for UA 4D Synchronization	143
7.4	Development of ADS-B Based Cooperative ACAS	144
7.4.1	System Design for ACAS	145
7.4.2	Results for Initial ACAS Flight Tests	145
7.4.3	Hardware-in-loop ACAS Testing Platform	148
7.4.4	ACAS HIL Test Results	149
7.5	Ground Portable Radar for Non-Cooperative Traffic	151
7.5.1	Test Procedure	152
7.5.2	Test Results	153
7.6	Beyond Visual Line of Sight (BVLOS) Flight Tests	156
7.6.1	System Configuration for BVLOS UAS	157
7.6.2	Link-loss Failure Action Plan for BVLOS Flights	158
7.6.3	BVLOS Flights	159
7.7	Summary	160
8	Conclusion and Future Work	161
8.1	Contributions	161
8.1.1	Modelling	162
8.1.2	Analysis Platform	162
8.1.3	Situation Awareness	163
8.1.4	Mitigation Solutions	163
8.1.5	Performance Ranking	164
8.1.6	Implementation and Flight Tests	164

8.2 Future Work	165
Bibliography	169

List of Tables

1.1	List of publications	12
2.1	Summary of sensor performance	22
3.1	Minimum requirement of radar track accuracy for high-priority traffic [1]	49
5.1	Description for P_{risk} (<i>Penetration</i>) value range	79
5.2	Collision Risk Ranking Table	85
5.3	Range Risk Ranking Table	87
5.4	Summary of encounter geometries [2]	88
5.5	Analysis results for encounters on the head-on geometry.	91
5.6	Analysis results for encounters on the UA overtaken geometry.	92
5.7	Analysis results for encounters on the UA overtaking geometry.	93
5.8	Analysis results for encounters on the left oblique UA overtaking geometry.	95
5.9	Analysis results for encounters with traffic on the left-converging geometry.	96
6.1	UA horizontal maneuvering options	103
6.2	Datasets in the UA maneuvering knowledge base	104
6.3	A sample database range query result from the knowledge base.	106
6.4	Maneuvering options statistics	106
6.5	List of sample analysis results from eight suggested maneuvering options on a three-level decision tree in a head-on encounter.	114

6.6	Vertical maneuvering strategy	119
6.7	Set and subset for the risk ratio analysis.	121
6.8	Datasets documented for further performance analysis	123
6.9	Maneuvering options for the encounter with left-converging traffic by a three-level decision tree.	125
6.10	Maneuvering options for the left oblique UA overtaking encounter by the top three-level decision tree.	127
6.11	Maneuvering options for the left oblique UA overtaking encounter by the expanded six-level decision tree (for Option 6 and 8 on the top three-level decision tree).	128
6.12	Mitigation performance comparison diagrams	129
7.1	Giant Big Stik aircraft specifications.	138
7.2	Vector-P aircraft specifications.	139
7.3	Zeus ground portable radar specifications and settings.	152
7.4	Summary of radar test flight plan.	153
7.5	Link-loss failure cases in BVLOS flights.	158

List of Figures

1.1	A typical system diagram for UAS [3].	2
1.2	RTCA special committee research timeline.	7
1.3	Diagram for DAA and CA regions in a mid-air encounter.	8
1.4	Block diagram for the fast-time simulation based analysis platform.	10
2.1	Antennas of a typical ground surveillance radar system for ATC [4].	15
2.2	TCAS direction antenna [5].	16
2.3	TCAS protection volume (modified from [6]).	17
2.4	ADS-B surveillance configuration diagram [7].	18
2.5	Encounter cylinder diagram.	23
2.6	Near Mid-Air Collision (NMAC) cylinder diagram.	24
2.7	Well Clear (WC) cylinder diagram.	24
2.8	DAA timeline diagram [8].	25
2.9	Aircraft positions in the three-dimensional space [9].	26
2.10	Block diagram for the fast-time simulation based analysis platform.	29
2.11	Feature histograms of recorded radar data based on 193 million samples [10].	30
2.12	A dynamic-size encounter cylinder in the three-dimensional space.	31
2.13	A pair of sample encounter trajectories generated by the uncorrelated encounter model (legend: blue for UA and green for traffic).	33

2.14	Feature histograms of five million sample encounters simulated on the fast-time simulation platform.	35
3.1	Block diagram for the fast-time simulation based analysis platform. .	38
3.2	Radar polar and Cartesian coordinates diagram [11].	41
3.3	Implementation diagram for sensor measurement and target tracking modules.	46
3.4	Aircraft measured positions with uncertainties during mid-air encounters.	47
3.5	Comparisons for trajectories estimated by Extended Kalman Filter (EKF) on the horizontal and vertical planes.	51
3.6	A pair of sample encounter trajectories estimated by EKF through ADS-B measurement. (Legend: blue for simulated UA trajectory, green for simulated traffic true trajectory, and magenta for estimated traffic trajectory.)	52
3.7	A pair of sample encounter trajectories estimated by EKF through ground portable radar measurement. (Legend: blue for simulated UA trajectory, green for simulated traffic true trajectory, and magenta for estimated traffic trajectory.)	52
4.1	Block diagram for the fast-time simulation based analysis platform. .	54
4.2	Layered encounter model of the airspace nearby the UA.	55
4.3	NMAC cylinder diagram.	56
4.4	WC cylinder diagram.	56
4.5	Layered encounter zones of the UA.	58
4.6	Sample turning trajectories for 75 kt UA under 20 kt winds in various wind directions from 0° to 360° every 45° by 20-second 2g left level turns (6°/sec).	60

4.7	Aircraft trajectory generation in the wind.	61
4.8	A web structure for Monte Carlo simulations to determine WCAT and CAAT boundaries (bearing in deg and range in nmi).	62
4.9	An example of 20-second gusty wind pattern with wind velocity jumps [12].	66
4.10	Range-based WCAT diagrams with 20 kt gusty winds in eight directions (bearing in deg, range in nmi, UA at 75 kt vs. traffic at various airspeeds).	67
4.11	Summarized range-based WCAT diagrams (bearing in deg, range in nmi, UA at 75 kt vs. traffic at various airspeeds).	68
4.12	Threshold changing ratio diagrams for the impact of WCAT boundaries on wind uncertainties (UA at 75 kt vs. traffic at various airspeeds).	69
4.13	Range-based CAAT diagrams with 20 kt gusty winds in eight directions (bearing in deg, range in nmi, UA at 75 kt vs. traffic at various airspeeds).	69
4.14	Summarized range-based CAAT diagrams (bearing in deg, range in nmi, UA at 75 kt vs. traffic at various airspeeds).	70
4.15	Threshold changing ratio diagrams for the impact of CAAT boundaries on wind uncertainties (UA at 75 kt vs. traffic at various airspeeds).	71
5.1	Block diagram for the fast-time simulation based analysis platform.	73
5.2	Benign momentary nick at the LoWC boundary and prolonged, severe LoWC [2].	74
5.3	A sample FG Norm operation diagram [2].	78
5.4	Diagrams of $\bar{P}_{risk}(\tau_{mod})$, $\bar{P}_{risk}(HMD)$, and $\bar{P}_{risk}(V_s)$ function curves.	80
5.5	Diagrams of $P_{risk}(Penetration)$ for co-altitude encounters.	81
5.6	Diagrams of $P_{risk}(Penetration)$ without $P_{risk}(\tau_{mod})$	82
5.7	Diagrams of $P_{risk}(Range)$ function curves.	83
5.8	Diagrams of P_{risk} calculations based on sensor measurements.	84

5.9	P_{risk} collision risk analysis for a head-on encounter.	90
5.10	P_{risk} collision risk analysis for a UA overtaken encounter.	92
5.11	P_{risk} collision risk analysis for a UA overtaking encounter.	93
5.12	P_{risk} collision risk analysis for left oblique UA overtaking encounters.	94
5.13	P_{risk} collision risk analysis for a left-converging traffic encounter. . . .	96
6.1	Block diagram for the fast-time simulation based analysis platform.	98
6.2	Diagram for risk-based horizontal maneuvering options.	103
6.3	Example for using a policy network to provide turning guidance in a mid-air encounter.	108
6.4	Sample policy network diagrams for UA maneuvering options in various velocities and wind conditions (UA: velocity at 75 kt and heading to the north; Legend: negative indexes for left turns in cool colors and positive indexes for right turns in warm colors).	109
6.5	An execution of a decision tree with choice points at time interval Δt .	111
6.6	Trajectory deviation diagram (modified from [2]).	113
6.7	Sample mitigation analysis in a head-on encounter.	114
6.8	Horizontal maneuvering strategies in the three-dimensional evasive maneuvering algorithm.	116
6.9	Evasive maneuvering strategy in quadrant I.	117
6.10	Evasive maneuvering strategies in quadrant II and quadrant III	118
6.11	Evasive maneuvering strategy in quadrant IV	118
6.12	Mitigation risk ratio analysis diagram.	121
6.13	Mitigation performance analysis for a left-converging traffic encounter.	125
6.14	Mitigation performance analysis for a left oblique UA overtaking en- counter.	126

6.15	Mitigation performance analysis of LoWC risk ratios in UA self-separation.	131
6.16	Sample diagrams for unresolved LoWC encounters in risk ratio analysis due to system delays.	132
6.17	Mitigation performance analysis of NMAC risk ratios in UA collision avoidance.	133
6.18	Sample diagrams for unresolved NMAC encounters in risk ratio analysis due to system delays.	134
7.1	UAS operation crew members and the GCS.	136
7.2	Giant Big Stik aircraft take-off and flying.	137
7.3	Vector-P aircraft take-off and flying.	139
7.4	The RAVEN project test site in Argentia, NL.	140
7.5	UA 4D synchronization system schematic diagram	141
7.6	UA 4D synchronization system design diagram.	142
7.7	UA 4D synchronization testing results.	143
7.8	AWSAS Box Diagram.	144
7.9	Cooperative ADS-B based ACAS schematic diagram.	145
7.10	Initial flight tests for ACAS.	146
7.11	Initial test results for ACAS.	147
7.12	Encounter pictures in ACAS flight tests.	147
7.13	The HIL ACAS testing platform schematic diagram.	148
7.14	The HIL ACAS testing platform in the lab.	149
7.15	Diagrams for unresolved NMACs in Quadrant I in ACAS HIL tests.	150
7.16	Zeus ground portable radar assembly [13].	151
7.17	Witless Bay Line radar test flight plan on the map.	152

7.18	Results for the approaching maneuvers [14]. Distances are relative to the radar, bearings are relative to the 80° radar pointing angle, the range rings interval is 1 nmi and the scan spoke interval is 15°.	153
7.19	Results for the crossing maneuvers [14]. Distances are relative to the radar, bearings are relative to the 80° radar pointing angle, the range rings interval is 1 nmi and the scan spoke interval is 15°.	154
7.20	Results for the circular maneuver [14]. Distances are relative to the radar, bearings are relative to the 80° radar pointing angle, the range rings interval is 1 nmi and the scan spoke interval is 15°.	155
7.21	Map for the BVLOS operating area in Argentina, NL.	156
7.22	System configuration for BVLOS UAS.	157
7.23	BVLOS flights at the RAVEN project test site in Argentina, NL. . . .	159
8.1	Diagram for three major contributions in this thesis.	162
8.2	Diagram for future recommendations.	167

List of Acronyms

ACAS Automatic Collision Avoidance System.

ADS-B Automatic Dependent Surveillance-Broadcast.

ATC Air Traffic Control.

BVLOS Beyond Visual Line of Sight.

C2 Command and Control.

CA Collision Avoidance.

CAAT Collision Avoidance Alerting Threshold.

CAHM Collision Avoidance Horizontal Maneuvering algorithm.

COA Certificates of Waiver or Authorization.

CPA Closest Point of Approach.

DAA Detect and Avoid.

DMOD Distance MODification.

EKF Extended Kalman Filter.

EO Electro-Optic.

EPU Estimated Position Uncertainty.

FAA Federal Aviation Administration.

FPE Flight Performance Envelope.

GA General Aviation.

GCS Ground Control Station.

HIL Hardware-In-Loop.

HMD Horizontal Miss Distance.

IR Infrared Radiation.

LoWC Loss of Well Clear.

MC Monte Carlo.

MOPS Minimum Operational Performance Standards.

NAS National Airspace System.

NMAC Near Mid-Air Collision.

PIC Pilot-In-Command.

PSR Primary Surveillance Radar.

RTCA Radio Technical Commission for Aeronautics.

SDTM Smart Decision Tree Method.

SFOC Special Flight Operations Certificates.

SLoWC Severity of Loss of Well Clear.

SSI Separation Severity Index.

SSR Secondary Surveillance Radar.

SWaP Size, Weight, and Power.

TC Transport Canada.

TCAS Traffic Collision Avoidance System.

UA Unmanned Aircraft.

UAS Unmanned Aircraft Systems.

US United States.

VLOS Visual Line of Sight.

VMD Vertical Miss Distance.

WC Well Clear.

WCAT Well Clear Alerting Threshold.

WCPI Well Clear Penetration Integral.

Chapter 1

Introduction

1.1 Background

The history of UAS can be traced back to World War II as a target-practice drone [15]. With evolution and development in the last seventy years, UAS have been largely applied for military purposes from aerial reconnaissance to active target spotting [16], and have become an indispensable part of modern warfare. At the same time, UAS have also become more and more popular for both civilian and commercial applications. For example, UAS have recently been used for environmental monitoring and measurements, emergency response, homeland security, precision agriculture, land management, infrastructure monitoring, and commercial applications such as aerial photography and transportation of goods and post [3, 17].

As new entrants to the aviation industry, UAS are more than just aircraft; they are a comprehensive control system, which consists of several distinct parts described in Fig. 1.1: the flying air vehicle with the systems onboard (i.e., the Unmanned Aircraft (UA)), the Ground Control Station (GCS) that the pilot uses to operate the UA, and the Command and Control (C2) link between the air and the ground [18].

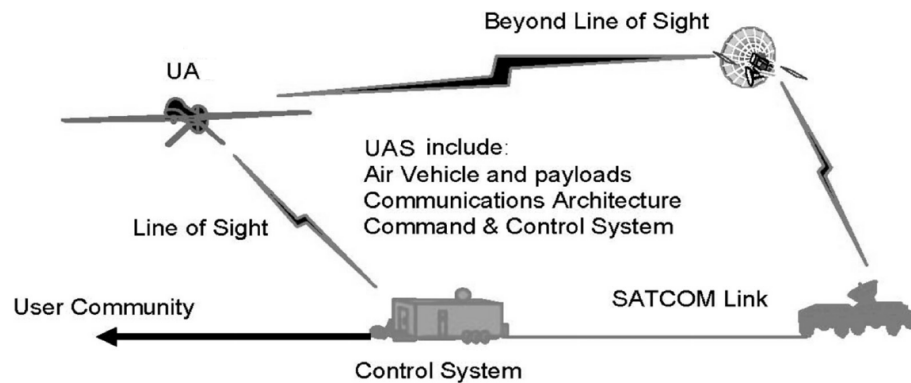


Figure 1.1: A typical system diagram for UAS [3].

On manned aircraft, human pilots are trained to communicate with and follow instructions from Air Traffic Control (ATC) on the ground, check equipment on the aircraft, and look through the windows of the aircraft to detect collision threats and maneuver to avoid other aircraft [19]. However, UAS are lacking this critical ability to Detect and Avoid (DAA) other aircraft during flight operations.

The other significant issue for operating UAS is the fact that the UA pilots control the UA in a remote manner, typically relying on radio frequency (RF) and/or satellite communications to establish a C2 link between the GCS and the UA. For safe operations of UAS, the C2 link has to be robustly, reliably, and redundantly established. When the C2 link does fail, the UA should perform predictable and acceptable “lost link” procedures similar to manned aircraft autopilot systems [18].

For these safety concerns, civil aviation authorities like the Federal Aviation Administration (FAA) in the United States (US) and Transport Canada (TC) in Canada have not allowed UAS to be integrated into civil airspace with manned aircraft. Currently, they allow UAS only in limited operational areas in civil airspace under Certificates of Waiver or Authorization (COA) in the US and Special Flight Operations Certificates (SFOC) in Canada.

As industry pushes for the increased use of more UAS, both the FAA and TC have committed to modifying the current regulations. As to the airworthiness and flight performance, they have decided to require UAS to be certified as compliant aircraft systems according to the existing standards and regulations for manned aircraft systems. As to the C2 link, they have published the UAS “Lost Link” procedures during UAS operations [20,21] and have issued a number of standards and certification processes for the link reliability requirements, as suggested by the Radio Technical Commission for Aeronautics (RTCA) Special Committee SC-228 (advisory committee of the FAA) [2]. As to the DAA systems, they have not set forth or issued any standards to guide the certification process of DAA systems for UAS because DAA systems are still under development. To help the industry gain operational experience and encourage researchers and system developers to solve the problems along the road to certify DAA systems, aviation authorities have proposed two near-term DAA solutions for integrating UAS into civil airspace:

1. **Large UAS** are required to have installed the same sensors as manned aircraft like airborne radar, Traffic Collision Avoidance System (TCAS), and Automatic Dependent Surveillance-Broadcast (ADS-B) to provide an equivalent level of safety as manned General Aviation (GA) aircraft [18]. Once equipped, processed sensor information is transmitted from the UA to the GCS, where the Pilot-In-Command (PIC) analyzes the guidance from the DAA systems and the data from different sensors, and makes final decisions on whether maneuvers are needed to avoid other surrounding traffic.
2. **Small UAS** are required to have installed newly-developed small, light, and low-power versions of airborne sensors or portable ground-based sensors for safe operations due to their limitations on Size, Weight, and Power (SWaP).

Once equipped, processed sensor information is transmitted from the UA to the GCS, where the PIC analyzes the guidance from the newly-developed DAA systems and the data from different sensors, and makes final decisions on whether maneuvers are needed to avoid other surrounding traffic.

1.2 Problem Discussion

The first solution for large UAS, discussed in Section 1.1, is a straightforward starting point for integrating UAS into civil airspace with other manned GA aircraft in the near future, as those DAA systems have already been proven and certified on manned aircraft. The remaining challenges are therefore to modify the current regulations and operational procedures in civil airspace, and to have additional training courses for air traffic controllers and pilots of large UAS and manned aircraft.

However, implementing the second near-term DAA solution for small UAS will be much harder for researchers and engineers in the UAS industry than implementing the first solution for large UAS, since there are no certified DAA systems that would allow small UAS to achieve the equivalent level of safety as manned GA aircraft. In addition, small UAS aerodynamic characteristics are very different from manned aircraft. The collision avoidance solutions for manned aircraft will not be suitable for small UAS. Generally, small UAS operate at a slow cruise airspeed; thus, the turning trajectories of small UAS and the time needed to complete turns are greatly affected by the wind conditions (i.e., wind speed and wind direction) during a level maneuver, whereas manned aircraft operate faster and are less affected by the wind during a turn. To reflect this reality, new specific collision avoidance solutions should be designed and implemented in the new DAA systems for small UAS to avoid potential collisions with other nearby mid-air traffic. Moreover, any such DAA systems should be evaluated

and qualified before they can be certified and deployed, either on the UA or on the ground, for small UAS to achieve an equivalent level of safety as manned GA aircraft.

Both the FAA and TC have established a number of restricted areas in civil airspace as test sites for carrying out system developments, performing UAS tests, and gathering operational data for the future integration of UAS into civil airspace with manned GA aircraft. It is true that field flight tests are absolutely necessary for the evaluation and certification of UAS and DAA systems; however, field tests are not cost-effective, and only limited cases (encounter geometries) can be carried out during system testing and verification. Another method, which is less expensive but still time-consuming, is to have these tests run on the Hardware-In-Loop (HIL) simulator. This method indeed is a very good solution for the training of pilots and air traffic controllers as well as for research on human factors in UAS operations. In addition to these two methods for the development of DAA systems, the Monte Carlo (MC) simulation method is also often used for risk-quantitative analysis and decision-making to handle uncertainty and variability of mid-air encounters in civil airspace. This method checks all possible initial conditions of encounters and researched environments, evaluates outputs of DAA systems from all the possible collision avoidance decisions, and assesses the risk levels and the performance of the collision decisions. For more accurate and reliable results from the analysis, the MC simulation generally requires the larger simulation sizes, which would be computationally expensive and inefficient [22].

As for system development and testing, it is crucial to have a fast performance evaluation method. The system should be tested and evaluated as quickly and comprehensively as possible after the initial design, and the problems found in the evaluation should be fed back to the design again for further modifications and updates, so that the design and implementation could be fine-tuned after a couple of iterations in a short time period. However, these three methods discussed in this section require a

long time (process turnaround time) to evaluate the newly-developed system, and only limited cases can be tested during flight tests in the field or on the HIL simulator, which will not be sufficient to obtain approvals or certifications from aviation authorities.

1.3 Perspectives and Scope

This thesis extends the recently published RTCA SC-228 Minimum Operational Performance Standards (MOPS) for DAA Systems [2] by filling the technology gaps identified in the current Phase I MOPS, and helps formalize the future Phase II MOPS for small UAS. Later, both FAA and Transport Canada will incorporate the RTCA recommendations for the future rule-making to approve the integration of small UAS into civil airspace.

1.3.1 DAA History

To assure the safe, efficient, and compatible operation of UAS with other manned GA aircraft in civil airspace, RTCA Special Committee SC-203 was established in 2004, to provide recommendations and technical standards for FAA to make policy, program, and regulatory decisions [23]. The SC-203 has developed and documented guiding principles for UAS integration and operations; however, due to disagreement on different aircraft dynamics among the great variety of UAS used in civil airspace [8], the SC-203 could not formalize a UAS MOPS for FAA to quantitatively determine the safety boundaries (e.g., collision avoidance alerting boundary and self-separation alerting boundary). In 2013, as learned from overly ambitious objectives in the SC-203, RTCA decided to assign UAS research tasks specifically into two separate special committees: a new SC-228 (to develop the MOPS for DAA equipment and C2

Data Link solutions) [24], and a previous SC-147 (to develop the MOPS for Collision Avoidance (CA) equipment, e.g., ACAS Xu) [25].

In the SC-228, the research focuses on long-range DAA in two phases (Phase I for large UAS for mostly transiting operations in Class A airspace, and Phase II extends to include small UAS and covers extended operations in Class G airspace) [26]. The RAVEN project¹ joined the SC-203 in 2009 and then moved to the new SC-228 in 2013. As shown in Fig. 1.2, after a four-year concentrated effort, the Phase I MOPS has been formalized and published in May, 2017 [2], in which a DAA Well Clear (WC) boundary is quantitatively determined for the UAS DAA systems regardless of aircraft dynamics, to replace previous subjective WC boundaries determined by human pilots [27]. Based on this WC boundary, a series of DAA research for small UAS has been carried out in this thesis, such as Remaining Well Clear (RWC) and avoiding Loss of Well Clear (LoWC). In addition, the SC-147 (established for TCAS in 1980) works on a new Aircraft Collision Avoidance System for NextGen (ACAS Xa) to replace TCAS II on the current manned aircraft (expected ACAS Xa MOPS completion date in December 2018), and the ACAS Xu MOPS for UAS is scheduled to be completed in 2020 [25].

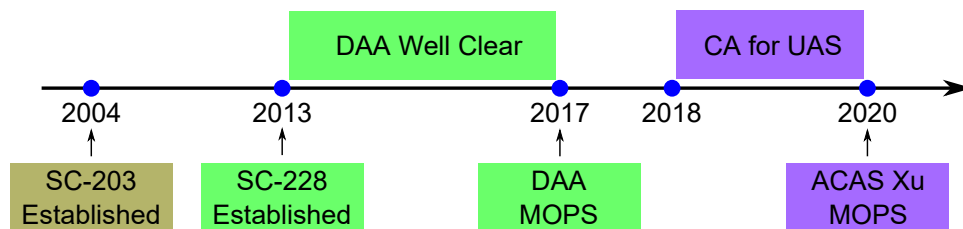


Figure 1.2: RTCA special committee research timeline.

¹The RAVEN project is based at Memorial University, St. John's, NL, Canada, and their main research objective is to develop intelligent DAA systems to allow small UAS to share the same airspace with manned aviation.

1.3.2 DAA Scope

As described in Section 1.1, to enable near-term UAS access to civil airspace, RTCA recommends to implement DAA systems for UAS to reduce the rate of Loss of Well Clear with other manned aircraft in civil airspace, and further to ensure the rate of unmitigated Near Mid-Air Collision (NMAC) lower to an accepted risk level for the UAS integration approval from aviation authorities.

In response, the research is focused on the long-range DAA for small UAS² as shown in Fig. 1.3, to provide DAA guidance for the PIC to make final decisions on whether maneuvers are needed to avoid LoWCs with other surrounding traffic. With currently available sensor technologies, such as small size, light weight, and low power airborne ADS-B and ground portable radar, a DAA system can provide warning alerts more than 60 seconds before potential LoWCs, which allows the PIC in the DAA loop to identify risks and make maneuvering decisions.

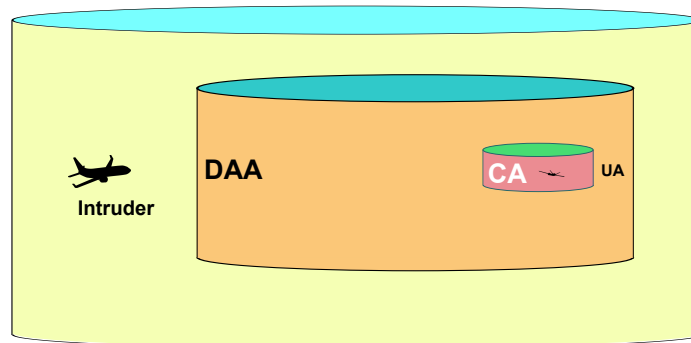


Figure 1.3: Diagram for DAA and CA regions in a mid-air encounter.

On the other hand, CA maneuvers are typically initiated 10 to 20 seconds before potential NMACs, which precludes the PIC in the CA loop when taking into account

²It should be clarified that small UAS operations in this thesis mainly refer to those unmanned aircraft operations in Class G uncontrolled airspace at the level of 2000 ft to 3000 ft with oncoming GA aircraft as intruders during mid-air encounters.

the non-removable system delays in 5 to 15 seconds [28]. Furthermore, CA systems on UA require to measure the distance to approaching traffic accurately for NMAC prediction,³ and to support resolution advisory (RA) coordination with existing CA systems on manned aircraft [2]. The former requirement inevitably prevents the integration of small UAS into civil airspace in the near future. For this reason, this thesis focuses on DAA research to help integrate small UAS into civil airspace in the near future (except using CA in Chapter 6 as a reference).

In general, CA is a last resort to avoid a potential NMAC when an aircraft WC boundary is violated. To accomplish this task, ACAS Xu will combine TCAS, airborne radar, ADS-B, and electro-optics (EO) and infrared (IR) sensors to carry out sensor fusion and collision avoidance [29]. Up to date, this will rely on a to-be-defined module named Nucleus in the future [30,31]. In addition, specifically for small UAS, miniaturization of sensors suite and aircraft dynamics for different UA and traffic have to be accounted in the development of future ACAS Xu. As a result, CA research is currently beyond the scope of this thesis.

1.4 Contributions

As required for the near-term integration of small UAS into civil airspace, it is necessary to have a comprehensive and efficient solution for the development of DAA systems of small UAS. As shown in Fig. 1.4, a fast-time software simulation platform is therefore proposed and developed to facilitate the development of DAA systems, to test and evaluate these newly-developed systems, and to qualify their DAA mitigation performance over millions of simulated mid-air encounters in civil

³Due to delays from sensor measurements and data communications, ADS-B provides traffic positions at an accuracy of 0.2 nmi [2], thus only airborne radar currently is a mature sensor for CA systems on UA.

airspace. Moreover, along with the development of this platform, a number of new metrics are also introduced to evaluate and analyze DAA systems performance, which will produce analytical statistics to help aviation authorities prepare future standards and regulations governing routine operations of small UAS in civil airspace.

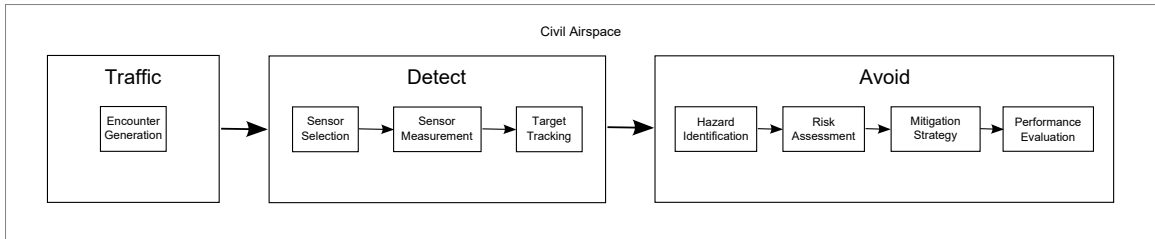


Figure 1.4: Block diagram for the fast-time simulation based analysis platform.

The contributions of this thesis are summarized as follows:

Modelling The effort on the modelling framework establishes a series of mathematical definitions and formulas to represent all the involved elements in mid-air encounters in civil airspace. These elements have been described and designed into software models such as the encounter generation model, the sensor measurement model, the target tracking model, the hazard identification model, the risk assessment model, the mitigation strategy model, as well as the performance evaluation model.

Analysis Platform A fast-time simulation-based analysis platform is developed to exercise encounter geometries, verify the performance and reliability of mitigation methods, and perform statistical analysis over millions of simulated encounters from a set of repeatable high fidelity aircraft encounters in civil airspace in a short period of time. The success of this simulation platform greatly reduces the turnaround time of the performance evaluation for DAA systems, and helps

them achieve the ultimate goal of an equivalent level of safety as human pilots on manned GA aircraft.

Situation Awareness For quantifying situation awareness during mid-air encounters, a set of time-based and range-based metrics are designed to evaluate encounter collision risks in real-time and provide normalized risk levels for oncoming air traffic [32]. More importantly, wind effects are also introduced in the mathematical analysis to determine ever-changing outer and inner safety boundaries in various wind conditions for small UAS in self-separation and collision avoidance during mid-air encounters [33]. With a decision synthesis on both collision risks and safety boundaries, an appropriate mitigation enabling time is selected for small UAS to initiate maneuvers to avoid potential collisions with other nearby traffic in civil airspace.

Mitigation Solutions During mid-air encounters, two types of mitigation solutions are proposed and designed for small UAS to provide DAA maneuvering guidance in self-separation and emergency evasive maneuvers in collision avoidance [34]. With millions of simulated mid-air encounters in civil airspace on the fast-time simulation platform, these two mitigation solutions are tested and qualified in different encounter geometries with various uncertainties on sensor measurements, wind effects and system delays from pilot decisions, command executions and aircraft aerodynamic responses. The analysis results are used to direct the development and improvement of mitigation solutions for future small UAS onboard DAA systems.

Performance Ranking For aircraft safety, the airworthiness of UAS can be evaluated and certified by existing standards and regulations for manned GA aircraft, but for DAA systems, there are no standards and regulations issued by aviation

authorities at present. Thus, a set of new analytical metrics are proposed and introduced for DAA systems to establish a performance ranking system for the integration of small UAS into civil airspace with manned GA aircraft [34]. This performance ranking system will guide researchers and system developers toward achieving the certification of newly-developed DAA systems, and help aviation authorities evaluate the risk levels of integrating small UAS into civil airspace.

Implementation and Flight Tests The theoretical approaches are integrated into an effort of implementing DAA systems to provide a safe operation environment for small UAS in civil airspace. A ground portable radar system and an ADS-B based ACAS [35] are developed and integrated (with the RAVEN team of which the author is a member) to provide the capability of detecting both cooperative and non-cooperative traffic in the surveillance volume. During system testing and qualification of DAA systems, a HIL simulator is designed and constructed for system ground tests and pilot training [36], and a four-dimensional (4D) encounter synchronization control system [37, 38] is also designed and developed for improving the efficiency of flight tests in the field.

Publications The results of this thesis are presented at two conferences [35, 37], and documented in four journal papers [32–34, 39], as well as recorded in four technical reports [36, 38, 40, 41]. The list of publications with respect to their contributions is given in Table 1.1.

Table 1.1: List of publications

Publications	[32]	[33]	[34]	[35]	[36]	[37]	[38]	[39]	[40]	[41]
Contributions										
Situation Awareness	✓	✓								
Mitigation Solutions			✓							
Performance Ranking			✓							
Implementation and Flight Tests				✓	✓	✓	✓	✓	✓	✓

1.5 Organization

The rest of this thesis is organized as follows: Chapter 2 contains a review of the literature on currently available sensor technologies that can be employed for DAA systems. It also includes related definitions and terminologies, as well as related work on DAA systems that will be discussed in the thesis for system modelling, assessment and evaluation. Chapter 3 explains the system modelling framework and begins to implement modules for the Detect System on the fast-time simulation based analysis platform. Chapter 4, Chapter 5, and Chapter 6 focus on the design and implementation of those modules for the Avoid System on the fast-time simulation based analysis platform. Chapter 4 quantifies the encounter safety boundaries in winds and completes the implementation of the hazard identification module. Chapter 5 develops a set of real-time computable collision risk assessment metrics and finishes the implementation of the risk assessment module. Chapter 6 proposes two types of mitigation solutions for small UAS in self-separation and collision avoidance to help implement the mitigation strategy module. It also introduces a set of risk-ratio metrics to implement the performance evaluation module. Chapter 7 discusses the effort on the experimental work carried out for system testing and verification. Finally, Chapter 8 summarizes the contributions to DAA research, and suggests directions for future work.

Chapter 2

Background and Related Work

This thesis is concerned with the implementation and evaluation of DAA systems for small UAS. As such, the background material contained in this chapter is of a diverse nature, encompassing elements of detection sensor technologies, aircraft encounter definitions, and DAA decision timeline and parameters. It also features related work on the high fidelity mid-air encounter model for civil airspace that will be used in the DAA analysis and evaluation throughout the modules on the fast-time simulation platform. This chapter is a brief overview of terminologies to support the design and analysis of DAA systems, and more detailed literature reviews will be given in their corresponding chapters later in the thesis.

2.1 Detection Sensor Technologies

Currently, multiple detection sensors have been used to detect mid-air hazards like nearby traffic or objects with a risk of collision on large UAS and manned aircraft. Based on the technologies employed, they can be summarized into two categories: cooperative and non-cooperative [42]. Cooperative sensors usually receive radio signals from equipment on other surrounding aircraft, such as ATC transponders, TCAS, and

ADS-B. On the other hand, non-cooperative sensors are used to detect non-cooperative traffic that have not been equipped with cooperative sensors, i.e., radar, Electro-Optic (EO) or Infrared Radiation (IR) cameras, acoustic sensors, as well as laser/light detection and ranging (lidar) systems.

2.1.1 Cooperative Sensors

2.1.1.1 ATC Transponder

A Mode A/C transponder is an avionic system that provides information about the aircraft identification (Mode A) and barometric altitude (Mode C) to the ATC Radar Beacon System (ATCRBS) on the ground and to TCAS on other aircraft, by the interrogation from the ATC Secondary Surveillance Radar (SSR) on the ground or TCAS on the other nearby aircraft [43]. Based on the travel time of the reply from the transponder and the SSR antenna pointing angle, the position of the aircraft is calculated by the SSR on the ground. Synchronized with the targets detected on the ATC Primary Surveillance Radar (PSR), air traffic controllers have a more complete picture of the surveillance area. Moreover, the identification information from a Mode A/C transponder can be used to correlate the aircraft track to its flight plan.



Figure 2.1: Antennas of a typical ground surveillance radar system for ATC [4].

Fig. 2.1 shows antennas of a typical ground radar system for ATC. The ladderlike top section is the SSR directional antenna, whereas the lower part of the assembly is the PSR antenna [44].

2.1.1.2 TCAS

TCAS provides a solution to the problem of reducing the risk of mid-air collisions between aircraft and has achieved extraordinary success in commercial aviation since 1990s [45,46]. TCAS basically is a mini version of SSR on the aircraft, which detects and tracks the surrounding transponder-equipped traffic by sending air-to-air interrogations and decoding replies from transponders on nearby traffic aircraft [47]. As a SSR, a TCAS measures the distance to an intruder by assessing the signal round-trip travel time and estimating the bearing of the intruder with a static, electronically steered four-element phased array directional antenna on the aircraft [46,47]. Two types of transponders are currently in use: Mode S and Mode A/C transponders. The main difference between them is the support of selective interrogation on Mode S transponders, which greatly reduces the likelihood of garbled or overlapping replies and frequency congestion in high density airspaces [46]. In addition, Mode S transponders have an additional data-link to coordinate collision avoidance maneuvers during mid-air encounters [46].



Figure 2.2: TCAS direction antenna [5].

TCAS is an advisory system for the pilot using three types of alerts: traffic advisory (TA), resolution advisory (RA) and clear of conflict (CC) [6]. When a TA is issued, the flight crews need to be alerted and start to search the intruder visually according to the bearing indicated on the TCAS display. If the intruder keeps approaching, a RA will be issued and the pilot will make a final decision to command the aircraft to climb or descend, and return back the previous assigned course after a CC is issued on TCAS [47]. Fig. 2.3 shows a TCAS protection volume with a RA region, a TA region, and a surveillance region around a TCAS-equipped aircraft in both horizontal and vertical directions.

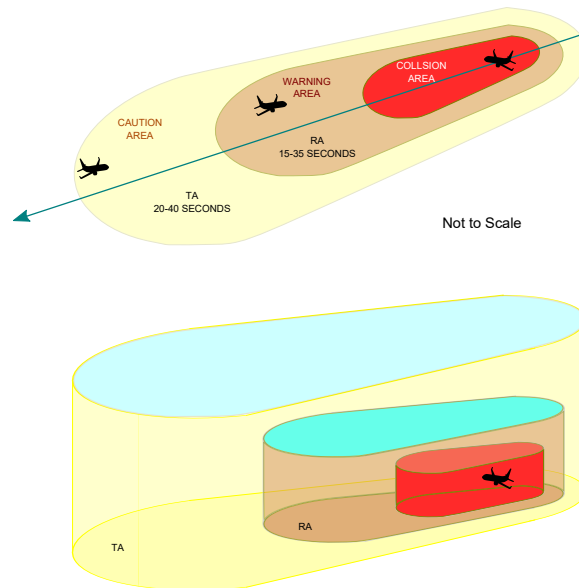


Figure 2.3: TCAS protection volume (modified from [6]).

2.1.1.3 ADS-B

As a solution for the Next Generation Air Transportation System (NextGen) in civil airspace, ADS-B combines the precise aircraft location and velocity derived from Global Positioning System (GPS) satellite signals with other data like the aircraft

identification and possibly its intent, and broadcasts this flight information to ATC and other surrounding ADS-B equipped aircraft [48]. It is designed to improve the operational capacity, safety and efficiency in civil airspace, and support ATC to gradually migrate their conventional ground-based SSR system to a satellite-based cooperative surveillance system to have more accurate and frequent surveillance services and less system maintenance cost [49].

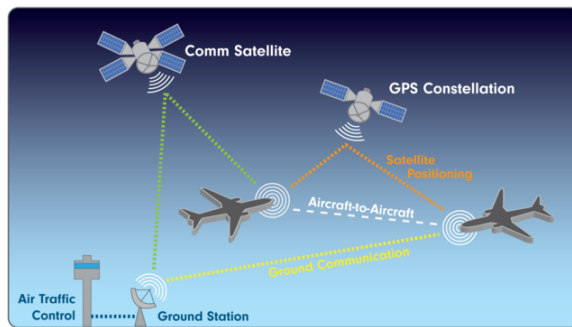


Figure 2.4: ADS-B surveillance configuration diagram [7].

For ADS-B communication, a data-link 1090 Extended Squitter (ES) at 1090MHz has been assigned internationally, which is also used by existing Mode A/C/S transponders for TCAS and SSR interrogations. Due to this potential frequency congestion on 1090 MHz, another data-link Universal Access Transceiver (UAT) at 978MHz is adopted in the US by the FAA as the second data-link for the GA aircraft operating below Flight Level (FL) 180 (18,000 ft). At the same time, this UAT data-link in the US is also used for transmitting the Ground Uplink Message from ground to air to provide weather information about aircraft operating areas [49].

As described in Fig. 2.4, all ADS-B equipped aircraft are able to detect and track other surrounding ADS-B equipped traffic automatically without interventions from pilots or air traffic controllers [50]. Although ADS-B was designed to improve the situational awareness for ATC and manned aircraft, it also becomes a feasible

cooperative DAA solution for the integration of small UAS into civil airspace because nowadays airborne ADS-B avionics have been made in small size, light weight and low power consumption [51].

2.1.2 Non-cooperative Sensors

In addition to the capacity of detecting and tracking mid-air traffic by cooperative sensors, it is necessary for UAS to have an ability to sense other non-cooperative traffic in civil airspace for safe operations with other GA aircraft, which indeed is an essential requirement to obtain the regulator approval of integrating UAS into civil airspace. Currently available technologies include passive sensors like EO/IR cameras and acoustic sensors, or active sensors such as radar and lidar.

2.1.2.1 Passive Sensors: EO/IR Cameras and Acoustic Sensors

With the general need for eyes in the sky, EO/IR cameras are the most popular payloads carried on a UA during airborne missions in both military and civilian applications. Technically, EO cameras record images by capturing the reflected light from objects during the day and IR cameras provide night visions by detecting the object's heat during the night [42]. As discussed in the survey conducted in Karhoff et al. [52], in terms of small size, light weight and low power consumption, the vision-based DAA solution using EO/IR cameras is the most cost-effective DAA solution for small UAS to achieve an equivalent level of safety as human pilots on manned aircraft. Following this conclusion, tremendous efforts have been put into the research and development of implementing a vision-based DAA system for small UAS [53–58], where field programmable gate array (FPGA) and graphics processing unit (GPU) based hardware systems are employed for image processing in real-

time detection of other nearby mid-air traffic. Up to date, due to shortcomings of optical technologies, vision-based DAA systems have not achieved the full level of success as human pilots on manned aircraft with solid and robust traffic detections in visual meteorological conditions (VMC). For example, environmental or background disturbances on captured images, such as sun and clouds in the sky, or trees and moving targets on the ground, often increase the false alarm rate (FAR) for surrounding traffic [59]. Thus, generally, to reach an acceptable FAR, thresholds in detection algorithms have to be set to different values on a case-by-case basis. In addition, to achieve the same required field of view (FOV) as human pilots, i.e., $\pm 110^\circ$ in the front of the UA, multiple cameras have to be arrayed together on the UA so the increasing requirements of space, weight and real-time image processing capabilities will eventually limit this solution applied on small UAS [52, 58].

Acoustic sensors have been applied on small UAS to detect the bearing angle of approaching intruder by the sound of engines, propellers, or rotors on the aircraft [60, 61]. They consist of a number of microphones mounted on the aircraft to provide bearing information for sound at different frequencies. The microphone array measures phase differences to determine the bearing angle to the intruder aircraft in both azimuth and elevation [60]. At present, the detected bearing accuracy of acoustic sensors is low, so they cannot be used for accurate measurements; however, they can be used to cue other higher resolution sensors like EO/IR cameras to detect a nearby intruder aircraft [60].

2.1.2.2 Active Sensors: Radar and Lidar

In general, an active radar system consists of a transmitter, an antenna for emitting electromagnetic radiation and receiving the echo, a receiver and a processor. The distance to objects is determined by measuring the time taken for signal to travel

to the target and back, and the bearing of the target is determined by the angle of arrival of the echo [62]. As a proven technology, radar has been widely used to detect and track targets in many military and civilian applications, such as airborne radar, marine radar, traffic radar, and weather radar. PSR is a good example of using radar to monitor the air traffic in the surrounding area as a complementary system to SSR for ATC on the ground, regardless of whether or not those traffic aircraft have installed onboard cooperative sensors like transponders, TCAS, and ADS-B.

With the basic principle of radar, longer detection range and higher bearing resolution usually require higher power and a larger antenna. As a result, small airborne radar currently is not able to meet DAA requirements for small UAS unless improvements are made to radar with digital technologies for miniaturizing radar implementation [63,64]. Alternatively, a ground-based radar system like PSR for ATC is attractive for small UAS to ensure safe operations in civil airspace; however, because of aviation security, it is prohibited for commercial UAS operators to access local real-time air traffic data from ATC facilities by a communication link electronically [65]. Moreover, in many cases, small UAS are often operated in areas without ATC PSR coverage, so it will be worthwhile to deploy a portable ground-based radar system at the area nearby small UAS operations to provide DAA abilities for implementing the second near-term solution of integrating small UAS into civil airspace, as proposed in Chapter 1.

Similar to radar, lidar emits laser lights and receives returns to measure the distance to the target. With recent achievements on mechanical beam-steering components, lidar is a suitable sensor on small UAS for target detection with outstanding measurement accuracies on both range and bearing [66]; however, because its detection range is relatively short and the FOV is narrow, at present, lidar is mainly used for low-altitude obstacle avoidance and terrain mapping on small UAS [66,67], rather than for mid-air

traffic detection and tracking like airborne radar on large UAS and manned aircraft.

2.1.3 Summary of Sensor Performance

The sensing technologies discussed in this section have various advantages and drawbacks, which are briefly listed in Table 2.1. The cooperative sensors (transponders, TCAS, and ADS-B) can be used under all-weather conditions; in particular, ADS-B can meet the SWaP limitations on small UAS and their cost is low. The advantages of passive non-cooperative technologies (EO/IR or acoustic) are the low cost and the ability to detect mid-air non-cooperative traffic; however, they cannot provide range information for detected targets. In addition, the bearing resolution from the acoustic sensors is low, and EO/IR cameras do not work well in poor weather conditions. By contrast, an airborne radar has the ability to work well under all-weather conditions, but at present it cannot overcome the SWaP limitations on small UAS. Moreover, a lidar can be installed on small UAS, but it is used for short-range obstacle avoidance and low-altitude terrain mapping. Thus, at the current stage and in the near future, ground portable radar is the only option to help small UAS detect and track mid-air non-cooperative traffic nearby UAS operating areas.

Table 2.1: Summary of sensor performance

Sensors	Non cooperative	Passive sensing	All-weather	SWaP	Range	2D Bearing	Cost
Transponder	×	×	✓	×	✓	✓	✓
TCAS	×	×	✓	×	✓	✓	×
ADS-B	×	×	✓	✓	✓	✓	✓
EO	✓	✓	×	✓	×	✓	✓
IR	✓	✓	×	✓	×	✓	✓
Acoustic	✓	✓	✓	✓	×	✓	✓
Airborne Radar	✓	×	✓	×	✓	✓	×
Ground	✓	×	✓	×	✓	✓	×
Portable Radar	✓	×	✓	×	✓	✓	×
Lidar	✓	×	✓	×	✓	✓	×

Note: ✓: favourable/applicable; and ×: not favourable/applicable.

2.2 DAA Terminologies

To introduce the details, it is necessary to consider terminologies for the encounter environment, the DAA timeline, and the parameters that will be studied in the later chapters.

2.2.1 Encounter Environment

A key challenge of integrating UAS into civil airspace is the ability to detect and avoid other mid-air traffic in civil airspace as human pilots on manned aircraft [68]. As shown in Fig. 2.5, two layers of critical UAS safety boundaries are adopted by the RTCA SC-228 to quantitatively predict and resolve a potential conflict in a mid-air encounter, i.e., the Near Mid-Air Collision (NMAC) boundary and the Well Clear (WC) boundary [2]. The inner NMAC boundary is also called the Collision Volume (CV) in [19].

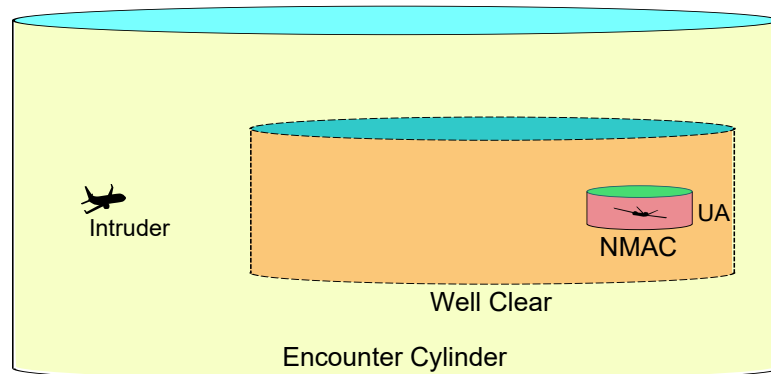


Figure 2.5: Encounter cylinder diagram.

As labelled in Fig. 2.6, the NMAC boundary is a standard cylinder: 500 ft in radius horizontally, and ± 100 ft in height vertically.

The WC boundary is not defined as simply as the NAMC boundary. The WC

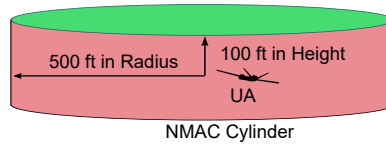


Figure 2.6: NMAC cylinder diagram.

boundary is not only a spatial separation in range, but also a temporal separation in time [69–71]. For example, during a head-on encounter in Fig. 2.7, the radius of the WC cylinder in the front of the UA is a 35-second travel distance between the intruder and the UA, and the radius of the WC cylinder in the back of the UA is 4000 ft. In addition, the height of the WC cylinder is ± 450 ft from the UA.

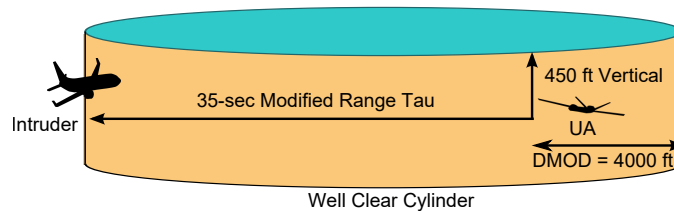


Figure 2.7: WC cylinder diagram.

2.2.2 DAA Timeline

Fig. 2.8 depicts a proposed timeline for DAA systems [8]. It shows that to avoid a potential collision, the sensors should detect mid-air traffic at a sufficient range so that there is enough time remaining for target tracking, decision making, and maneuver executing. The required detection range is not only determined by relative velocities between UA and traffic, but also by time delays from measurement uncertainties, tracker confirmations, PIC decisions, and aircraft aerodynamic responses [42]. As a result, these delays have to be counted into the warning alert time in the design of DAA systems.

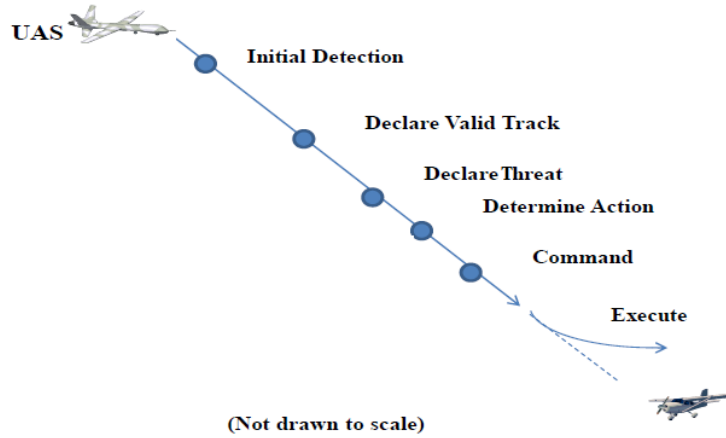


Figure 2.8: DAA timeline diagram [8].

2.2.3 DAA Parameters

For convenience in the analysis and implementation, air traffic positions in mid-air encounters are defined on the local three-dimensional Cartesian coordinates (x, y, h) with respect to the UA. As shown in Fig. 2.9, the x axis is pointing to the north for the latitude position, and the y axis is pointing to the east for the longitude position, and the h axis is pointing up for the altitude position. In addition, ψ is the traffic heading relative to the north, and v is the horizontal velocity of the traffic in the three-dimensional space.

In Fig. 2.9, $(\Delta x, \Delta y, \Delta h)$ are local positions for the traffic relative to the UA. Assume that

$$d_x = \Delta x = x_{\text{TRAFFIC}} - x_{\text{UA}} \quad (2.1)$$

$$d_y = \Delta y = y_{\text{TRAFFIC}} - y_{\text{UA}} \quad (2.2)$$

$$d_h = \Delta h = h_{\text{TRAFFIC}} - h_{\text{UA}} \quad (2.3)$$

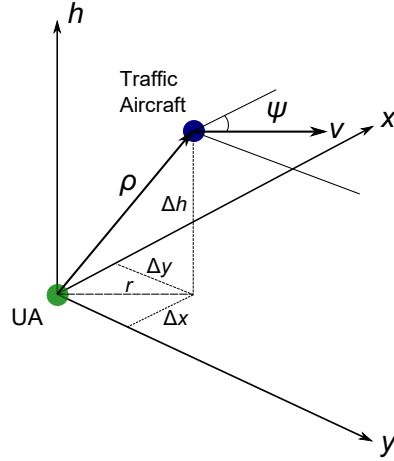


Figure 2.9: Aircraft positions in the three-dimensional space [9].

The slant range ρ is

$$\rho = \sqrt{d_x^2 + d_y^2 + d_h^2} \quad (2.4)$$

The slant range rate $\dot{\rho}$ is

$$\dot{\rho} = \frac{d\rho}{dt} = \frac{d_x v_{rx} + d_y v_{ry} + d_h v_{rh}}{\rho} \quad (2.5)$$

where v_{rx} , v_{ry} , and v_{rh} are traffic velocities relative to the UA in the three-dimensional space.

$$v_{rx} = v_{\text{TRAFFIC}} \cos(\psi_{\text{TRAFFIC}}) - v_{\text{UA}} \cos(\psi_{\text{UA}}) \quad (2.6)$$

$$v_{ry} = v_{\text{TRAFFIC}} \sin(\psi_{\text{TRAFFIC}}) - v_{\text{UA}} \sin(\psi_{\text{UA}}) \quad (2.7)$$

$$v_{rh} = \dot{h}_{\text{TRAFFIC}} - \dot{h}_{\text{UA}} \quad (2.8)$$

Similarly, the horizontal range r is

$$r = \sqrt{d_x^2 + d_y^2} \quad (2.9)$$

The horizontal range rate \dot{r} is

$$\dot{r} = \frac{dr}{dt} = \frac{d_x v_{rx} + d_y v_{ry}}{r} \quad (2.10)$$

It is noted that the safe horizontal range to separate UA from other traffic often changes in mid-air encounters, in terms of various relative velocities between UA and traffic. Thus, to unify a safe separation threshold in risk assessment, a time-based range tau is introduced to evaluate the risk severity of potential collisions as [72]

$$\tau = -\frac{r}{\dot{r}} \quad (\text{if } \dot{r} \neq 0) \quad (2.11)$$

Usually, a larger τ indicates lower collision risks and a smaller τ means higher collision risks. However, in the case of two tail-chase aircraft operated at similar velocities (i.e., range rate $\dot{r} \rightarrow 0$), the calculated range tau from Eq. 2.11 will stay high even when the intruder is in the NMAC cylinder (i.e., $r < 500$ ft). In addition, this range tau will not be able to provide sufficient alerting time to avoid a Loss of Well Clear (LoWC) or even a NMAC when a traffic suddenly accelerates. Thus, another modified range tau is used to provide a minimum range, Distance MODification (DMOD),¹ at which to alert regardless of the range tau. This modified range tau (τ_{mod}) is defined as [72, 73]

$$\tau_{mod} = -\frac{r - (DMOD^2/r)}{\dot{r}} = -\frac{r^2 - DMOD^2}{r\dot{r}} \quad (\text{if } r\dot{r} \neq 0) \quad (2.12)$$

where: DMOD = 4000 ft for the minimum of WC boundaries, and $(DMOD^2/r)$ is a range buffer depending on the ratio of the DMOD and the horizontal range, i.e.,

¹DMOD: an absolute distance threshold to alert the collision risk in mid-air encounters, e.g., DMOD = 4000 ft to alert the LoWC.

$$(\text{DMOD}^2/r) = \text{DMOD} \times \left(\frac{\text{DMOD}}{r}\right).$$

Another important encounter parameter is the Horizontal Miss Distance (HMD) between the UA and other traffic in an encounter, which refers to the horizontal distance at the horizontal Closest Point of Approach (CPA) between two aircraft throughout the entire encounter [2, 74]. In general, the horizontal range of two aircraft is defined as the following time domain function.

$$r(t) = \sqrt{(x_0 + v_{rx}t)^2 + (y_0 + v_{ry}t)^2} \quad (2.13)$$

where x_0 and y_0 are the initial positions of the other traffic relative to the UA.

The minimal distance occurs when $\frac{d(r(t)^2)}{dt} = 0$, so the time to CPA can be obtained by

$$t_{\text{CPA}} = \max\left(0, -\frac{x_0 v_{rx} + y_0 v_{ry}}{v_{rx}^2 + v_{ry}^2}\right) \quad (2.14)$$

where positive t_{CPA} for closing geometries and zero for others.

According to Eq. 2.13 and Eq. 2.14, the HMD of two aircraft in an encounter can be predicted from its current positions as [2]

$$\text{HMD} = \sqrt{(d_x + v_{rx}t_{\text{CPA}})^2 + (d_y + v_{ry}t_{\text{CPA}})^2} \quad (2.15)$$

Similarly, the Vertical Miss Distance (VMD) between the UA and other traffic at the horizontal CPA can be predicted by

$$\text{VMD} = d_h + v_{rh}t_{\text{CPA}} \quad (2.16)$$

2.3 Related Work

The MIT Lincoln Laboratory has developed a series of statistical aircraft encounter models to generate high fidelity aircraft encounters in US civil airspace (National Airspace System (NAS)) using Markov predictions on dynamic Bayesian networks, based on the ground radar data from more than 200 radar systems across the US [10,75,76]. One of these models, an uncorrelated encounter model, is designed for non-cooperative air traffic (without ATC guidance); another model, a correlated encounter model, is developed for cooperative air traffic (with ATC guidance). This thesis uses an uncorrelated encounter model to simulate the initial conditions and transitions of millions of non-cooperative aircraft in mid-air encounters on the fast-time simulation platform (as shown in the green box in Fig. 2.10). When required, a correlated encounter model is also used to simulate ATC-guided cooperative encounters.

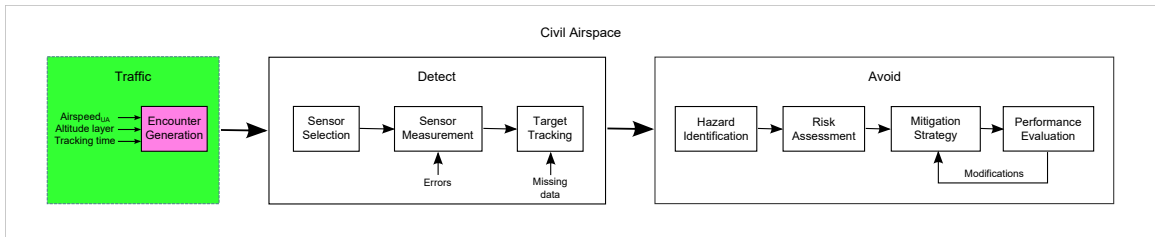


Figure 2.10: Block diagram for the fast-time simulation based analysis platform.

2.3.1 Bounded initial conditions and transitions for non-cooperative encounters in low altitude airspace

In general, most non-cooperative air traffic and small UAS are operated at similar altitude layers, usually, below 5000 ft. Their feature histograms, based on recorded radar data [10], are shown in Fig. 2.11,

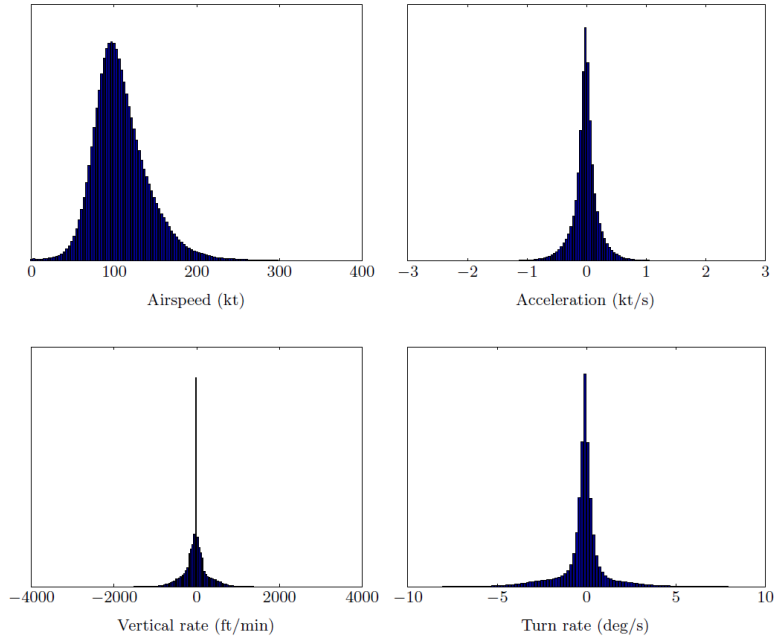


Figure 2.11: Feature histograms of recorded radar data based on 193 million samples [10].

where traffic horizontal airspeed $v \in [0, 300]$ kt, horizontal acceleration $\dot{v} \in [-1, 1]$ kt/sec, vertical rate $\dot{h} \in [-1250, 1250]$ ft/min, turn rate $\dot{\psi} \in [-6, 6]$ deg/sec, and traffic operating altitude $h \in [500, 5000]$ ft.

2.3.2 Size of encounter cylinder

In the uncorrelated encounter model, an encounter cylinder is chosen for starting positions to initiate mid-air traffic nearby the UA, which can be either a **fixed-size** cylinder (e.g. 5 nmi in radius, ± 1000 ft in height), or a **dynamic-size** one based on the relative velocity and the tracking time required for a mid-air encounter. For better simulation efficiency (in terms of the simulation time required for each encounter), a dynamic-size encounter cylinder is chosen to initiate mid-air encounters on the fast-time simulation platform, so that encounter trajectories can be simulated just enough for UA to detect and track nearby air traffic in a fixed period of time (i.e.,

a required DAA tracking time). As shown in Fig. 2.12, the dynamic-size encounter cylinder is not a regular cylinder and its size depends on the relative velocity, the tracking time required, and the traffic bearing relative to the UA at the encounter.

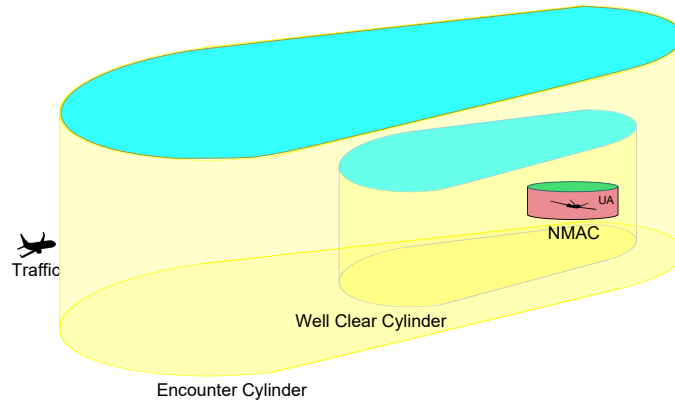


Figure 2.12: A dynamic-size encounter cylinder in the three-dimensional space.

Two types of dynamic-size encounter cylinders are established on the fast-time simulation platform for UAS DAA analysis in self-separation and collision avoidance: one dynamic-size encounter cylinder, with 120 seconds tracking time, is used for UAS self-separation; the other one, with 60 seconds tracking time, is used for UAS collision avoidance. In addition, similar to the DMOD defined in Subsection 2.2.3, a minimum distance boundary is also implemented on the dynamic-size encounter cylinder for tail-chase encounters with low relative velocities (e.g., $v_{\text{TRAFFIC}} - v_{\text{UAS}} = 85 \text{ kt} - 75 \text{ kt} = 10 \text{ kt} = 16.88 \text{ ft/sec}$). As a result, a self-separation encounter cylinder is set at a minimum of 2 nmi in radius and $\pm 800 \text{ ft}$ in height, and a collision avoidance encounter cylinder is set at a minimum of 1 nmi in radius and $\pm 450 \text{ ft}$ in height.

2.3.3 Aircraft model for encounter generation

UAS DAA performance analysis is performed based on aircraft trajectories rather than detailed aircraft aerodynamics, so a set of particle motion equations in Eq. 2.17 - Eq.

2.21 [77] are employed in the encounter generation module to update the aircraft's flight states and construct the encounter trajectories on the fast-time simulation platform. Following the definitions in Subsection 2.2.3, the aircraft's initial conditions are given as $\mathbf{Initial}_{AC} = [x, y, h, \psi, v, \dot{v}, \dot{h}, \dot{\psi}]$ in a three-dimensional space for latitude (north), longitude (east), altitude (up), heading, horizontal velocity, horizontal acceleration, vertical rate, and turn rate, respectively. Similarly, the aircraft transitions are given as $\mathbf{Transition}_{AC} = [t, \dot{v}, \dot{h}, \dot{\psi}]$ for encounter time elapsed, horizontal acceleration, vertical rate, turn rate, respectively. Thus, detailed equations for updating aircraft's flight states and constructing trajectories can be described as follows [77]:

$$h_{t+1} = h_t + \dot{h}_t \Delta t \quad (2.17)$$

$$x_{t+1} = x_t + v_t \cos(\psi_t) \Delta t + \frac{1}{2} \dot{v}_t \cos(\psi_t) \Delta t^2 \quad (2.18)$$

$$y_{t+1} = y_t + v_t \sin(\psi_t) \Delta t + \frac{1}{2} \dot{v}_t \sin(\psi_t) \Delta t^2 \quad (2.19)$$

$$v_{t+1} = v_t + \dot{v}_t \Delta t \quad (2.20)$$

$$\psi_{t+1} = \psi_t + \dot{\psi}_t \Delta t \quad (2.21)$$

where t is the non-negative integer, and Δt depends on the sampling rate, e.g., $\Delta t = 1$ sec at 1 Hz or $\Delta t = 0.1$ sec at 10 Hz. Fig. 2.13 shows a pair of sample encounter trajectories for a converging geometry of the UA with traffic from the front right (relative bearing at around 87 degrees), where encounter trajectories are updated at 1 Hz ($\Delta t = 1$ sec).

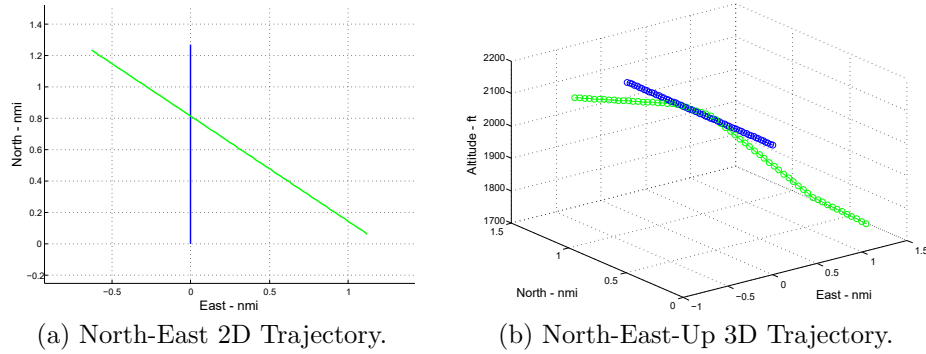


Figure 2.13: A pair of sample encounter trajectories generated by the uncorrelated encounter model (legend: blue for UA and green for traffic).

2.3.4 Implementation of encounter generation

In the implementation of encounter generation, a rejection sampling process [10, 76] is used to reject outbound traffic at the surface of an encounter cylinder and only construct inbound traffic trajectories for DAA analysis and evaluation on the fast-time simulation platform in Fig. 2.10. In addition, for a repeatable encounter analysis on the fast-time simulation platform, all the selected initial conditions and transitions of the UA and the inbound traffic are saved into Matlab workspace MAT-files. This enables both interaction explorations and DAA performance comparisons among various mitigation solutions, wind conditions, system delays on the fast-time simulation platform (by a workspace reloading process prior to the simulation on Matlab).

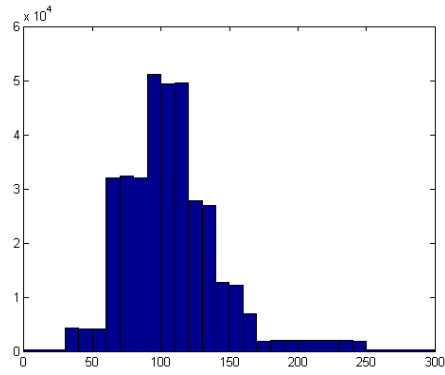
A sample of the encounter generation process is described as follows [10]:

1. Set a required tracking time for the encounter cylinder (e.g., 60 or 120 seconds); then use the MIT Lincoln Laboratory uncorrelated encounter model to generate five million sets of initial aircraft conditions $\mathbf{Initial}_{AC} = [x, y, h, \psi, v, \dot{v}, \dot{h}, \dot{\psi}]$ and aircraft transitions $\mathbf{Transition}_{AC} = [t, \dot{v}, \dot{h}, \dot{\psi}]$, and save them into matrices in the Matlab workspace MAT-files.

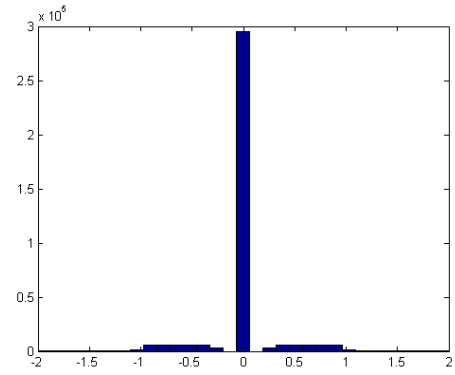
2. Determine a set of initial encounter generation parameters (e.g., the UA airspeed and the UA operating altitude layer), and then select a set of matched initial conditions for the UA from the saved five million sets of initial conditions and aircraft transitions in Matlab workspace MAT-files.
3. Select a random set of initial conditions for the traffic from the saved five million sets of initial conditions and aircraft transitions in Matlab workspace MAT-files.
4. Set the size of the dynamic encounter cylinder depending on initial conditions selected for two encounter aircraft.
5. Set the UA at the center of the encounter cylinder with a north heading (0°).
6. Set the traffic aircraft on a random position at a surface (i.e., top, bottom or side) of the encounter cylinder and select a heading randomly from $[0^\circ, 360^\circ]$ over a uniform distribution.
7. Perform a rejection sampling process to remove outbound traffic at the surface of encounter cylinder; then only construct trajectories for the UA and the inbound traffic; finally, save them into matrices in the Matlab workspace MAT-files as accepted encounter data for the future repeatable encounter analysis.
8. Repeat Step 2 through 7 to generate millions of mid-air encounters as needed.

For example, followed with the instructions listed above, a set of five million sample encounters are generated according to the predefined encounter parameters; e.g., the UA cruise airspeed $v = 76$ kt, the UA operating altitude layer $L = 2$ (a transition zone from 1200 ft to 3000 ft above ground level), and the required traffic tracking time $t = 60$ sec. The feature histograms of these five million sample encounters are

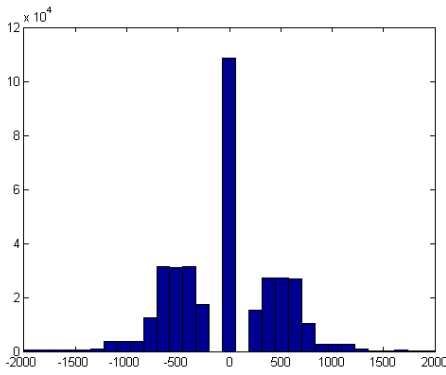
drawn in Fig. 2.14, and they are in accord with the ones based on recorded radar data in Fig. 2.11 in Subsection 2.3.1.



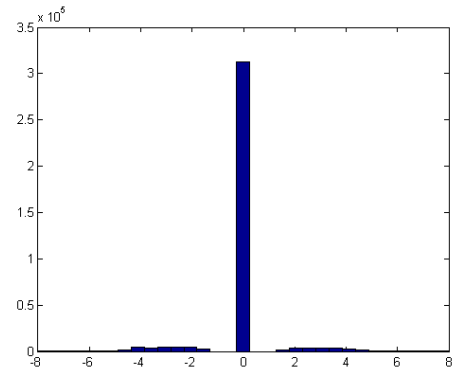
(a) Airspeed (kt)



(b) Acceleration (kt/sec)



(c) Vertical rate (ft/min)



(d) Turn rate (deg/sec)

Figure 2.14: Feature histograms of five million sample encounters simulated on the fast-time simulation platform.

2.4 Summary

In this chapter we examine detection sensor technologies for DAA systems that have been reported as currently available in the literature, and two sensor technologies are chosen for the research of DAA systems for small UAS: ADS-B and ground portable radar. Meanwhile, we also begin to introduce DAA terminologies on various aircraft encounter definitions and parameters, such as: NMAC, WC, CPA, slant range, horizontal range, range tau, modified range tau, time to CPA, HMD, and VMD. In the last section, we discuss the uncorrelated encounter model from the MIT Lincoln Laboratory and have it implemented into the encounter generation module on the fast-time simulation platform to provide high fidelity non-cooperative aircraft encounters in civil airspace for DAA analysis and evaluation.

In the following chapters, two major systems in Fig. 2.10, Detect System and Avoid System, will be developed in further detail followed by sensor measurement and target tracking in Chapter 3, hazard identification in Chapter 4, risk assessment in Chapter 5, as well as mitigation strategy and performance evaluation in Chapter 6.

Chapter 3

Detection and Tracking

As briefly discussed in Chapter 1, aviation authorities will not grant the integration of small UAS into non-segregated airspace with other manned aircraft, unless DAA systems for small UAS have reached an equivalent level of safety as human pilots on manned aircraft in civil airspace. As a result, further testing is required to prove that this equivalence of safety has been achieved on small UAS. First, to save time and cost, a large amount of data should be collected on a fast-time simulation based analysis platform to comprehensively explore the interactions among engaging elements of UAS operations in civil airspace with other manned aircraft, e.g., encounters at various initial conditions and aircraft transitions, encounters in different atmospheric conditions, failures on sensors, hidden limitations in algorithms, and delays across DAA systems. Later, flight tests on the HIL simulator and in the field should be used to validate the simulation results and ensure the performance of DAA systems. These two methods have been used together with great success for the development and verification of TCAS in the 1990s [42]. To follow this successful strategy, a fast-time simulation based analysis platform is thus designed and developed to facilitate the development of DAA systems for the future integration of small UAS into civil airspace.

3.1 Introduction

From this chapter we begin to introduce the design and development of the fast-time simulation platform, which consists of two major systems: the Detect System and the Avoid System, as drawn in Fig. 3.1. This chapter emphasizes the Detect System in the green box, including the sensor selection module, the sensor measurement module and the target tracking module. The Detect System is developed to simulate traffic detection and tracking functions for DAA systems on the fast-time simulation platform.

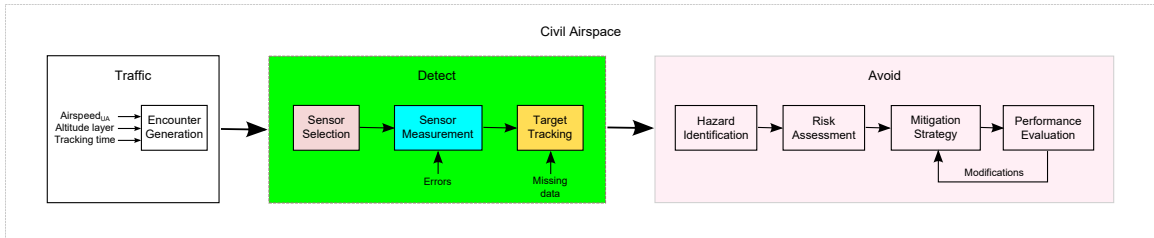


Figure 3.1: Block diagram for the fast-time simulation based analysis platform.

In this chapter, we first summarize the required inputs/outputs and internal functions for the modules in the Detect System and integrate them into the corresponding mathematical models to develop these modules (as shown in the green box in Fig. 3.1). Later, we introduce the implementation of these modules in further detail with the discussions for sensor errors and missing data during traffic detection and target tracking on the fast-time simulation platform.

3.2 Mathematical Models for Sensor Measurement

Two promising sensor technologies, ADS-B and ground portable radar, are selected in the research for small UAS to detect cooperative and non-cooperative mid-air traffic during UAS operations. For the integration of these two sensors on the fast-time simulation platform, we develop two sensor measurement models to convert the detected aircraft positions from their built-in measurement coordinates into the three-dimensional Cartesian coordinates (x, y, h) in accord with the coordinates used on the fast-time simulation platform, as discussed in Subsection 2.2.3.

3.2.1 Aircraft positions from ADS-B

In default, ADS-B equipped cooperative traffic aircraft broadcast their precise GPS positions and velocities during flight operations. These GPS positions are based on a WGS84 reference coordinate system in latitude, longitude, and altitude, in which latitude and longitude are in degrees, and altitude is in feet or meters. As discussed in Subsection 2.2.3, a local three-dimensional Cartesian coordinate system is used for DAA evaluation and analysis on the fast-time simulation platform. Thus, in the ADS-B measurement model, we need to convert the latitude and longitude from their global coordinates in degrees to the local Cartesian coordinates in nautical miles with respect to the UA, and convert the absolute altitude to the relative altitude in feet with respect to the UA. The conversion equations are given as follows [78–80]:

$$\varphi = \text{Latitude}_{\text{AVERAGE}} = 0.5 \times (\text{Latitude}_{\text{TRAFFIC}} + \text{Latitude}_{\text{UA}}) \quad (3.1)$$

$$Coef_{Lat} = 111132.92 - 559.82\cos(2\varphi) + 1.175\cos(4\varphi) + 0.0023\cos(6\varphi) \quad (3.2)$$

$$Coef_{Lon} = 111412.84\cos(\varphi) - 93.5\cos(3\varphi) + 0.118\cos(5\varphi) \quad (3.3)$$

$$\Delta x = Coef_{Lat}(\text{Latitude}_{\text{TRAFFIC}} - \text{Latitude}_{\text{UA}})/1852.0 \quad (3.4)$$

$$\Delta y = Coef_{Lon}(\text{Longitude}_{\text{TRAFFIC}} - \text{Longitude}_{\text{UA}})/1852.0 \quad (3.5)$$

$$\Delta h = (\text{Altitude}_{\text{TRAFFIC}} - \text{Altitude}_{\text{UA}}) \quad (3.6)$$

Note that Eq. 3.2 is used to calculate the latitude coefficient (the length in meters of a degree of latitude at a latitude on the the WGS84 spheroid). Similarly, Eq. 3.3 is used to calculate the longitude coefficient (the length in meters of a degree of longitude on the the WGS84 spheroid) [78–80]. Eq. 3.4 and Eq. 3.5 show that the global GPS coordinates are almost linear to the local three-dimensional Cartesian coordinates because the coefficients $Coef_{Lat}$ and $Coef_{Lon}$ do not change when the UA and traffic aircraft are in the nearby area during a mid-air encounter.

3.2.2 Aircraft positions from ground portable radar

A ground radar usually measures a mid-air moving target by slant range ρ , azimuth angle β , and elevation angle ε in the spherical polar coordinates as drawn in Fig. 3.2. Thus, in the ground radar measurement model, we need to convert these radar measurements from the spherical polar coordinates into the three-dimensional Cartesian coordinates (x, y, h) for further evaluation and analysis on the fast-time simulation platform. The conversions are listed as follows [81]:

$$x_{\text{TRAFFIC}} = \rho\cos(\varepsilon)\cos(\beta) \quad (3.7)$$

$$y_{\text{TRAFFIC}} = \rho\cos(\varepsilon)\sin(\beta) \quad (3.8)$$

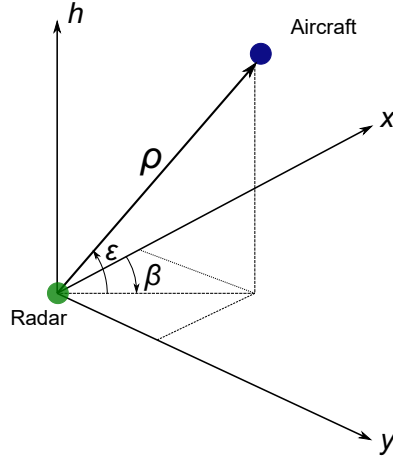


Figure 3.2: Radar polar and Cartesian coordinates diagram [11].

$$h_{\text{TRAFFIC}} = \rho \sin(\varepsilon) \quad (3.9)$$

where x_{TRAFFIC} , y_{TRAFFIC} , h_{TRAFFIC} are detected traffic positions relative to radar positions.

Finally, for the traffic relative positions $(\Delta x, \Delta y, \Delta h)$ with respect to the UA, we calculate them through Eq. 2.1, Eq. 2.2 and Eq. 2.3 with the current UA positions $(x_{\text{UA}}, y_{\text{UA}}, h_{\text{UA}})$ decoded from the UA telemetry data received by a GCS, or the ADS-B messages received by a ground ADS-B receiver.

In addition, Eq. 3.10, Eq. 3.11, and Eq. 3.12 are used to convert the three-dimensional Cartesian coordinates back to the spherical polar ones, and they will be used to calculate the radar measurement estimates in Eq. 3.24 in Section 3.3.

$$\rho = \sqrt{x^2 + y^2 + h^2} \quad (3.10)$$

$$\beta = \arctan\left(\frac{y}{x}\right) \quad (3.11)$$

$$\varepsilon = \arcsin\left(\frac{h}{\sqrt{x^2 + y^2 + h^2}}\right) \quad (3.12)$$

where x , y , h are current traffic positions relative to radar positions.

3.3 Mathematical Models for Target Tracking

Owing to the nature of noisy and/or possibly missing measurements on detection sensors during target tracking [82], Kalman filtering is adopted to provide more accurate position estimates of both the UA and the traffic during mid-air encounters [83]. In this section, two aircraft tracking models are developed to carry out traffic estimates for two sensor measurements: ADS-B and ground portable radar, respectively.

Similar to the trajectory generation equations in Subsection 2.3.3, the aircraft trajectory in a Kalman filter can be expressed in a discrete-time matrix notation as follows [84]:

$$\begin{bmatrix} x_{n+1} \\ y_{n+1} \\ h_{n+1} \\ v_{x,n+1} \\ v_{y,n+1} \\ v_{h,n+1} \end{bmatrix} = \begin{bmatrix} 1 & 0 & 0 & \Delta t & 0 & 0 \\ 0 & 1 & 0 & 0 & \Delta t & 0 \\ 0 & 0 & 1 & 0 & 0 & \Delta t \\ 0 & 0 & 0 & 1 & 0 & 0 \\ 0 & 0 & 0 & 0 & 1 & 0 \\ 0 & 0 & 0 & 0 & 0 & 1 \end{bmatrix} \begin{bmatrix} x_n \\ y_n \\ h_n \\ v_{x,n} \\ v_{y,n} \\ v_{h,n} \end{bmatrix} + \begin{bmatrix} \frac{\Delta t^2}{2} & 0 & 0 \\ 0 & \frac{\Delta t^2}{2} & 0 \\ 0 & 0 & \frac{\Delta t^2}{2} \\ \Delta t & 0 & 0 \\ 0 & \Delta t & 0 \\ 0 & 0 & \Delta t \end{bmatrix} \begin{bmatrix} \dot{v}_{x,n} \\ \dot{v}_{y,n} \\ \dot{v}_{h,n} \end{bmatrix} \quad (3.13)$$

where $X_n = [x_n, y_n, h_n, v_{x,n}, v_{y,n}, v_{h,n}]^T$ is the state vector of the detected target aircraft on the three-dimensional Cartesian coordinates at the time step n , Δt is the sensor measurement interval, (x_n, y_n, h_n) are the target positions, $(v_{x,n}, v_{y,n}, v_{h,n})$ are the target velocities, and $(\dot{v}_{x,n}, \dot{v}_{y,n}, \dot{v}_{h,n})$ are the target accelerations at the time step n .

During flight operations, aircraft usually operates at a constant velocity on a straight-line trajectory; thus aircraft maneuvers and accelerations are modelled as perturbations on the aircraft trajectory. By this assumption, we can rewrite Eq. 3.13

into a simplified matrix notation [84]:

$$X_{n+1} = F_n X_n + G_n V_n \quad (3.14)$$

where V_n is the Gaussian distributed random process noise $[\dot{v}_{x,n}, \dot{v}_{y,n}, \dot{v}_{h,n}]^T$ with zero mean and covariance matrix Q_n , F_n is the transition matrix, and G_n is the noise gain matrix. Similarly, we can simplify sensor measurements into a matrix notation [84]:

$$Z_n = H_n X_n + W_n \quad (3.15)$$

where Z_n is the sensor measurement output vector, H_n is the measurement coordinate transformation matrix that converts the state vector X_n from the Cartesian coordinates to the coordinates used on measurement sensors, and W_n is the sensor measurement error vector that is assumed to be zero-mean white Gaussian noise with covariance matrix R_n .

In Eq. 3.15, for non-linear transformation between aircraft trajectory estimates and position measurements, a first-order Taylor series approximation is used to linearize the transformation function and form the transformation matrix H_n . Then, the target aircraft positions can be estimated recursively by the following Prediction and Update processes in the extended Kalman filter (EKF) algorithm [83, 84].

Prediction

$$\hat{X}_{n|n-1} = F_{n-1} \hat{X}_{n-1|n-1} \quad (3.16)$$

$$P_{n|n-1} = F_{n-1} P_{n-1|n-1} F_{n-1}^T + G_{n-1} Q_{n-1} G_{n-1}^T \quad (3.17)$$

Update

$$\hat{X}_{n|n} = \hat{X}_{n|n-1} + K_n (Z_n - H_n \hat{X}_{n|n-1}) \quad (3.18)$$

$$P_{n|n} = P_{n|n-1} - K_n H_n P_{n|n-1} \quad (3.19)$$

where P_n is the estimation error covariance matrix, and K_n is the Kalman gain

$$K_n = P_{n|n-1} H_n^T [H_n P_{n|n-1} H_n^T + R_n]^{-1} \quad (3.20)$$

The process noise covariance matrix Q_n is

$$Q_n = \begin{bmatrix} \sigma_{\dot{v}_{rx}}^2 & 0 & 0 \\ 0 & \sigma_{\dot{v}_{ry}}^2 & 0 \\ 0 & 0 & \sigma_{\dot{v}_{rh}}^2 \end{bmatrix} \quad (3.21)$$

where $\sigma_{\dot{v}_{rx}}^2$, $\sigma_{\dot{v}_{ry}}^2$, $\sigma_{\dot{v}_{rh}}^2$ are acceleration covariances in the three-dimensional space.

For target tracking by the ADS-B, as the equations listed in Eq. 3.4, Eq. 3.5, and Eq. 3.6, the measurement coordinate transformation matrix H_n can be approximated linearly as

$$H_n = \begin{bmatrix} 1 & 0 & 0 & 0 & 0 & 0 \\ 0 & 1 & 0 & 0 & 0 & 0 \\ 0 & 0 & 1 & 0 & 0 & 0 \end{bmatrix} \quad (3.22)$$

The ADS-B measurement error covariance matrix R_n is

$$R_n = \begin{bmatrix} \sigma_x^2 & 0 & 0 \\ 0 & \sigma_y^2 & 0 \\ 0 & 0 & \sigma_h^2 \end{bmatrix} \quad (3.23)$$

where σ_x^2 , σ_y^2 , σ_h^2 are the ADS-B measurement error covariances for x , y , and h on the local three-dimensional coordinates.

On the other hand, for target tracking by the ground portable radar, the first-order Taylor series approximation is applied on the non-linear transformation equations (Eq. 3.10, Eq. 3.11, and Eq. 3.12) to obtain the coordinate transformation Jacobian matrix H_n as

$$H_n = \begin{bmatrix} \frac{x}{\sqrt{x^2 + y^2 + h^2}} & \frac{y}{\sqrt{x^2 + y^2 + h^2}} & \frac{h}{\sqrt{x^2 + y^2 + h^2}} & 0 & 0 & 0 \\ \frac{-y}{x^2 + y^2} & \frac{x}{x^2 + y^2} & 0 & 0 & 0 & 0 \\ -\frac{hx}{\sqrt{x^2 + y^2}(x^2 + y^2 + h^2)} & -\frac{hy}{\sqrt{x^2 + y^2}(x^2 + y^2 + h^2)} & \frac{\sqrt{x^2 + y^2}}{x^2 + y^2 + h^2} & 0 & 0 & 0 \end{bmatrix} \quad (3.24)$$

where (x, y, h) are predicted aircraft positions relative to radar positions at the time step $(n - 1)$.

The radar measurement error covariance matrix R_n is

$$R_n = \begin{bmatrix} \sigma_\rho^2 & 0 & 0 \\ 0 & \sigma_\beta^2 & 0 \\ 0 & 0 & \sigma_\varepsilon^2 \end{bmatrix} \quad (3.25)$$

where σ_ρ^2 , σ_β^2 , σ_ε^2 are the radar measurement error covariances on slant range, azimuth, and elevation.

3.4 Implementation for Sensor Measurement and Target Tracking

As shown in Fig. 3.3, sensor measurement errors and missing data are considered and simulated in the sensor measurement and target tracking modules on the fast-

time simulation platform because they are normal situations for UAS operations in civil airspace. Thus, based on the true trajectory data outputted from the encounter generation module, the EKF algorithm in this section is used “reversely” (in the design of the target tracking module) to introduce randomized sensor measurement errors, for generating representative trajectories fed to the Avoid System on the fast-time simulation platform.

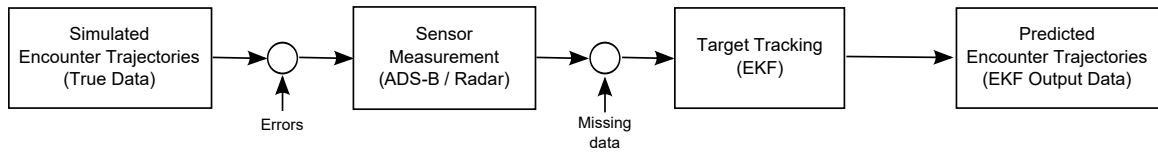


Figure 3.3: Implementation diagram for sensor measurement and target tracking modules.

For the implementation in this section, the difficulties are to determine sensor measurement errors as well as a number of matrices for EKF prediction and update processes, i.e., the estimation error covariance matrix P_n , the process noise covariance matrix Q_n , and the sensor measurement error covariance matrix R_n .

3.4.1 Sensor measurement errors

With regard to ADS-B and ground portable radar, measurement errors are composed by a large number of small and independent random factors such as the GPS position bias, the GPS position noise, the radar range error, the radar azimuth angle error, and the radar elevation angle error. Based on the central limit theorem, these measurement errors are in normal distribution [85–87]. Hence, in Fig. 3.4, aircraft positions of both the UA and traffic are drawn as a series of cylinders in the three-dimensional space, where their radii relate to the mean and standard deviation of horizontal measurement errors, and their heights are determined by the mean and standard deviation of altitude

measurement errors.

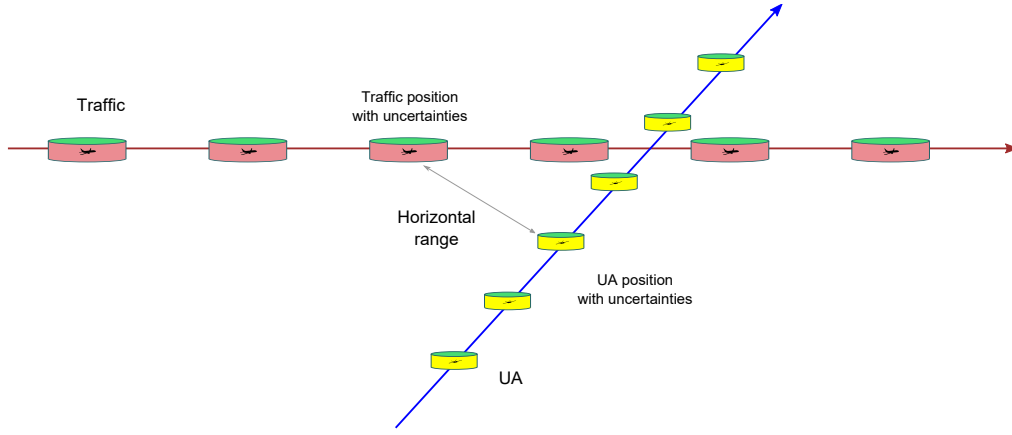


Figure 3.4: Aircraft measured positions with uncertainties during mid-air encounters.

ADS-B measurement errors

Usually, the ADS-B acquires horizontal positions from GPS and altitude through a barometric altimeter. For horizontal positions, ADS-B measurement errors come from GPS horizontal position errors, as well as from ADS-B uncompensated latency on receiving and transmitting GPS positions (e.g., 100 to 600 milliseconds) [2]. Thus, ADS-B horizontal position errors are simulated as the following equations [2, 88].

$$x_{measured} = x_{simulated} + (bias_{xy} + noise_{xy})\cos(\theta_{xy}) \quad (3.26)$$

$$y_{measured} = y_{simulated} + (bias_{xy} + noise_{xy})\sin(\theta_{xy}) \quad (3.27)$$

where: $bias_{xy} \sim \mathcal{N}(0, \sigma_{XY-EPU}^2)$ in normal distribution, $\theta_{xy} \in U(0, 2\pi)$ is the angle of the horizontal position bias on the horizontal x/y plane in uniform distribution, and

$$noise_{xy} = \begin{cases} -0.05\sigma_{XY-EPU} & \text{if } p \leq 0.5, \\ 0.05\sigma_{XY-EPU} & \text{Otherwise.} \end{cases} \quad (3.28)$$

Note that $p \in U(0, 1)$ is a uniform distributed random number and σ_{XY-EPU} is the standard deviation of the GPS Estimated Position Uncertainty (EPU)¹ on the horizontal x/y plane and $\sigma_{XY-EPU} \approx \frac{100}{3}$ m = 33.33 m = 0.018 nmi because nearly all (99.7%) of measurement readings in normal distribution are within **three** standard deviations from the mean [89].

For altitude measurements, as stated in the regulation [91], certified barometric altimeters provide vertical accuracy within ± 75 ft, so

$$h_{measured} = h_{simulated} + h_{err} \quad (3.29)$$

where: $h_{err} \sim \mathcal{N}(0, \sigma_{H-EPU}^2)$ in normal distribution, and σ_{H-EPU} is the standard deviation of the barometric altimeter EPU and $\sigma_{H-EPU} \approx \frac{75}{3} = 25$ ft.

Ground portable radar measurement errors

As discussed in Subsection 3.2.2, the ground radar usually measures mid-air moving targets by slant range ρ , azimuth angle β , and elevation angle ε in spherical polar coordinates; thus radar measurement errors comprise these three components: the range error, the azimuth angle error and the elevation angle error. In addition, these radar measurement errors often vary from radar systems and manufacturers. For simplicity in the implementation, we adopt a minimum requirement of radar track accuracy [1] in Table 3.1 to implement the radar measurement model for Detect System on the fast-time simulation platform.

¹ The GPS standard positioning service (SPS) provides 100 meters horizontal accuracy [90].

Table 3.1: Minimum requirement of radar track accuracy for high-priority traffic [1]

Measurement errors	Mean	Standard deviation	Unit
Range error	$\mu_{\rho-err} = 50$	$\sigma_{\rho-err} = 70$	ft
Azimuth angle error	$\mu_{\beta-err} = 0.5$	$\sigma_{\beta-err} = 1$	deg
Elevation angle error	$\mu_{\varepsilon-err} = 0.5$	$\sigma_{\varepsilon-err} = 1$	deg

where $\mu_{\rho-err}$, $\mu_{\beta-err}$, $\mu_{\varepsilon-err}$ are radar measurement error means on slant range, azimuth, and elevation, and $\sigma_{\rho-err}^2$, $\sigma_{\beta-err}^2$, $\sigma_{\varepsilon-err}^2$ are radar measurement error covariances on slant range, azimuth, and elevation.

Then,

$$\rho_{measured} = \rho_{simulated} + \rho_{err} \quad (3.30)$$

$$\beta_{measured} = \beta_{simulated} + \beta_{err} \quad (3.31)$$

$$\varepsilon_{measured} = \varepsilon_{simulated} + \varepsilon_{err} \quad (3.32)$$

where $\rho_{err} \sim \mathcal{N}(\mu_{\rho-err}, \sigma_{\rho-err}^2)$ in normal distribution, $\beta_{err} \sim \mathcal{N}(\mu_{\beta-err}, \sigma_{\beta-err}^2)$ in normal distribution, and $\varepsilon_{err} \sim \mathcal{N}(\mu_{\varepsilon-err}, \sigma_{\varepsilon-err}^2)$ in normal distribution as well.

3.4.2 Matrices initialization for EKF implementation

As in the EKF algorithm described in equations (Eq. 3.16 - Eq. 3.21), we need to initialize a number of matrices to enable recursive prediction and update processes, such as: the estimation error covariance matrix P_0 , the process noise covariance matrix Q_0 , the measurement coordinate transformation matrix H_0 , the sensor measurement error covariance matrix R_0 .

For the estimation error covariance matrix P_0 , we can use 10% estimation errors for traffic state variables $X_n = [x_n, y_n, h_n, v_{x,n}, v_{y,n}, v_{h,n}]^T$ at the beginning of EKF processes, thus

$$P_0 = \begin{bmatrix} 0.1 & 0 & 0 & 0 & 0 & 0 \\ 0 & 0.1 & 0 & 0 & 0 & 0 \\ 0 & 0 & 0.1 & 0 & 0 & 0 \\ 0 & 0 & 0 & 0.1 & 0 & 0 \\ 0 & 0 & 0 & 0 & 0.1 & 0 \\ 0 & 0 & 0 & 0 & 0 & 0.1 \end{bmatrix} \quad (3.33)$$

Later, the more accurate estimation error covariance matrix P_n is calculated and updated by Eq. 3.17 and Eq. 3.19 during EKF recursive prediction and update processes.

For most aircraft operated in civil airspace, the maximum load factor is less than four during the takeoff and turns [92], i.e., the maximum accelerations in lateral and vertical are less than $4g$ (39.2 m/s^2 with gravitational acceleration $g = 9.8\text{m/s}^2$). Thus, $\sigma_{\dot{v}_{rx}} = \sigma_{\dot{v}_{ry}} = \sigma_{\dot{v}_{rh}} = \frac{4g}{3} = \frac{39.2}{3}\text{m/s}^2 = 13.07\text{m/s}^2 = 0.007\text{nmi/s}^2 = 42.87\text{ft/s}^2$. With Eq. 3.21, the process noise covariance matrix Q_0 can be obtained in terms of traffic positions x , y in nmi and h in ft.

$$Q_0 = \begin{bmatrix} 0.00005 & 0 & 0 \\ 0 & 0.00005 & 0 \\ 0 & 0 & 1837.81 \end{bmatrix} \quad (3.34)$$

The measurement coordinate transformation matrix H_0 and the sensor measurement error covariance matrix R_0 depend on the measurement method selected, either the ADS-B by Eq. 3.22 and Eq. 3.23 with measurement error covariances ($\sigma_{\text{XY-EPU}}^2$, $\sigma_{\text{XY-EPU}}^2$, $\sigma_{\text{H-EPU}}^2$) calculated in Subsection 3.4.1, or the ground portable radar by Eq. 3.24 and Eq. 3.25 with measurement error covariances (σ_ρ^2 , σ_β^2 , σ_ε^2) obtained from Table 3.1 in Subsection 3.4.1.

3.4.3 Results for EKF target tracking with measurement errors

During EKF recursive prediction and update processes, predicted measurements can be used to replace missing measurements from sensors. Thus, missing measurement data in a short period of time (e.g., 1 to 5 seconds) will not be a major problem for target tracking with the EKF during UAS operations. In addition, for better performance in the EKF implementation, the sensor measurement interval Δt in Eq. 3.13 is set to 0.1 sec (10 Hz), so measurement interpolations are required for low update rate sensor measurements (e.g., ADS-B measurement at 1 Hz) in the EKF measurement update process in Eq. 3.18.

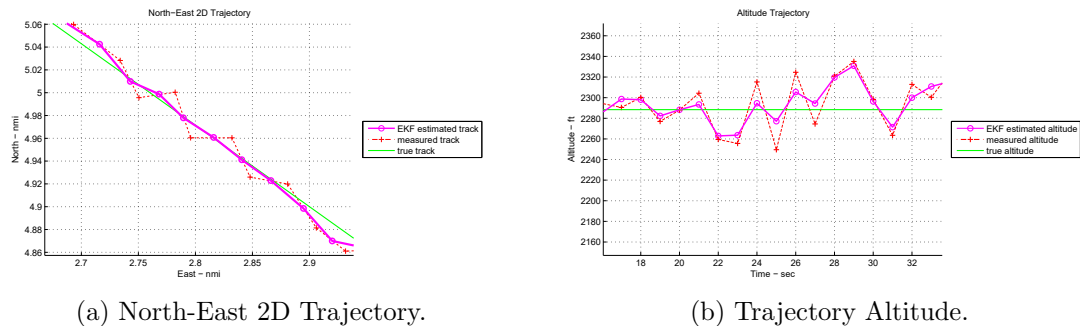
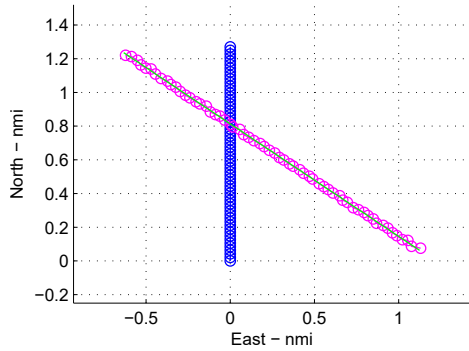
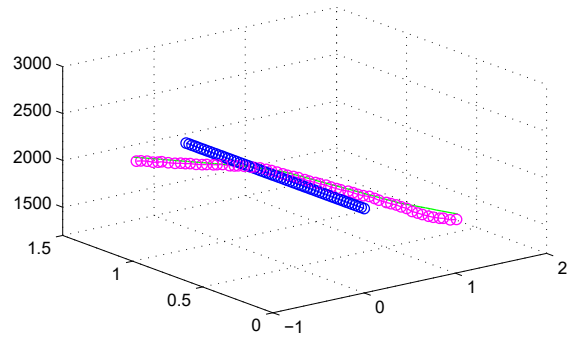


Figure 3.5: Comparisons for trajectories estimated by EKF on the horizontal and vertical planes.

As seen in Fig. 3.5, the EKF estimated traffic trajectories are much smoother than the ones directly from sensor measurements, and more closer to simulated traffic true trajectories. Furthermore, EKF estimated sample trajectories of the UA and traffic are drawn in Fig. 3.6 and Fig. 3.7 for measurements through the ADS-B or the ground portable radar, respectively.

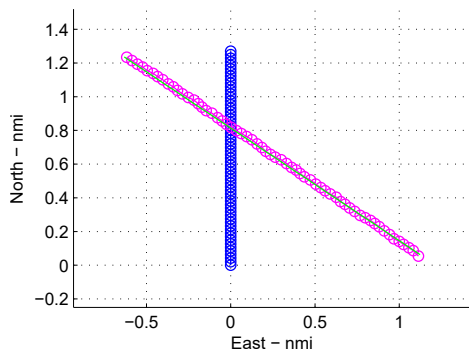


(a) North-East 2D Trajectory.

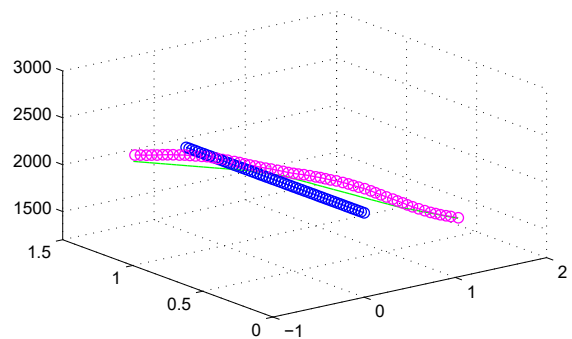


(b) North-East-Up 3D Trajectory.

Figure 3.6: A pair of sample encounter trajectories estimated by EKF through ADS-B measurement. (Legend: blue for simulated UA trajectory, green for simulated traffic true trajectory, and magenta for estimated traffic trajectory.)



(a) North-East 2D Trajectory.



(b) North-East-Up 3D Trajectory.

Figure 3.7: A pair of sample encounter trajectories estimated by EKF through ground portable radar measurement. (Legend: blue for simulated UA trajectory, green for simulated traffic true trajectory, and magenta for estimated traffic trajectory.)

3.5 Summary

In this chapter, we develop mathematical models for sensor measurement and target tracking modules on the fast-time simulation platform with regard to two promising sensor technologies: the ADS-B and the ground portable radar, which are selected for small UAS to detect cooperative and non-cooperative mid-air traffic during UAS operations in civil airspace. Later in this chapter, we discuss the implementation of sensor measurement and target tracking modules, where sensor measurement errors and a number of matrices initialized for EKF prediction and update processes are addressed.

By sensor measurement and target tracking modules, simulated UAS trajectories and EKF estimated traffic trajectories are obtained, and ready to feed to the Avoid System on the fast-time simulation platform for hazard identification, risk assessment and mitigation analysis. In Chapter 4, we determine the alerting boundaries necessary to identify mid-air encounter hazards. In Chapter 5, we develop a real-time computable collision risk level evaluation method for collision risk assessment. In Chapter 6, we construct a novel learning-based decision tree method to provide mitigation solutions for UAS mitigation strategy. The topics introduced in these three chapters are major contributions to this thesis.

Chapter 4

Hazard Identification

4.1 Introduction

In Chapter 3, we developed and discussed modules for the Detect System on the fast-time simulation platform to detect and track simulated nearby traffic during mid-air encounters. In this chapter and the next two chapters, we will develop modules for the Avoid System [93] on the fast-time simulation platform, as shown in the green box in Fig. 4.1. These modules are designed to identify traffic hazards and assess risk levels of potential collisions in mid-air encounters, as well as determine appropriate avoidance maneuvers when required [94].

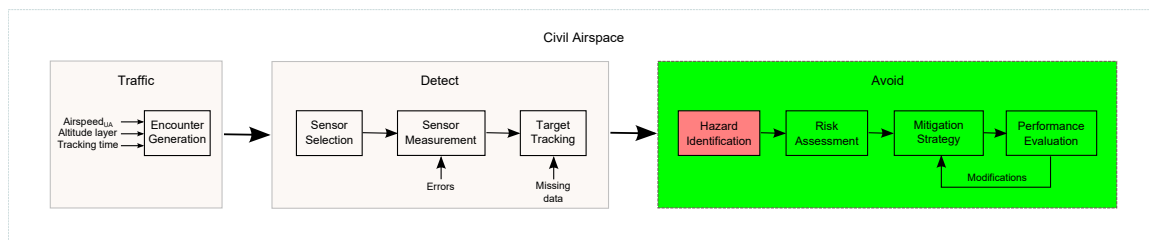


Figure 4.1: Block diagram for the fast-time simulation based analysis platform.

In this chapter, we focus on the development and implementation of the hazard identification module of the Avoid System on the fast-time simulation platform. We

first introduce mathematical definitions used for UAS to identify hazards with other approaching traffic during mid-air encounters. Later, in the implementation, because these mathematical definitions cannot be computed in real-time, we develop two algorithms to use Monte Carlo simulations to form lookup tables for UAS real-time hazard identification during mid-air encounters.

4.2 Mathematical Definitions for Mid-Air Encounters

A layered encounter environment in Fig. 4.2 is initially introduced in Subsection 2.2.1, where NMAC and WC cylinders are defined as two layers of critical UAS safety boundaries to help UAS predict and resolve a potential conflict in an encounter quantitatively.

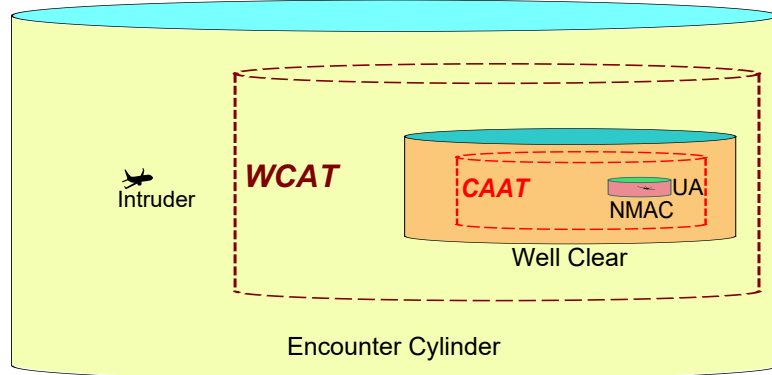


Figure 4.2: Layered encounter model of the airspace nearby the UA.

In this section, the formal definitions for NMAC and WC cylinders are given as follows:

Definition 1 (NMAC) *The NMAC boundary is a standard cylinder around the UA. $R_{\text{NMAC}} = 500$ feet in radius horizontally, and $h_{\text{NMAC}} = \pm 100$ feet in height vertically [2].*

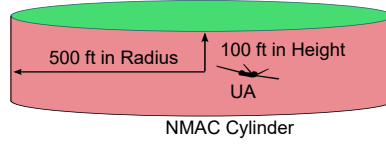


Figure 4.3: NMAC cylinder diagram.

Definition 2 (WC) For given: Modified Range Tau Threshold $\tau_{mod_{wc}}^* = 35 \text{ sec}$, Horizontal Miss Distance Threshold $HMD_{wc}^* = DMOD_{wc} = 4000 \text{ ft}$, and Vertical Separation Threshold $VMD_{wc}^* = 450 \text{ ft}$, an intruder is within WC [2] when

$$[0 \leq \tau_{mod} \leq \tau_{mod_{wc}}^*] \text{ and } [HMD \leq HMD_{wc}^*] \text{ and } [V_s \leq VMD_{wc}^*] \quad (4.1)$$

where: τ_{mod} is the modified range tau defined in Eq. 2.12, HMD is the horizontal miss distance at CPA defined in Eq. 2.15, and V_s is the vertical separation that can be calculated by $V_s = abs(d_h)$ with Eq. 2.3.



Figure 4.4: WC cylinder diagram.

By comparing to Fig. 2.5 in Subsection 2.2.1, we note that two dash line cylinders in Fig. 4.2 are added in this section, which are two new alerting threshold boundaries to avoid LoWCs or NMACs:

- A Well Clear Alerting Threshold (WCAT) boundary is located at the outer layer of the WC cylinder, which is the closest range boundary for the UA to still be able to remain WC with the traffic by a horizontal maneuver within the Flight Performance Envelope (FPE).

- A Collision Avoidance Alerting Threshold (CAAT) boundary is located at the outer layer of the NMAC cylinder, which is the closest range boundary for the UA to still be able to avoid NMACs with the traffic by a horizontal maneuver within the FPE.

Their formal mathematical definitions are given as follows:

Assume that $\mathbf{x} = [x, y, h, \psi, v]$ are aircraft states for latitude, longitude, altitude, heading, and horizontal velocity, respectively. $\mathbf{m} = [\dot{\psi}, t_m]$ are horizontal maneuvers for turn rate and time duration for maneuvering ¹. \mathbf{X}_{LPT} is the set of all possible aircraft states for linear projected traffic (LPT) ². \mathbf{X}_{LPU} is the set of all possible aircraft states for linear projected UA (LPU) ³. $\mathbf{M}_{\text{FPE}}^{\text{WC}}$ is the set of all allowed UA horizontal maneuvers within the FPE that can be used for remaining WC, and $\mathbf{M}_{\text{FPE}}^{\overline{\text{NMAC}}}$ is the same for UA to avoid NMACs.

Definition 3 (WCAT) For given: $\mathbf{x}_{\text{TRAFFIC}} \in \mathbf{X}_{\text{LPT}}$ and $\mathbf{x}_{\text{UA}} \in \mathbf{X}_{\text{LPU}}$, a traffic aircraft is outside of WCAT when

$$\exists \mathbf{m}_{\text{UA}} \in \mathbf{M}_{\text{FPE}}^{\text{WC}} \text{ such that WC} \quad (4.2)$$

Definition 4 (CAAT) For given: $\mathbf{x}_{\text{TRAFFIC}} \in \mathbf{X}_{\text{LPT}}$ and $\mathbf{x}_{\text{UA}} \in \mathbf{X}_{\text{LPU}}$, a traffic aircraft is outside of CAAT when

$$\exists \mathbf{m}_{\text{UA}} \in \mathbf{M}_{\text{FPE}}^{\overline{\text{NMAC}}} \text{ such that } \overline{\text{NMAC}} \quad (4.3)$$

¹ \mathbf{m} refers to single-move horizontal maneuvers, e.g., a horizontal maneuver at 6°/sec for 5 seconds.

² LPT refers to the traffic aircraft that are flying at constant velocities on straight line flights.

³ LPU refers to the UA that are flying at constant velocities on straight line flights.

4.3 Methodology for Hazard Identification

For hazard identification to prevent mid-air traffic from violating the safety boundaries, three control zones around the UA are proposed and defined in Fig. 4.5: the hazard zone, the alert zone, and the safe zone. In the design, **1)** when traffic aircraft break into the **hazard zone**, the UA should take immediate maneuvers to avoid potential mid-air collisions; **2)** when traffic aircraft break into the **alert zone** the UA may or may not respond to alerts from DAA systems upon collision risk levels; and **3)** when traffic aircraft are outside of the alert zone, the UA are in the **safe zone** and can remain on the original flight course.

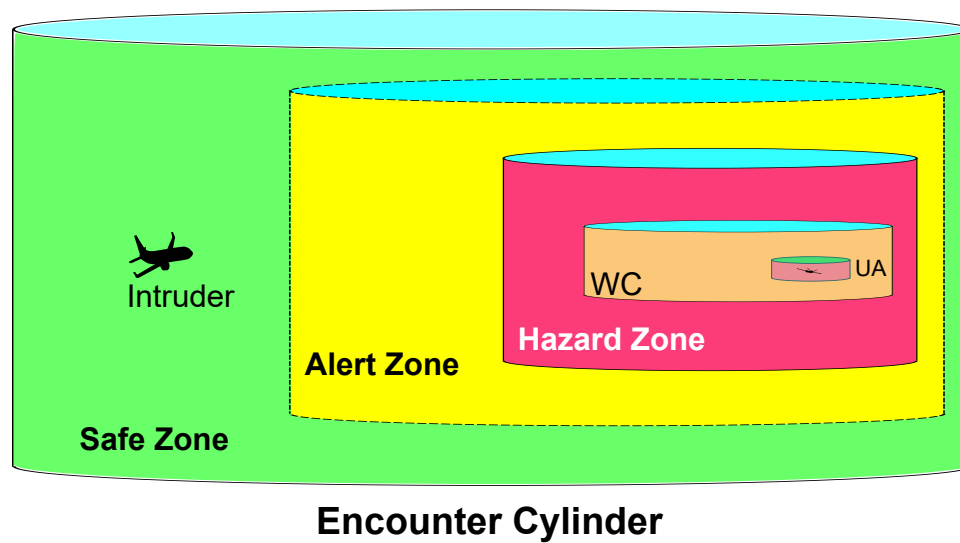


Figure 4.5: Layered encounter zones of the UA.

As depicted in Fig. 4.5, the safe zone in green refers to the areas outside the alert zone of the UA. The alert zone in yellow is a larger cylinder outside the hazard zone, which is defined as follows [2]:

Definition 5 (Alert Zone) For given: Modified Range Tau Threshold $\tau_{mod_{AZ}}^* = 110$ sec, Horizontal Miss Distance Threshold $HMD_{AZ}^* = DMOD_{AZ} = 2$ nmi, and Vertical

Separation Threshold $VMD_{AZ}^ = 800$ ft, an intruder is within the alert zone when*

$$[0 \leq \tau_{mod} \leq \tau_{mod_{AZ}}^*] \quad \text{and} \quad [HMD \leq HMD_{AZ}^*] \quad \text{and} \quad [V_s \leq VMD_{AZ}^*] \quad (4.4)$$

The hazard zone refers to a region outside the WC boundary and within the alert zone of the UA, which is determined by the WCAT boundary (i.e., the threshold boundary for the UA to initiate maneuvers to avoid LoWCs).

As mentioned in Chapter 1, two types of UAS mitigation solutions are developed for DAA systems to avoid LoWCs or NMACs during mid-air encounters: self-separation and collision avoidance, which can be clearly described using above five definitions given in this chapter.

- **Self-separation** refers to efforts carried out by the PIC with the guidance from DAA systems to avoid LoWCs (the breach of the hazard zone) when traffic aircraft are penetrating the alert zone of the UA with LoWCs projected.
- **Collision avoidance** refers to maneuvers triggered by DAA systems to avoid NMACs when traffic aircraft have entered the hazard zone and are close to breaching the CAAT boundary of the UA with NMACs projected.

4.4 Implementation for Hazard Identification

To identify hazards for the UA during mid-air encounters, we should first locate boundaries for the alert zone and the hazard zone of the UA. As given in Definition 5 (Alert Zone) and Definition 3 (WCAT), the alert zone of the UA can be easily calculated in real-time through Eq. 4.4; however, the hazard zone (i.e., the WCAT boundary) of the UA cannot be simply obtained through the statement in Definition

3 (WCAT) in real-time, because it usually requires a time-consuming Monte Carlo (MC) simulation to estimate the WCAT boundary for the UA in that encounter.

Moreover, in the case of the breach of the hazard zone, we should locate the CAAT boundary for DAA systems to determine if collision avoidance maneuvers are required as a last resort for the UA to avoid potential NMACs. Similar to the WCAT, the CAAT boundary cannot be calculated through the statement in Definition 4 (CAAT) in real-time, which also requires a time-consuming MC simulation to carry out the estimation.

As a result, we develop two algorithms in this section based on MC simulations to locate WCAT and CAAT boundaries, and then establish WCAT and CAAT lookup tables for real-time hazard identification on the fast-time simulation platform. It is noted that small UA are usually light-weight (e.g., less than 25 kg) and operate at a slow cruise airspeed (e.g., 75 kt), so their turning trajectories and the time needed to complete turns vary in different wind conditions (i.e., different wind speed and wind directions). As small UA turning trajectories look very different under various wind conditions in Fig. 4.6, wind effects have to be quantified in MC simulations to locate WCAT and CAAT boundaries for small UA.

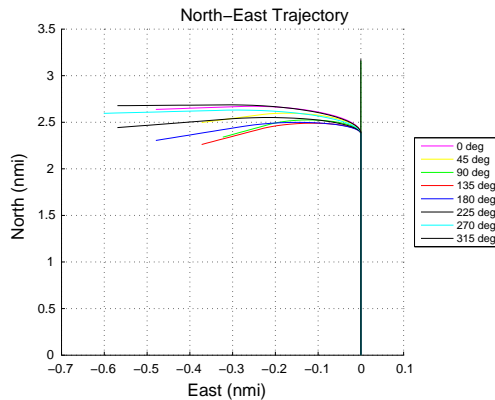


Figure 4.6: Sample turning trajectories for 75 kt UA under 20 kt winds in various wind directions from 0° to 360° every 45° by 20-second $2g$ left level turns ($6^\circ/\text{sec}$).

4.4.1 Aircraft trajectory generation in the wind

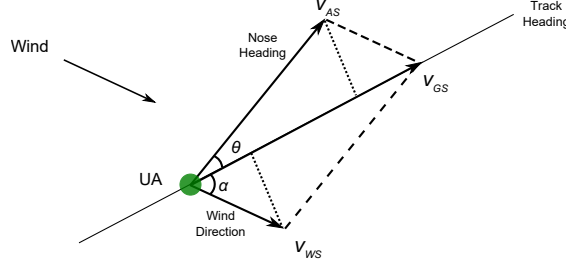


Figure 4.7: Aircraft trajectory generation in the wind.

During mid-air encounters, DAA maneuvers are usually triggered in long-range, thus as suggested in [95–97], small UA trajectory during level flights and horizontal maneuvers in the wind can be propagated based on a kinematics model discussed in [98]. For general cases in UAS operations, we can assume that the wind has only a horizontal component with wind speed v_{WS} and wind direction ψ_{WIND} , and the UA is on the level with airspeed v_{AS} , ground speed v_{GS} , and turn rate $\dot{\psi}$, thus UA trajectories during level flights and horizontal maneuvers in the wind can be generated by the following equations, as depicted in Fig. 4.7.

$$\alpha(0) = \psi_{WIND} - \psi_{TRACK}(0) \quad (4.5)$$

$$\theta(0) = \arcsin\left(\frac{v_{WS} \sin(\alpha(0))}{v_{AS}}\right) \quad (4.6)$$

$$\psi_{NOSE}(0) = \psi_{TRACK}(0) - \theta(0) \quad (4.7)$$

$$\psi_{NOSE}(n) = \psi_{NOSE}(n-1) + \dot{\psi}(n) \quad (4.8)$$

$$v_{GS_x}(n) = v_{AS} \cos(\psi_{NOSE}(n)) + v_{WS} \cos(\psi_{WIND}) \quad (4.9)$$

$$v_{GS_y}(n) = v_{AS} \sin(\psi_{NOSE}(n)) + v_{WS} \sin(\psi_{WIND}) \quad (4.10)$$

$$x_n = x_{n-1} + v_{gsx}(n) \quad (4.11)$$

$$y_n = y_{n-1} + v_{gsy}(n) \quad (4.12)$$

$$h_n = h_{n-1} \quad (4.13)$$

where: $n \in \mathbb{N}^+$. θ is the angle between the UA nose heading ψ_{NOSE} and the UA ground track heading ψ_{TRACK} . α is the angle between the wind direction ψ_{WIND} and the UA ground track heading ψ_{TRACK} .

4.4.2 Algorithms to determine WCAT and CAAT boundaries

For simplicity, vertical boundaries of CAAT and WCAT are pre-defined at fixed heights; namely, the vertical boundary of CAAT is defined as $VMD_{\text{WC}}^* = 450$ ft, and the vertical boundary of WCAT is defined as $VMD_{\text{AZ}}^* = 800$ ft. Thus, only horizontal boundaries of WCAT and CAAT are required to be determined via MC simulations by a series of co-altitude mid-air encounters.

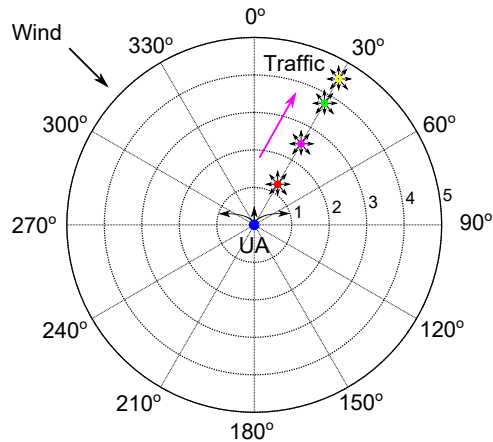


Figure 4.8: A web structure for Monte Carlo simulations to determine WCAT and CAAT boundaries (bearing in deg and range in nmi).

To implement these MC simulations, as shown in Fig. 4.8, we introduce a web structure in the algorithm design based on the principle of dynamic programming [99,100], where traffic aircraft are initiated from inner circles to outer circles at bearing angles $[0^\circ, 360^\circ)$ with heading angles in $[0^\circ, 360^\circ)$; UA are initiated at the web center with the 0° heading angle (to the north). At each bearing angle, we locate the shortest horizontal range between UA and traffic at which UA can avoid LoWCs or NMACs with traffic in all possible headings by one of the appropriate horizontal maneuvers.

Algorithm 1 Determine WCAT

```

1: function DETERMINEWCAT( $v_{UA}, \psi_{UA}$ )
2:   for  $\psi_{TRAFFIC} \in [0^\circ, 360^\circ)$  with  $1^\circ$  increment > do
3:     for  $v_{TRAFFIC} \in [50, 300]$  kt with 50 kt increment > do
4:       for  $\psi_{WIND} \in [0^\circ, 360^\circ)$  with  $45^\circ$  increment > do
5:         for  $\beta_{TRAFFIC} \in [0^\circ, 360^\circ)$  with  $1^\circ$  increment > do
6:           for  $r_{TRAFFIC} \in [0.6, 10]$  with 0.01 nmi increment > do
7:             while LoWC or LoWC-projected (according to Eq. 4.1) do
8:               for  $\psi_{UA} \in [-180^\circ, 180^\circ]$  with  $\psi_{UA}$  increment > do
9:                 Generate trajectories for traffic in the wind
10:                Generate maneuvering trajectories for UA in the wind
11:                by a single-move maneuver to the new heading
12:                if the UA regains WC then 4
13:                  Update and record the shortest traffic range  $r_{TRAFFIC}$ 
14:                  Update and record the least maneuvering method
15:                  either left turn or right turn initiated on UA
16:                  with the heading change in For Loop ( $\psi_{UA}$ )
17:                end if
18:              end for
19:            end while
20:          end for
21:        end for
22:      end for
23:    end for
24:  end for
25: end function

```

In the implementation, two algorithms are developed for UA to determine WCAT

⁴Based on a Detect and Avoid Alerting Logic for Unmanned Systems (DAIDALUS) in [101]

and CAAT boundaries via MC simulations, i.e., Algorithm 1 (Determine WCAT) and Algorithm 2 (Determine CAAT). For obtaining bounded WCAT and CAAT boundaries, as Definition 3 (WCAT) and Definition 4 (CAAT), two algorithms are designed with two assumptions: **1)** traffic are on level flights with constant horizontal velocities throughout mid-air encounters; and **2)** UA are on level flights or level maneuvers to avoid LoWCs or NMACs. Hence, the states of UA and traffic can be reduced to $[x, y, \psi, v, \dot{\psi}]$ for latitude, longitude, heading, horizontal velocity, and turn rate, respectively.

The parameters and settings used in MC simulations to implement Algorithm 1 (Determine WCAT) and Algorithm 2 (Determine CAAT) are listed as follows:

- Based on the airspace in the low altitude below 5000 ft at which small UA are most likely operated and the feature histograms in Fig. 2.11, assume that small UA are operated at airspeed $v_{UA} = 75$ kt and turn rate $\dot{\psi}_{UA} = 6$ °/sec.
- Traffic are simulated at an airspeed range of [50, 300] kt with an airspeed increment every 50 kt.
- For WCAT, traffic are initiated at 0.6 nmi (within $DMOD_{wc} = 0.66$ nmi = 4000 ft) at a bearing angle $\beta_{TRAFFIC}$ in $[0^\circ, 360^\circ)$ (e.g. at 30° in Fig. 4.8) and move outer bound every 0.01 nmi for each simulation run.
- For CAAT, traffic are initiated at 490 ft (0.08 nmi within $R_{NMAC} = 500$ ft) at a bearing angle $\beta_{TRAFFIC}$ in $[0^\circ, 360^\circ)$ and move outer bound every 10 ft (0.0016 nmi) for each simulation run.
- The detected traffic bearing $\beta_{TRAFFIC}$ and the traffic heading $\psi_{TRAFFIC}$ are selected every 1° in $[0^\circ, 360^\circ)$.
- Winds are introduced at 20 kt in eight directions every 45° in $[0^\circ, 360^\circ)$.

In addition, during MC simulations, for each simulated encounter, the closest traffic range and the least maneuvering method (left turn or right turn with the least heading change on the UA), as well as other related encounter parameters such as v_{UA} , ψ_{UA} , $v_{TRAFFIC}$, $\psi_{TRAFFIC}$, $\beta_{TRAFFIC}$, v_{WIND} , ψ_{WIND} , HMD , VMD , and τ_{mod} , are saved in a SQLite local database [102] for further analysis. In this chapter, they are first used to construct WCAT and CAAT lookup tables for real-time hazard identification on the fast-time simulation platform. Later in Chapter 6, these encounter results will be used again as the encounter maneuvering guidance knowledge base to guide decision making in the mitigation strategy module.

Algorithm 2 Determine CAAT

```

1: function DETERMINECAAT( $v_{UA}$ ,  $\psi_{UA}$ )
2:   for  $\langle \psi_{TRAFFIC} \in [0^\circ, 360^\circ)$  with  $1^\circ$  increment  $\rangle$  do
3:     for  $\langle v_{TRAFFIC} \in [50, 300]$  kt with 50 kt increment  $\rangle$  do
4:       for  $\langle \psi_{WIND} \in [0^\circ, 360^\circ)$  with  $45^\circ$  increment  $\rangle$  do
5:         for  $\langle \beta_{TRAFFIC} \in [0^\circ, 360^\circ)$  with  $1^\circ$  increment  $\rangle$  do
6:           for  $\langle r_{TRAFFIC} \in [490, 10000]$  with 10 ft increment  $\rangle$  do
7:             while NMAC or NMAC-projected (upon Definition 1) do
8:               for  $\langle \psi_{UA} \in [-180^\circ, 180^\circ]$  with  $\psi_{UA}$  increment  $\rangle$  do
9:                 Generate trajectories for traffic in the wind
10:                Generate maneuvering trajectories for UA in the wind
11:                by a single-move maneuver to the new heading
12:                if the UA avoids NMAC then
13:                  Update and record the shortest traffic range  $r_{TRAFFIC}$ 
14:                  Update and record the least maneuvering method
15:                  either left turn or right turn initiated on UA
16:                  with the heading change in For Loop ( $\psi_{UA}$ )
17:                end if
18:              end for
19:            end while
20:          end for
21:        end for
22:      end for
23:    end for
24:  end for
25: end function

```

4.4.3 Impact of WCAT and CAAT boundaries on wind uncertainties

To analyze the impact of WCAT and CAAT boundaries on wind uncertainties (i.e., various wind speeds and wind directions), a 20 kt gusty wind with a pattern [12] in Fig. 4.9 is introduced in MC simulations while locating WCAT and CAAT boundaries.

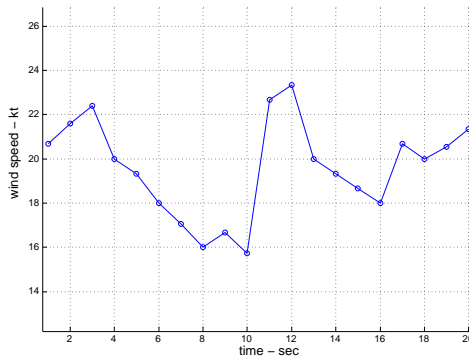


Figure 4.9: An example of 20-second gusty wind pattern with wind velocity jumps [12].

Followed by Algorithm 1 (Determine WCAT) and Algorithm 2 (Determine CAAT) with the gusty winds introduced in eight wind directions from 0° to 360° every 45° , two MC simulations are performed in this section and encounter results are saved in the database as designated in Subsection 4.4.2. Once these two MC simulations are completed, a data retrieving process is then performed to find the shortest horizontal range for UA to avoid LoWCs or NMACs at each bearing angle in $[0^\circ, 360^\circ)$ under one of the gusty wind conditions for nearby traffic operating in the heading angles from 0° to 360° every 1° and the airspeeds from 50 kt to 300 kt every 50 kt.

For example, at the bearing angle 30° for a 100 kt operated traffic aircraft under a 20 kt gusty wind in 45° (southwest wind), 360 matched records are retrieved from the database for traffic in all heading angles from 0° to 360° every 1° , and then the alert threshold for this bearing angle 30° is obtained by the shortest range among these

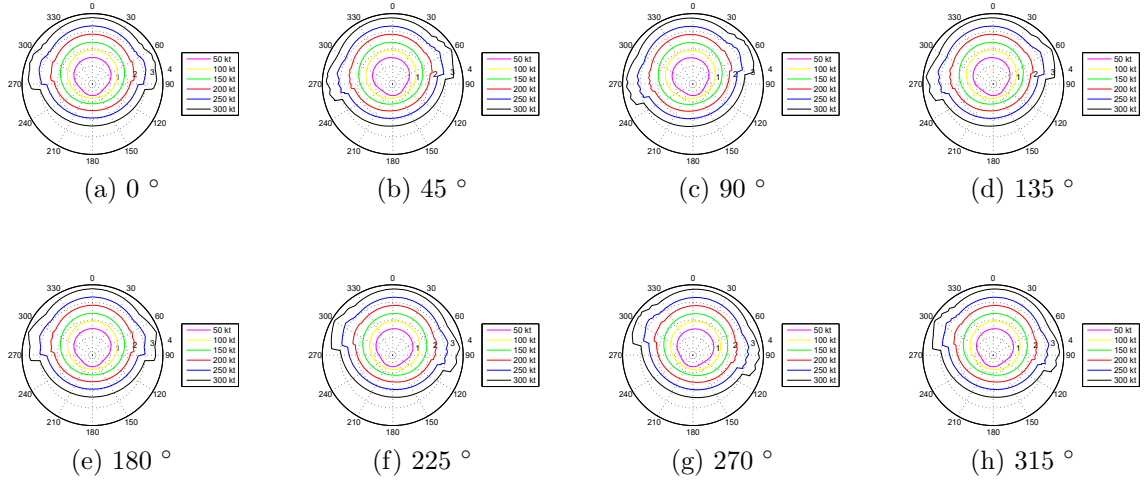


Figure 4.10: Range-based WCAT diagrams with 20 kt gusty winds in eight directions (bearing in deg, range in nmi, UA at 75 kt vs. traffic at various airspeeds).

360 retrieved records. Similar to this example, data retrieving processes for all 360 bearing angles, six traffic airspeeds, and eight gusty wind directions are performed throughout the whole database and finally a number of WCAT and CAAT boundaries are obtained and plotted in this section.

WCAT

In Fig. 4.10, eight subfigures show small UA WCAT boundaries under 20 kt gusty winds in eight wind directions, where WCAT boundaries are rotated in various wind directions. For instance, WCAT boundaries are left rotated when the winds come from the left side of the UA (e.g., southwest wind in 45° and northwest wind in 135°), and vice versa. Moreover, in each subfigure in Fig. 4.10, the size of WCAT boundaries are proportional to traffic velocities; namely, the faster the traffic velocities the bigger the WCAT boundaries. In addition, the UA front $\pm 120^\circ$ WCAT boundaries are generally larger than the UA rear ones due to faster relative velocities between UA and traffic.

During UAS operations, wind conditions around the UA usually vary over time

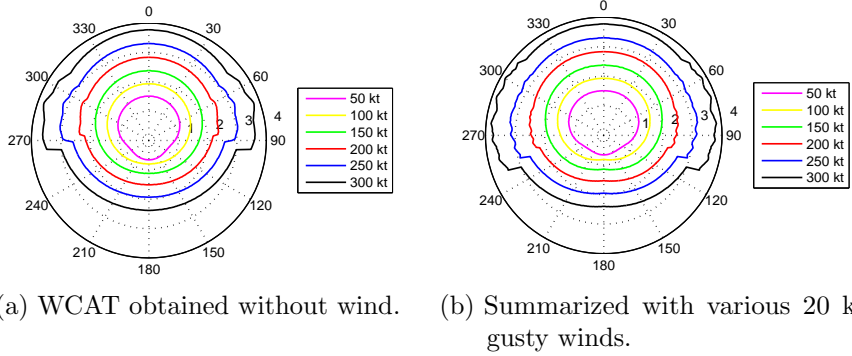


Figure 4.11: Summarized range-based WCAT diagrams (bearing in deg, range in nmi, UA at 75 kt vs. traffic at various airspeeds).

and location, and no accurate wind velocity measurements are available for DAA systems (only estimates based on the airspeed and groundspeed of the UA). Thus, to overcome wind uncertainties on WCAT boundaries, we reorganize eight sets of WCAT boundaries in Fig. 4.10 into a set of wind-summarized WCAT boundaries in Fig. 4.11b to cover encounters in various wind conditions. In general, the UA front WCAT boundaries in Fig. 4.11b are enlarged in comparison with the ones without wind in Fig. 4.11a. In particular, the UA WCAT boundaries at the bearing angles $[95^\circ, 110^\circ]$ and $[250^\circ, 265^\circ]$ are enlarged dramatically due to the WCAT boundary rotations in various wind directions. For quantitative comparison between Fig. 4.11a and Fig. 4.11b, we define a new variable, the threshold changing ratio (TCR).

$$TCR_{WCAT} = \frac{WCAT_{WIND-SUMMARIZED}}{WCAT_{NO-WIND}} \times 100\% \quad (4.14)$$

Two TCR diagrams of WCAT boundaries on Cartesian coordinates and on polar coordinates are plotted in Fig. 4.12. The TCRs of WCAT boundaries are increased by almost 25% between the wind-summarized WCAT and the no-wind WCAT at the bearing angles $[95^\circ, 110^\circ]$ and $[250^\circ, 265^\circ]$. In other words, these two traffic bearing regions are the most vulnerable regions for the PIC to identify hazards and initiate

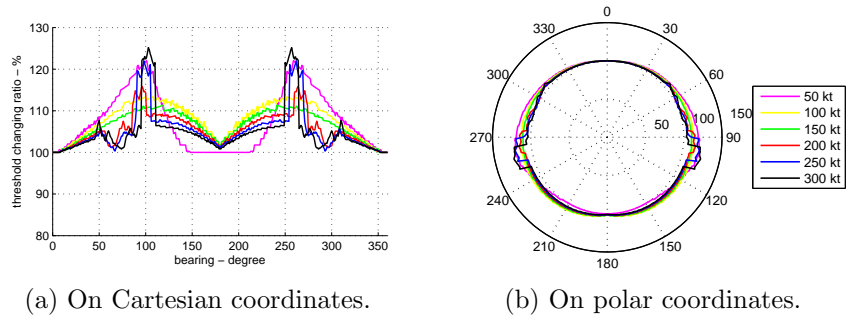


Figure 4.12: Threshold changing ratio diagrams for the impact of WCAT boundaries on wind uncertainties (UA at 75 kt vs. traffic at various airspeeds).

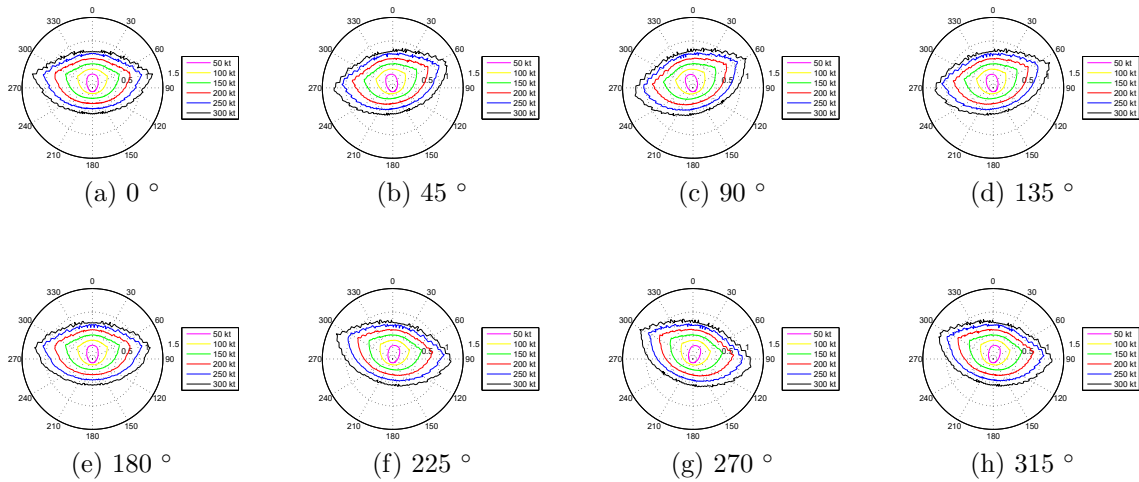


Figure 4.13: Range-based CAAT diagrams with 20 kt gusty winds in eight directions (bearing in deg, range in nmi, UA at 75 kt vs. traffic at various airspeeds).

maneuvers to avoid LoWCs in various wind conditions during UAS operations.

CAAT

Eight subfigures in Fig. 4.13 show small UA CAAT boundaries under 20 kt gusty wind in eight wind directions, where CAAT boundaries are rotated into wind directions as those rotations occurred on WCAT boundaries. Moreover, in each subfigure in Fig. 4.13, the size of CAAT boundaries are proportional to traffic velocities; namely, the faster the traffic velocities the bigger the CAAT boundaries.

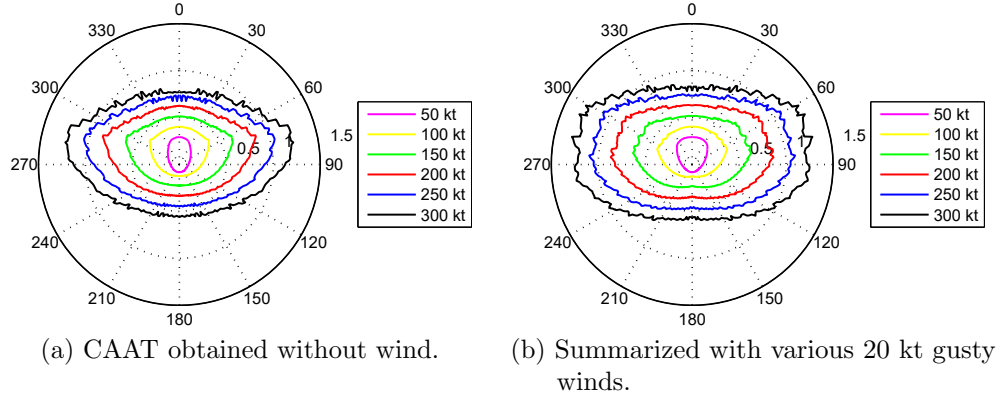


Figure 4.14: Summarized range-based CAAT diagrams (bearing in deg, range in nmi, UA at 75 kt vs. traffic at various airspeeds).

Similar to the wind-summarized WCAT, we reorganize eight sets of CAAT boundaries in Fig. 4.13 into a set of wind-summarized CAAT boundaries in Fig. 4.14b to cover encounters in various wind conditions. In general, the UA front CAAT boundaries in Fig. 4.14b are enlarged in comparison with the ones without wind in Fig. 4.14a. For quantitative comparison between Fig. 4.14a and Fig. 4.14b, we define

$$TCR_{CAAT} = \frac{CAAT_{WIND-SUMMARIZED}}{CAAT_{NO-WIND}} \times 100\% \quad (4.15)$$

Two TCR diagrams of CAAT boundaries on Cartesian coordinates and on polar coordinates are plotted in Fig. 4.15. The TCRs of CAAT boundaries are about 10% to 35% increased between the wind-summarized CAAT and the no-wind CAAT in most bearing angles. Furthermore, Fig. 4.14a and Fig. 4.14b show that UA require longer horizontal ranges to avoid NMACs for traffic from the side regions of UA, such as: $[60^\circ, 120^\circ]$ and $[240^\circ, 300^\circ]$, because during UAS operations they are the most vulnerable bearing regions on CAAT boundaries in various wind conditions.

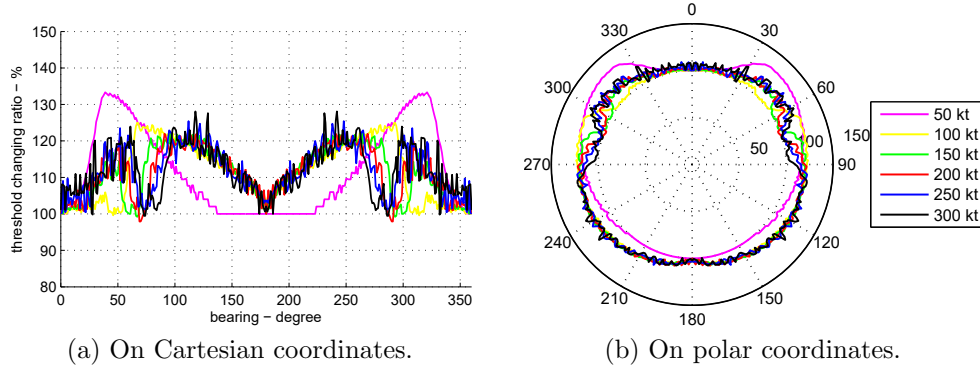


Figure 4.15: Threshold changing ratio diagrams for the impact of CAAT boundaries on wind uncertainties (UA at 75 kt vs. traffic at various airspeeds).

Real-time lookup tables

Two lookup tables are constructed for real-time use on the fast-time simulation platform based on wind-summarized WCAT and CAAT boundaries in Fig. 4.11b and Fig. 4.14b. In MC simulations, traffic at six airspeeds from 50 kt to 300 kt every 50 kt are simulated in the analysis so only six traffic airspeeds are available in lookup tables. Moreover, as shown in Fig. 4.11b and Fig. 4.14b, faster traffic corresponds with larger WCAT or CAAT boundaries of small UA. As a result, a worst-case scenario method is designed to estimate WCAT or CAAT boundaries for small UA at each encounter carried out on the fast-time simulation platform. This worst-case scenario lookup table method is summarized as follows:

1. Locate the airspeed range for traffic, and choose the upper bound as the airspeed for traffic in the lookup table search.
2. Use the rounded traffic detected bearing angle as the index to locate the WCAT or CAAT for small UA in lookup tables.

For example, during a mid-air encounter, the UA is heading to the north (0°) at 75 kt in 20 kt wind, and a traffic aircraft is detected at a bearing angle 32.25° with

a detected horizontal speed at 109.76 kt. Using the worst-case scenario method, we can search the WCAT or CAAT boundary based on the airspeed band 150 kt and the detected bearing angle at 32° in the lookup table. Then, the corresponding WCAT for this encounter is at 2.35 nmi, and the CAAT is at 0.56 nmi.

4.5 Summary

In this chapter, we introduce a series of layered encounter boundaries for small UA to identify hazards with approaching traffic in mid-air encounters, i.e., NMAC, WC, WCAT, CAAT, hazard zone, alert zone, and safe zone. During the implementation of hazard identification, for WCAT and CAAT boundaries that cannot be directly calculated through computable formulas, we design and develop two algorithms to locate them via MC simulations by exhaustively checking the maneuverabilities of small UA with traffic at six airspeeds in various wind conditions. The encounter results in MC simulations have also been saved in the database and summarized into lookup tables for real-time hazard identification on the fast-time simulation platform.

The hazard identification module is implemented for the Avoid System on the fast-time simulation platform in this chapter. The next two chapters will introduce collision risk assessment methods, discuss mitigation strategies in self-separation and collision avoidance, as well as carry out performance evaluations in further detail.

Chapter 5

Risk Assessment

In Chapter 4, we completed the development and implementation of the hazard identification module, the first module of the Avoid System on the fast-time simulation platform. In this chapter, we begin to implement the risk assessment module, the second module of the Avoid System, as the yellow block drawn in the green box in Fig. 5.1. Similar to previous chapters, we first design a set of metrics (mathematical formulas) for small UA to assess collision risk levels from the outer encounter boundary (the encounter surveillance cylinder) to the inner encounter boundary (the NMAC cylinder) as previously depicted in Fig. 4.2. Later, we introduce a statistical risk-ranking method in the implementation to provide robust risk assessment results to overcome uncertainties from sensor measurement errors.

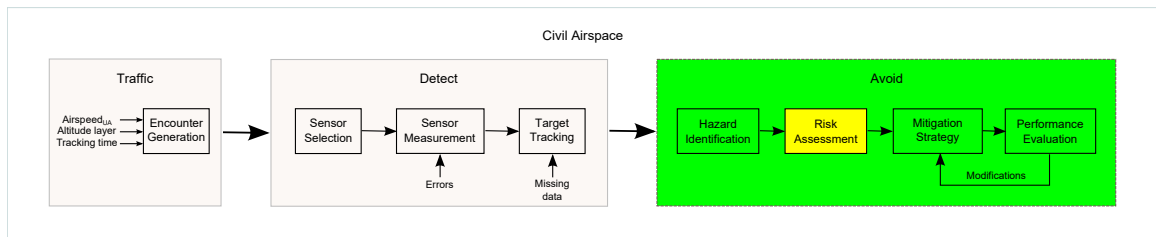


Figure 5.1: Block diagram for the fast-time simulation based analysis platform.

5.1 Introduction

In collision risk analysis, for post-analysis, calculations of probability of potential collisions are straightforward when processing recorded encounter data; however, for prediction, calculations usually rely on probabilistic methods, such as an analytical approximation method [87], a numerical approximation method [103,104], or an MC simulation method [105,106]. These methods typically require intensive computation over a long period of time, thus they are not suitable for real-time analysis. To overcome this drawback, we adopt a geometric method to develop a computable collision risk level evaluation method based on linear projections to carry out collision risk assessment for small UAS in real-time [107,108].

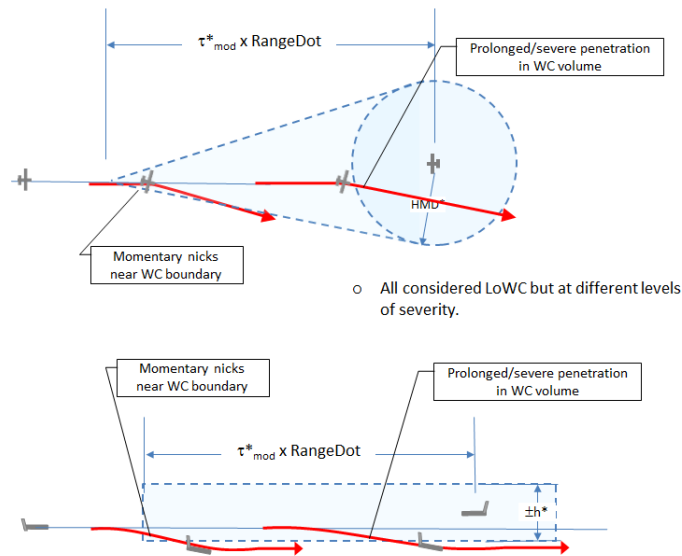


Figure 5.2: Benign momentary nick at the LoWC boundary and prolonged, severe LoWC [2].

As discussed in previous chapters, LoWCs are categorical failures to maintain the separation standard in civil airspace; however, only a few LoWCs will result in NMACs, with determining factor normally being the severities of LoWCs [109]. Thus,

as shown in Fig. 5.2, severity metrics should be alternative solutions to evaluate the collision risks from benign LoWCs to NMACs in mid-air encounters. In [110], the Separation Severity Index (SSI) in Eq. 5.1 has been developed to measure the separation between aircraft at the CPA on predicted trajectories of the UA and traffic.

$$SSI = \min_t \left\{ \max \left[\frac{r(t_i)}{DMOD_{wc}}, \frac{V_s(t_i)}{VMD_{wc}^*} \right] \right\} \quad (5.1)$$

where $t = t_0, t_1, t_2, t_3, \dots, t_{CPA}$, and $t_{CPA} \in [0, 110]$ sec, $DMOD_{wc} = 4000$ ft, and $VMD_{wc}^* = 450$ ft. For $SSI \geq 1$, no LoWC will occur in the next t_{CPA} seconds. For $SSI \in [0, 1)$, LoWC will occur or has occurred and the Severity of Loss of Well Clear (SLoWC) is from 0 (the most severe, i.e., NMAC) to 1 (the least severe, i.e., WC).

As shown in Eq. 5.1, the calculated SSI at t_0 may be equal to the other calculated SSI at t_{CPA} because the time penetration component τ_{mod} is not included in the calculations. However, the SLoWCs at these two timestamps should not be the same as indicated by SSI calculations. For this reason, in Eq. 5.2, the Well Clear Penetration Integral (WCPI) is therefore introduced to calculate the SLoWC based on all three penetration components: the horizontal penetration (HMD), the vertical penetration (V_s), and the time penetration (τ_{mod}) [2].

$$WCPI = \sum_{i=1}^n \min \left(\frac{(DMOD_{wc} - HMD_i)}{DMOD_{wc}}, \frac{(VMD_{wc}^* - V_{s_i})}{VMD_{wc}^*} \right) \frac{(\tau_{mod_{wc}} - \tau_{mod_i})}{\tau_{mod_{wc}}} \Delta t \quad (5.2)$$

where i is the local instance of LoWC, n is the total number of local instances of LoWC, $\tau_{mod_{wc}} = 35$ sec is the modified range tau threshold for LoWC, and Δt is the sensor measurement interval. Through this equation, the calculated WCPI should provide penetration severities for LoWC encounters. Usually, LoWC encounters with

($WCPI < 2$) are benign LoWCs, while encounters with ($WCPI > 10$) are considered significant LoWCs [2]. Thus, penetration severities can be used to represent collision risks for small UA during mid-air encounters.

However, as the sum total is listed in Eq. 5.2, the WCPI is unbounded so that it cannot be normalized into a ratio in $[0, 1]$ to identify the collision risks by a set of consistent risk levels. Moreover, the WCPI is designed to measure the collision risks in LoWCs (i.e., the SLoWC), so it cannot be used for small UA to estimate the collision risks with traffic approaching during the transition period from the beginning of the violation of the alert zone to the LoWC. To overcome these drawbacks, we design a set of new severity metrics in this chapter to assess collision risks in the entire alert zone by extending the penetration control boundary from the WC boundary outbound to the alert zone boundary for the severity of penetrating the alert zone (SPenAZ).

5.2 Severity Metrics for Risk Assessment

According to SLoWC severity metrics discussed in Section 5.1 and WC and alert zone definitions given in Chapter 4, we extend severity calculations from the SLoWC to the SPenAZ for quantifying collision risk levels throughout the period when traffic are penetrating the UA alert zone, which comprise all three local penetration components: the time penetration (τ_{mod}), the horizontal penetration (HMD) and the vertical penetration (V_s), as well as normalize collision risk levels into a bounded range $[0, 1]$ to standardize decision-making for UAS mitigation analysis. Moreover, new severity metrics predict collision risk levels based on the current aircraft states and projections, rather than requiring calculations over the entire projected trajectories of the UA and traffic throughout mid-air encounters, thus they greatly reduce the computation time for the real-time collision risk assessment during mid-air encounters.

In the following subsections, new severity metrics are introduced and designed based upon two independent predictions of collision risk levels: the penetration risk level and the range risk level.

5.2.1 Penetration risk level

Similar to the three local penetration components of τ_{mod} , HMD and V_s used in Definition 2 (WC) and Definition 5 (Alert Zone) in Chapter 4, we design a set of real-time computable equations to quantitatively assess the penetration risk level, $P_{risk}(Penetration)$, for small UA with traffic approaching during mid-air encounters, as follows:

$$P_{risk}(Penetration) = 1 - (\bar{P}_{risk}(\tau_{mod}) \oplus \bar{P}_{risk}(HMD) \oplus \bar{P}_{risk}(V_s)) \quad (5.3)$$

$$\bar{P}_{risk}(\tau_{mod}) = \begin{cases} \min\left(\frac{\tau_{mod} - \tau_{mod_{wc}}^*}{\tau_{mod_{az}}^*}, 1\right) & \text{if } \tau_{mod} > \tau_{mod_{wc}}^*, \\ 1 & \text{if } \tau_{mod} < 0, \\ 0 & \text{Otherwise.} \end{cases} \quad (5.4)$$

$$\bar{P}_{risk}(HMD) = \begin{cases} \min\left(\frac{HMD - R_{NMAC}}{DMOD_{AZ}}, 1\right) & \text{if } HMD > R_{NMAC}, \\ 0 & \text{Otherwise.} \end{cases} \quad (5.5)$$

$$\bar{P}_{risk}(V_s) = \begin{cases} \min\left(\frac{V_s - h_{NMAC}}{VMD_{wc}^* + VMD_{az}^*}, 1\right) & \text{if } V_s > h_{NMAC}, \\ 0 & \text{Otherwise.} \end{cases} \quad (5.6)$$

where: $P_{risk}(Penetration) \in [0, 1]$, $\bar{P}_{risk}(\tau_{mod}) \in [0, 1]$, $\bar{P}_{risk}(HMD) \in [0, 1]$, $\bar{P}_{risk}(V_s) \in [0, 1]$, and

$$P_{risk}(\tau_{mod}) = 1 - \overline{P}_{risk}(\tau_{mod}) \quad (5.7)$$

$$P_{risk}(HMD) = 1 - \overline{P}_{risk}(HMD) \quad (5.8)$$

$$P_{risk}(V_s) = 1 - \overline{P}_{risk}(V_s) \quad (5.9)$$

Note that the Fernandez-Guasti (FG) squircle operators, \oplus , in Eq. 5.3 refer to FG Norm operations used for risk synthesis to combine three normalized penetration components of collision risk levels together. As shown in Eq. 5.10 and Fig. 5.3, the FG Norm operation is better than the multiplication operation ($a \times b$) which always moves toward low values, and also is better than the maximum operation $\max(a, b)$ which does not provide distinction from variation of the lesser component [111].

$$a \oplus b = \sqrt{a^2 + (1 - a^2)b^2} \quad (5.10)$$

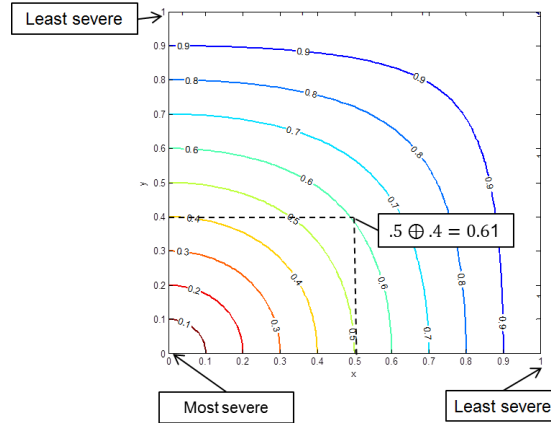


Figure 5.3: A sample FG Norm operation diagram [2].

The FG Norm operation in Eq. 5.10 was originally designed to blend together two normalized components that range from 1 (least severe) to 0 (most severe) [111].

To combine together three normalized components in Eq. 5.3, FG Norm operations should meet the following necessary properties [2, 111],

- $a \oplus b = b \oplus a$ (commutative)
- $a \oplus (b \oplus c) = (a \oplus b) \oplus c$ (associative)
- $1 \oplus a = 1$ for any a
- $0 \oplus a = a$ for any a
- $0 \oplus a = 0$ if and only if $a = 0$

When FG Norm operations meet the above properties among three normalized and inverted risk levels: $\bar{P}_{risk}(\tau_{mod})$, $\bar{P}_{risk}(HMD)$, and $\bar{P}_{risk}(V_s)$, the penetration risk level, $P_{risk}(Penetration)$, can be calculated by Eq. 5.3 with a probability-inverting operation. $[P_{risk}(Penetration) \rightarrow 0]$ refers to a low collision risk level while traffic aircraft start penetrating the UA alert zone, whereas $[P_{risk}(Penetration) \rightarrow 1]$ means that the risk level to a potential NMAC is high. The detailed description for the $P_{risk}(Penetration)$ value range is listed as follows:

Table 5.1: Description for $P_{risk}(Penetration)$ value range

$P_{risk}(Penetration)$	Description for parameter value range
$[0, 0.5)$	Penetrating the alert zone, but always remaining WC
0.5	Penetrating the alert zone, with potential LoWC (on the critical boundary between WC and Benign LoWC)
$(0.5, 1]$	Penetrating the alert zone, with potential LoWC / already LoWC LoWC from the least severe to the most severe (WC to NMAC)

Note that $P_{risk}(Penetration) = 0.5$ is designed and selected as a critical risk level threshold, i.e., $P_{risk}(Threshold)$, to distinguish the collision risks between WC and LoWC. During UAS operations, the PIC can select a preferable risk level threshold

depending on safety concerns and flight missions planned, e.g., $P_{risk}(Threshold) \in [0.45, 0.55]$.

Based on Eq. 5.4, Eq. 5.5, and Eq. 5.6, three function curves of inverted risk levels $\bar{P}_{risk}(\tau_{mod})$, $\bar{P}_{risk}(HMD)$, and $\bar{P}_{risk}(V_s)$ are plotted in Fig. 5.4. In Fig. 5.4a, $\bar{P}_{risk}(\tau_{mod}) = 1$ when traffic are not on the closing geometry with small UA ($\tau_{mod} < 0$ sec) or on the closing geometry but $\tau_{mod} > 145$ sec. $\bar{P}_{risk}(\tau_{mod}) = 0$ when traffic are on the closing geometry and $\tau_{mod} < 35$ sec. $\bar{P}_{risk}(\tau_{mod})$ is on the linear transition from 0 to 1 when $\tau_{mod} \in [35, 145]$ sec; namely, $\bar{P}_{risk}(\tau_{mod})$ is decreasing while τ_{mod} decreases (i.e., when traffic are approaching small UA).

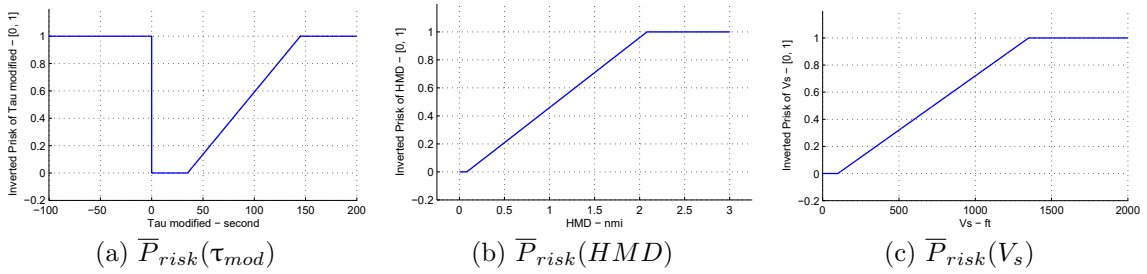


Figure 5.4: Diagrams of $\bar{P}_{risk}(\tau_{mod})$, $\bar{P}_{risk}(HMD)$, and $\bar{P}_{risk}(V_s)$ function curves.

In Fig. 5.4b, $\bar{P}_{risk}(HMD) = 1$ when the projected HMD is larger than 2.08 nmi (2 nmi + 500 ft = 2.08 nmi). $\bar{P}_{risk}(HMD) = 0$ when traffic are projected within the range of 500 ft (0.08 nmi) with small UA on the horizontal plane. $\bar{P}_{risk}(HMD)$ is on the linear transition from 0 to 1 when $HMD \in [0.08, 2.08]$ nmi; namely, $\bar{P}_{risk}(HMD)$ is lower for smaller HMD (i.e., small UA and traffic are projected closer at the CPA on the horizontal plane).

In Fig. 5.4c, $\bar{P}_{risk}(V_s) = 1$ when the vertical separation V_s is larger than 1250 ft. $\bar{P}_{risk}(V_s) = 0$ when traffic are within a 100-ft vertical separation with small UA in altitude. $\bar{P}_{risk}(V_s)$ is on the linear transition from 0 to 1 when $V_s \in [100, 1250]$ ft; namely, $\bar{P}_{risk}(V_s)$ is lower for the smaller vertical separation V_s (i.e., small UA and

traffic are closer on the vertical plane).

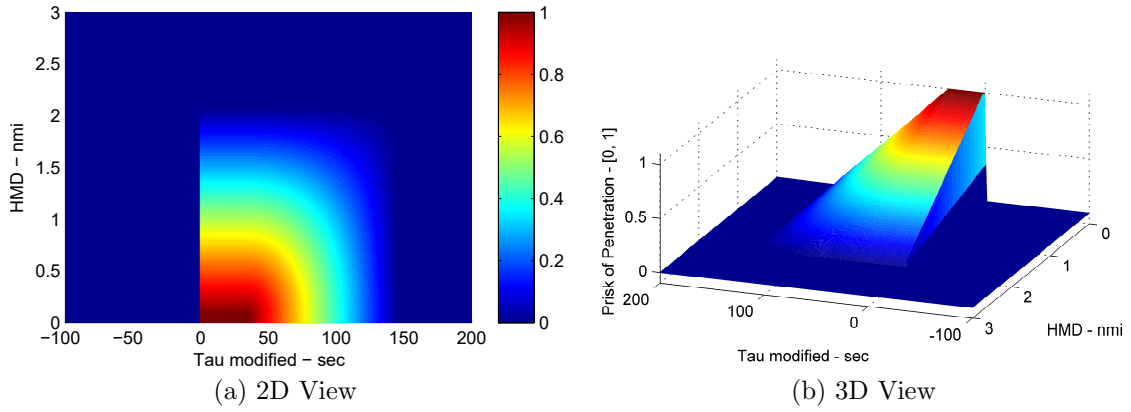


Figure 5.5: Diagrams of $P_{risk}(Penetration)$ for co-altitude encounters.

Moreover, for co-altitude encounters, i.e., $\bar{P}_{risk}(V_s) = 0$, Eq. 5.3 can be rewritten into a simplified equation as follows:

$$P_{risk}(Penetration_{coAlt}) = 1 - (\bar{P}_{risk}(\tau_{mod}) \oplus \bar{P}_{risk}(HMD)) \quad (5.11)$$

The penetration risk levels for co-altitude encounters are plotted on the colormaps in Fig. 5.5, so the change of $P_{risk}(Penetration_{coAlt})$ can be explored through interactions of the closing time τ_{mod} and the horizontal separation HMD between the UA and traffic. For example, when the projected horizontal separation $HMD > 1.1$ nmi, $P_{risk}(Penetration_{coAlt})$ will be below 0.5 (50%) regardless of the closing time τ_{mod} ; when the closing time $\tau_{mod} > 91$ sec, $P_{risk}(Penetration_{coAlt})$ will be below 0.5 (50%) regardless of the horizontal separation HMD .

In addition, to further research the impact of horizontal and vertical separation on collision risks [112], assume that $\bar{P}_{risk}(\tau_{mod}) = 0$, i.e., $\tau_{mod} \in [0, 35]$ sec, then Eq. 5.3 can be rewritten as follows:

$$P_{risk}(Penetration_{separation}) = 1 - (\bar{P}_{risk}(HMD) \oplus \bar{P}_{risk}(V_s)) \quad (5.12)$$

The penetration risk levels by the separation are plotted in the colormaps in Fig. 5.6, so the change of $P_{risk}(Penetration_{separation})$ can be explored through interactions of the horizontal separation HMD and the vertical separation V_s between the UA and traffic. For example, when the projected horizontal separation $HMD > 1.1$ nmi, $P_{risk}(Penetration_{separation})$ will be lower than 0.50 (50%) regardless of the vertical separation V_s ; when the vertical separation $V_s > 730$ ft, $P_{risk}(Penetration_{separation})$ will be lower than 0.50 (50%) regardless of the horizontal separation HMD .

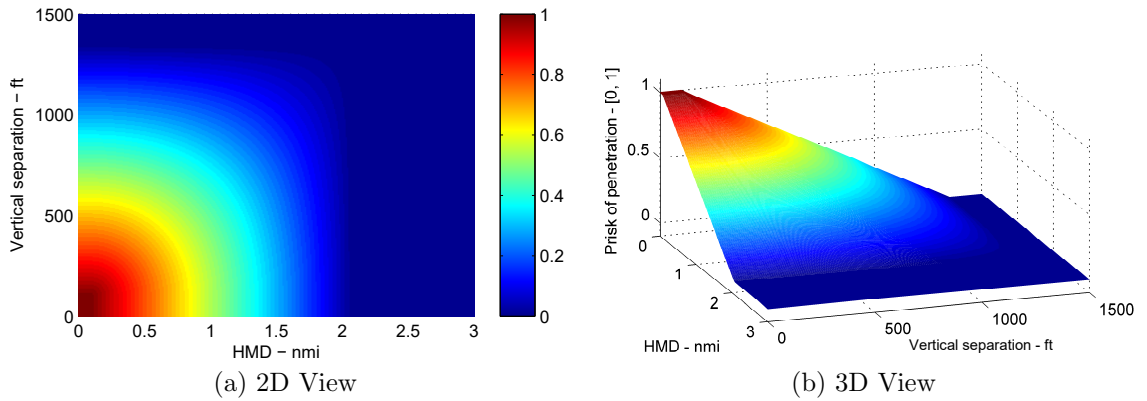


Figure 5.6: Diagrams of $P_{risk}(Penetration)$ without $P_{risk}(\tau_{mod})$.

5.2.2 Range risk level

For most head-on encounters, the penetration risk level $P_{risk}(Penetration)$ in Eq. 5.3 can be used to evaluate collision risk levels between the UA and traffic; however, for tail-chase encounters with very small closing velocities, τ_{mod} may still be larger than $\tau_{mod_{AZ}}^*$ (110 sec), even when traffic aircraft close to the UA $DMOD_{wc}$ boundary (4000 ft), e.g., a tail-chase encounter with a UA at 75 kt and traffic at 76kt (i.e., a UA overtaken encounter with a 1 kt closing velocity). Thus, the calculated penetration risk level cannot be used to represent collision risk levels for encounters with small closing velocities. To remedy this issue, we introduce a new severity metric, the range

risk level, $P_{risk}(Range)$, to evaluate collision risks based on the horizontal range r regardless of the τ_{mod} calculated during mid-air encounters.

$$P_{risk}(Range) = \begin{cases} 1 - \min\left(\frac{r - 2DMOD_{wc}}{2DMOD_{wc}}, 1\right) & \text{if } r > 2DMOD_{wc} \text{ and } V_s \leq VMD_{AZ}^*, \\ 1 & \text{if } r \leq 2DMOD_{wc} \text{ and } V_s \leq VMD_{AZ}^*, \\ 0 & \text{Otherwise.} \end{cases} \quad (5.13)$$

where $P_{risk}(Range) \in [0, 1]$, $DMOD_{wc} = 4000$ ft, $VMD_{AZ}^* = 800$ ft, r is the current horizontal range between the UA and traffic (obtained by Eq. 2.9), and V_s is the current vertical separation between the UA and traffic (obtained by Eq. 2.3).

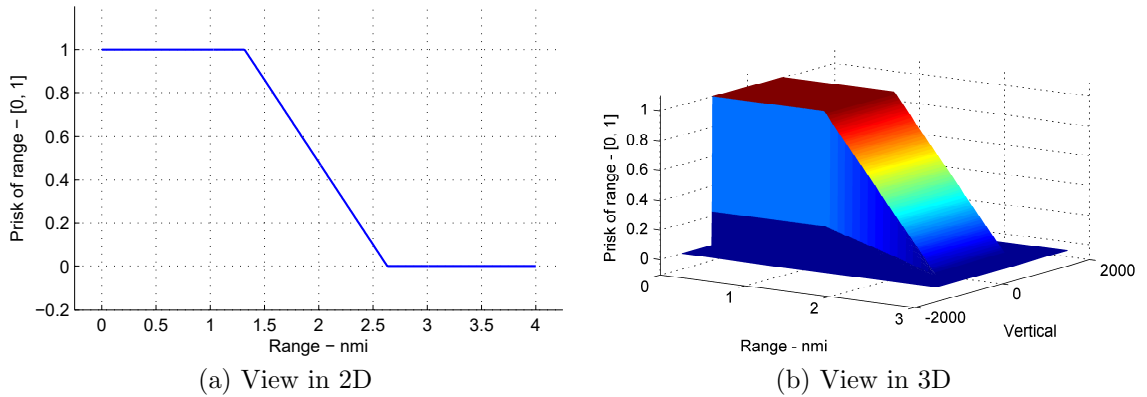


Figure 5.7: Diagrams of $P_{risk}(Range)$ function curves.

Fig. 5.7 shows the function curve of $P_{risk}(Range)$ when the vertical separation $V_s \leq 800$ ft. Namely, $P_{risk}(Range) = 0$ when the horizontal range between the UA and traffic is larger than 2.63 nmi (16000 ft); $P_{risk}(Range) = 1$ when the horizontal range between the UA and traffic is within 1.32 nmi (8000 ft); $P_{risk}(Range)$ is on the linear transition from 1 to 0 when $r \in [1.32, 2.63]$ nmi ([8000, 16000] ft); and $P_{risk}(Range) = 0.5$ when the horizontal range between the UA and traffic is at 2 nmi (12000 ft), which is equal to the minimum horizontal range of the UA alert zone, $DMOD_{AZ}$.

5.3 Implementation Methodology

As designed for the fast-time process, the penetration risk level $P_{risk}(Penetration)$ in Eq. 5.3 and the range risk level $P_{risk}(Range)$ in Eq. 5.13 are calculated based on current estimated aircraft states and projections; thus, as shown by the blue curve drawn in Fig. 5.8b, the penetration risk level assessed for traffic on the EKF-estimated trajectory in Fig. 5.8a varies a lot throughout a simulated mid-air encounter. This shows that the penetration risk level $P_{risk}(Penetration)$ is sensitive to projections of the current τ_{mod} and HMD (i.e., relative heading angles estimated between the UA and traffic which lead to projection errors). To solve this problem, a risk-ranking method based on likelihood statistical analysis [113] is developed in this section to provide robust risk assessment results for the next module, mitigation strategy, on the fast-time simulation platform.

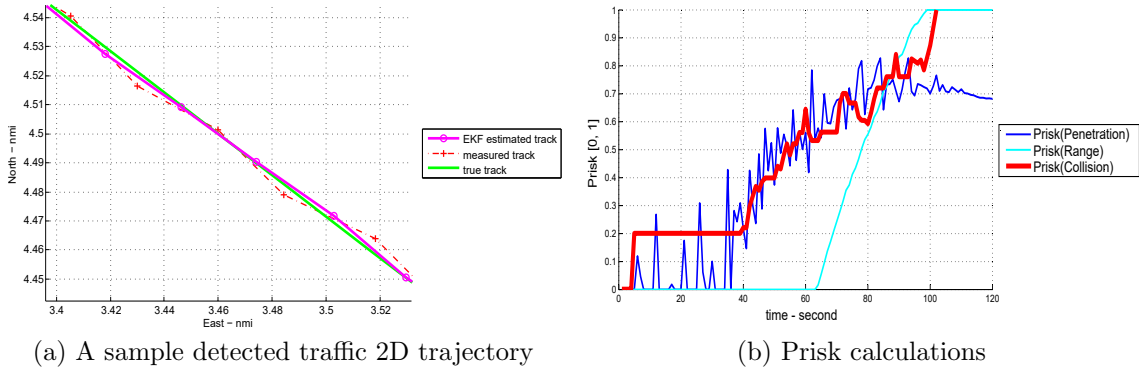


Figure 5.8: Diagrams of P_{risk} calculations based on sensor measurements.

Penetration risk ranking

A collision risk-ranking table is designed in Table 5.2, where five rows refer to five risk level categories: Insignificant, Minor, Moderate, Major, and Catastrophic; five columns indicate five likelihood options of detected risk levels: Rare, Unlikely, Possible, Likely,

and Certain; the probability range numbers (e.g., Moderate [0.45, 0.7], or Unlikely [15%,45%]) are set for these risk level categories and likelihood options based on previously successful risk-ranking analysis results obtained on the fast-time simulation platform; 25 risk ranks are assigned in the table from 1 (bottom left) to 50 (top right) based upon both the risk level and the likelihood; low collision risk ranks are displayed in green; catastrophic collision risk ranks are displayed in brown; and high collision risk ranks are displayed in red.

Table 5.2: Collision Risk Ranking Table

Likelihood Risk Level	Rare [0%, 15%]	Unlikely [15%, 45%]	Possible [45%, 55%]	Likely [55%, 85%]	Certain [85%, 100%]
Catastrophic [0.9, 1.0]	22	38	46	48	50
Major [0.7, 0.9]	18	26	36	42	45
Moderate [0.45, 0.7]	15	22	27	32	35
Minor [0.2, 0.45]	7	12	16	22	24
Insignificant [0.0, 0.2]	1	4	6	8	10

As per the ranking process summarized in Eq. 5.14, the ranked penetration risk level is determined by the likelihood analysis of the last ten penetration risk levels calculated at time steps ($n - 9, n - 8, \dots, n - 2, n - 1, \text{ and } n$). Namely, the rank “1” is assigned when only one measurement has the penetration risk level in [0.0, 0.2) in the last ten measurements; the rank “27” is assigned when five measurements have penetration risk levels in [0.45, 0.7) in the last ten measurements; and the rank “50” is assigned when all ten measurements have risk levels in [0.9, 1.0].

$$P_{risk}(Penetration_{ranked}) = \sum_{i=1}^5 \frac{Rank(i)Num_{P_{risk}}(i)}{50 \times 10} \quad (5.14)$$

where:

- i is the index of five penetration risk level categories (i.e., 1 for Insignificant, 2 for Minor, 3 for Moderate, 4 for Major, and 5 for Catastrophic in Table 5.2).
- $Rank(i)$ is the rank value assigned based on the risk level category and the likelihood of $P_{risk}(Penetration)$. For example, the Minor risk level, $Rank(2)$, is assigned to “16” when five calculated penetration risk levels $P_{risk}(Penetration)$ are in the risk level range $[0.2, 0.45)$ in the last ten calculations (50% likelihood).
- $Num_{P_{risk}}(i)$ is the number of calculated penetration risk levels $P_{risk}(Penetration)$ found in each risk level category from the last ten $P_{risk}(Penetration)$ calculations at time steps $(n - 9, n - 8, \dots, n - 2, n - 1, \text{ and } n)$, and $\sum_{i=1}^5 Num_{P_{risk}}(i) = 10$.

Range risk ranking

Similar to calculations of ranked penetration risk levels, calculations of ranked range risk levels are also based on the ranking table method. The ranks in the range risk-ranking table in Table 5.3 are modified, because the value changes in calculated range risk levels in Eq. 5.13 are usually small in comparison with the changes in calculated penetration risk levels. Furthermore, for the fast response on range risk ranking, only the last four range risk levels at time steps $(n - 3, n - 2, n - 1, \text{ and } n)$ are used in calculations of ranked range risk levels.

$$P_{risk}(Range_{ranked}) = \sum_{i=1}^5 \frac{Rank(i)Num_{P_{risk}}(i)}{50 \times 4} \quad (5.15)$$

where:

- i is the index of five penetration risk level categories (i.e., 1 for Insignificant, 2 for Minor, 3 for Moderate, 4 for Major, and 5 for Catastrophic in Table 5.3).

- $Rank(i)$ is the rank value assigned based on the risk level category and the likelihood of $P_{risk}(Penetration)$.
- $Num_{P_{risk}}(i)$ is the number of calculated penetration risk levels $P_{risk}(Penetration)$ found in each risk level category from the last four $P_{risk}(Penetration)$ calculations at time steps $(n - 3, n - 2, n - 1, \text{ and } n)$, and $\sum_{i=1}^5 Num_{P_{risk}}(i) = 4$.

Table 5.3: Range Risk Ranking Table

Likelihood Risk Level	Rare [0%, 15%]	Unlikely [15%, 45%]	Possible [45%, 55%]	Likely [55%, 85%]	Certain [85%, 100%]
Catastrophic [0.9, 1.0]	18	21	46	48	50
Major [0.7, 0.9]	16	26	32	42	45
Moderate [0.45, 0.7]	12	18	25	26	30
Minor [0.2, 0.45]	6	10	16	22	24
Insignificant [0.0, 0.2]	1	2	6	12	16

Collision risk ranking

The collision risk level, $P_{risk}(Collision)$, can be defined as

$$P_{risk}(Collision) = \max (P_{risk}(Penetration_{ranked}), P_{risk}(Range_{ranked})) \quad (5.16)$$

In Eq. 5.16, the collision risk level is determined by the larger one between two independent risk levels: the ranked penetration risk level $P_{risk}(Penetration_{ranked})$ in Eq. 5.14 and the ranked range risk level $P_{risk}(Range_{ranked})$ in Eq. 5.15. Finally, as shown in Fig. 5.8b, the change of the ranked $P_{risk}(Collision)$ (the red curve) is small in comparison with the change of calculated $P_{risk}(Penetration)$ (the blue curve), and thus the ranked $P_{risk}(Collision)$ can be used to provide robust collision risk assessment on the fast-time simulation platform.

5.4 Risk Assessment Performance Analysis

Table 5.4: Summary of encounter geometries [2]

Geometric Classification	Icon Description
Head-On	
UA Overtaken	
UA Overtaking	
Left Oblique UA Overtaking	
Right Oblique UA Overtaking	
Left-Converging Traffic	
Right-Converging Traffic	

Legend: UA in blue and traffic in red.

In this section, we start to analyze the risk assessment performance using the developed severity metrics on listed encounter geometries in Table 5.4. As with the design of metrics, the collision risk level $P_{risk}(Collision)$ is normalized into $[0, 1]$ to assess collision risks from the least severe at 0 (WC) to the most severe at 1 (NMAC). Based on this normalization, a risk level threshold $P_{risk}(Threshold)$ is selected in the analysis to control the sensitivity of the mitigation triggering process for the Avoid System on the fast-time simulation platform.

In default, $P_{risk}(Threshold) = 0.5$, i.e., the mitigation module is activated to provide the maneuvering guidance when $P_{risk}(Collision) > 0.5$. For example, using this threshold and the developed severity metrics, we can obtain UA mitigation triggering conditions for two sample encounters, where the UA in encounter 2 initiates a self-separation maneuver 10 seconds earlier than the UA in encounter 1 due to the higher collision risk level.

1. Benign LoWC encounter: the mitigation process is triggered to avoid a potential LoWC when $\tau_{mod} < 68$ sec, $HMD_{projected} = 0.65$ nmi (3950 ft $\approx DMOD_{wc}$), and $V_s = 475$ ft ($\approx VMD_{wc}^*$).
2. Severe LoWC encounter: the mitigation process is triggered to avoid the potential LoWC when $\tau_{mod} < 78$ sec, $HMD_{projected} = 0.31$ nmi (1900 ft), and $V_s = 475$ ft ($\approx VMD_{wc}^*$).

In the following subsections, we choose five typical left-side encounters from the encounter geometries summarized in Table 5.4 to initiate 500 mid-air encounters on the fast-time simulation platform, and perform further analysis on collision risk assessment for the developed severity metrics. Note that for encounters on both the left encounter geometries and the corresponding right encounter geometries, the developed severity metrics will give the same triggering results because of encounter symmetries.

5.4.1 Head-On

As shown in Fig. 5.9a, in a head-on encounter, the UA in blue is heading to the north, the traffic aircraft in red is heading the south, and their initial conditions are: the detected traffic bearing at 0 deg (the north), the traffic heading at 179 deg (the south), the south wind (0 deg) at 20 kt, the UA ground speed at 95 kt, and the traffic ground

speed at 100 kt. A set of sample P_{risk} curves are drawn in Fig. 5.9b, where the red curve depicts the collision risk level $P_{risk}(Collision)$ over the evaluation time $[0, 120]$ sec. Upon the output performance, it is a much smoother control curve in comparison with the blue curve of the penetration risk level $P_{risk}(Penetration)$ in Fig. 5.9b.

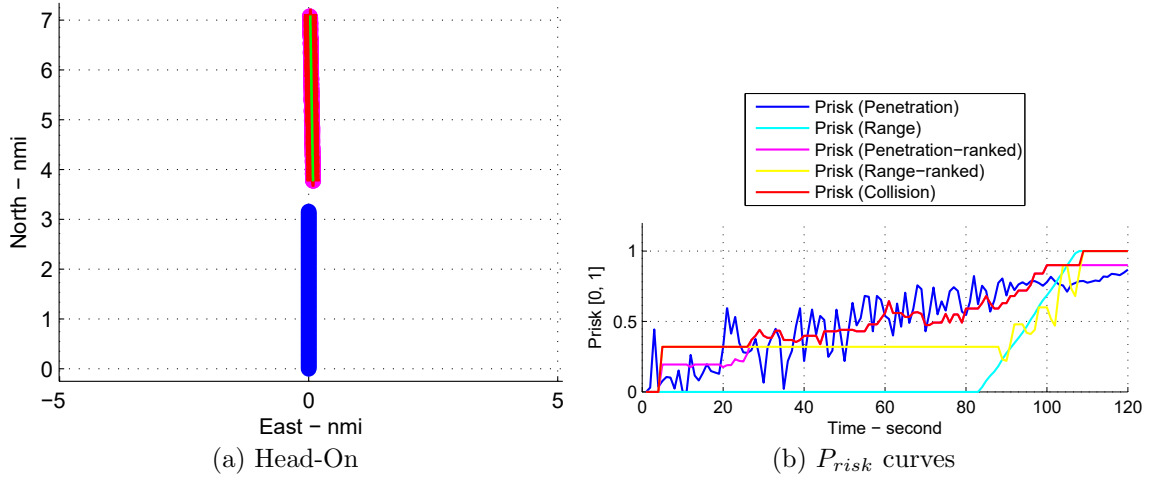


Figure 5.9: P_{risk} collision risk analysis for a head-on encounter.

As shown in the implementation block diagram in Fig. 3.3, measurement errors are introduced in the sensor measurement module, and detected traffic trajectories are tracked and smoothed by the EKF in the tracking module. With this simulated detection process, 100 head-on encounters in Fig. 5.9a are generated on the fast-time simulation platform, and at the same time the risk assessment performance of the developed severity metrics is analyzed. Table 5.5 lists analysis results at the first breach of $P_{risk}(Collision) > 0.5$ for these head-on encounters, where the two-sigma rule (2 standard deviations) is used to calculate 95% containment for each statistical result. Upon analysis of the results of these head-on encounters, the DAA mitigation process is usually triggered to provide mitigation guidance to avoid the potential LoWC when the horizontal range $r < 4.63$ nmi (or the closing time $\tau_{mod} < 83.52$ sec), which is outside of the WCAT boundary (2.38 nmi, as per the WCAT lookup table

obtained in Chapter 4).

Table 5.5: Analysis results for encounters on the head-on geometry.

Statistic	Unit	N	Mean	95% Containment	Standard Deviation	Min	Max
range (r)	nmi	100	4.63	± 0.38	0.19	3.20	4.86
range rate (\dot{r})	kt	100	-195.90	± 18.90	9.44	-237.43	-177.65
time (τ_{mod})	sec	100	83.52	± 11.16	5.58	50.35	91.18
horizontal separation (HMD)	nmi	100	0.18	± 0.30	0.15	0.00	0.71
vertical separation (V_s)	ft	100	354.82	± 40.34	20.67	304.27	412.44
$P_{risk}(Penetration_{ranked})$		100	0.52	± 0.0032	0.0016	0.52	0.54
$P_{risk}(Range_{ranked})$		100	0.32	± 0.0000	0.0000	0.32	0.32
$P_{risk}(Collision)$		100	0.52	± 0.0032	0.0016	0.52	0.54

5.4.2 UA Overtaken

As shown in Fig. 5.10a, in a UA overtaken encounter, the UA in blue is heading to the north, the traffic aircraft in red is heading the northeast with a faster velocity, and their initial conditions are: the detected traffic bearing at 228 deg (the southwest), the traffic heading at 17 deg (the northeast), the south wind (0 deg) at 20 kt, the UA ground speed at 95 kt, and the traffic ground speed at 122 kt. A set of sample P_{risk} curves are drawn in Fig. 5.10b, where the red curve depicts the collision risk level $P_{risk}(Collision)$ over the evaluation time $[0, 120]$ sec.

Similar to the performance analysis of previous head-on encounters, risk assessment results for UA overtaken encounters at the first breach of $P_{risk}(Collision) > 0.5$ in 100 runs on the fast-time simulation platform are listed in Table 5.6. In this encounter geometry, the DAA mitigation process is triggered to provide mitigation guidance to avoid the potential LoWC by the breach of the ranked range risk level $P_{risk}(Range_{ranked})$ (i.e., $r < 2$ nmi and $V_s < 800$ ft regardless of the time τ_{mod}). At the triggering time, the ranked penetration risk level $P_{risk}(Penetration_{ranked})$ indeed stays small because the closing time τ_{mod} is larger than 110 sec. Moreover, the DAA

triggering location is also outside of the WCAT boundary (1.43 nmi, based on the WCAT lookup table obtained in Chapter 4).

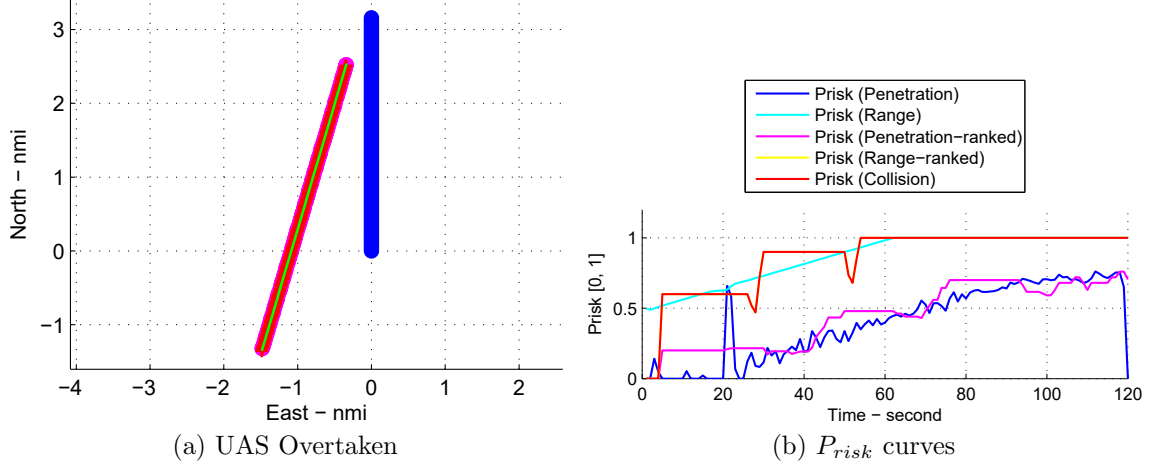


Figure 5.10: P_{risk} collision risk analysis for a UA overtaken encounter.

Table 5.6: Analysis results for encounters on the UA overtaken geometry.

Statistic	Unit	N	Mean	95% Containment	Standard Deviation	Min	Max
range (r)	nmi	100	1.95	± 0.0068	0.0034	1.94	1.96
range rate (\dot{r})	kt	100	-40.47	± 27.53	13.77	-76.00	2.15
time (τ_{mod})	sec	100	147.78	± 651.68	325.84	-2894.65	929.30
horizontal separation (HMD)	nmi	100	0.52	± 0.81	0.41	0.01	1.95
vertical separation (V_s)	ft	100	436.95	± 38.29	19.14	391.25	477.12
$P_{risk}(Penetration_{ranked})$		100	0.20	± 0.0019	0.01	0.17	0.22
$P_{risk}(Range_{ranked})$		100	0.60	± 0.0000	0.00	0.60	0.60
$P_{risk}(Collision)$		100	0.60	± 0.0032	0.00	0.60	0.60

5.4.3 UA Overtaking

As shown in Fig. 5.11a, in a UA overtaking encounter, the UA in blue is heading to the north, the traffic aircraft in red is heading the north with a slower velocity, and their initial conditions are: the detected traffic bearing at 357 deg (the north), the traffic heading at 359 deg (the north), the south wind (0 deg) at 20 kt, the UA

ground speed at 95 kt, and the traffic ground speed at 70 kt. A set of sample P_{risk} curves are drawn in Fig. 5.11b, where the red curve depicts the collision risk level $P_{risk}(Collision)$ over the evaluation time $[0, 120]$ sec.

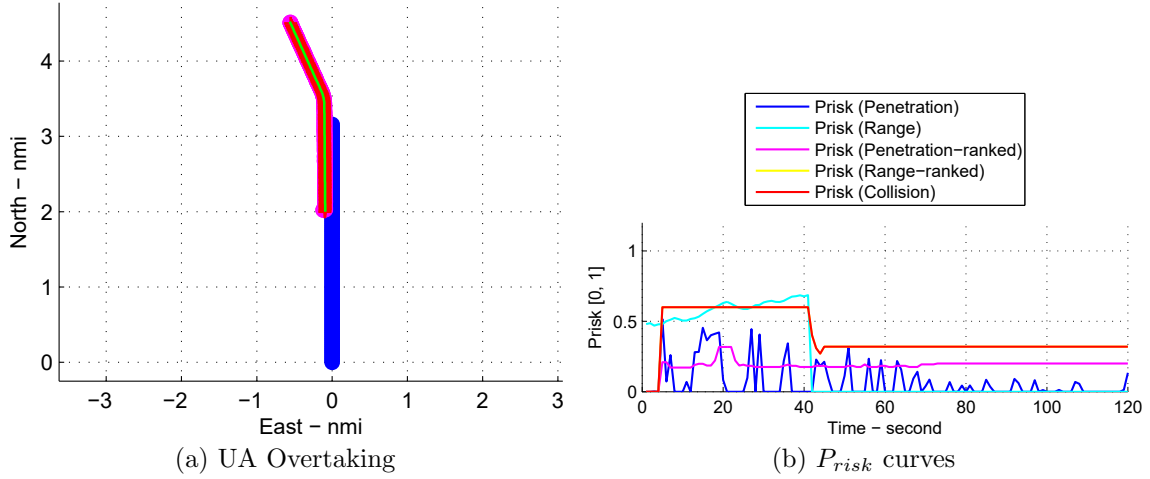


Figure 5.11: P_{risk} collision risk analysis for a UA overtaking encounter.

Table 5.7: Analysis results for encounters on the UA overtaking geometry.

Statistic	Unit	N	Mean	95% Containment	Standard Deviation	Min	Max
range (r)	nmi	100	1.98	± 0.008	0.004	1.96	1.99
range rate (\dot{r})	kt	100	-23.55	± 20.73	10.37	-54.49	5.93
time (τ_{mod})	sec	100	164.12	± 2292.91	1146.45	-9355.26	2231.20
horizontal separation (HMD)	nmi	100	0.64	± 1.09	0.55	0.00	1.98
vertical separation (V_s)	ft	100	513.10	± 36.92	18.46	455.93	549.71
$P_{risk}(Penetration_{ranked})$		100	0.20	± 0.0133	0.007	0.17	0.22
$P_{risk}(Range_{ranked})$		100	0.60	0.00	0.00	0.60	0.60
$P_{risk}(Collision)$		100	0.60	0.00	0.00	0.60	0.60

Similar to the performance analysis of the previous encounters, risk assessment results for UA overtaking encounters at the first breach of $P_{risk}(Collision) > 0.5$ in 100 runs on the fast-time simulation platform are listed in Table 5.7. In this encounter geometry, the DAA mitigation process is triggered to provide mitigation guidance to avoid the potential LoWC by the breach of the ranked range risk level $P_{risk}(Range_{ranked})$ (i.e., $r < 2$ nmi and $V_s < 800$ ft regardless of the time τ_{mod}). At

the triggering time, the ranked penetration risk level $P_{risk}(Penetration_{ranked})$ indeed stays small because of the low closing velocity between the UA and traffic (-23.55 kt) and the large τ_{mod} ($\tau_{mod} > 110$ sec). Moreover, the DAA triggering location is also outside of the WCAT boundary (1.51 nmi, based on the WCAT lookup table obtained in Chapter 4).

5.4.4 Left Oblique UA Overtaking

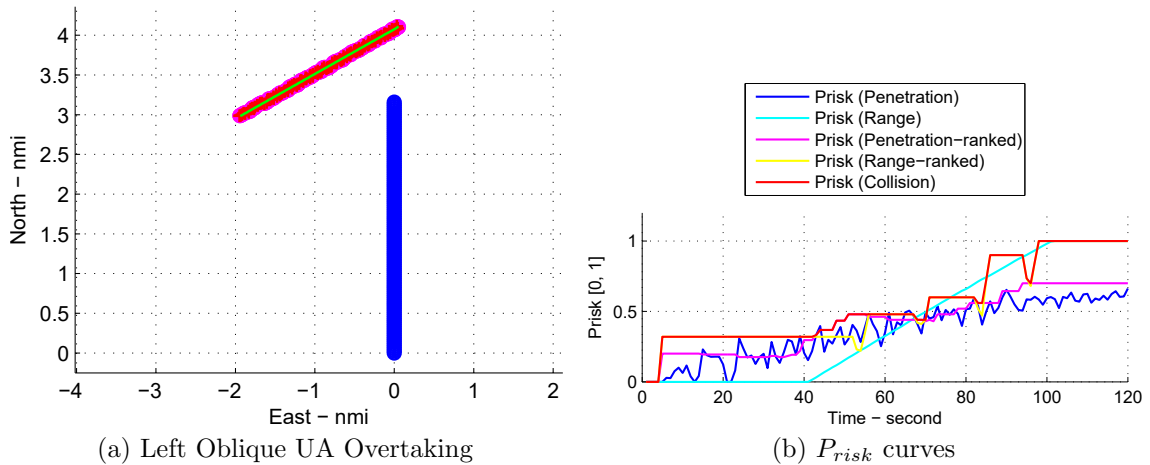


Figure 5.12: P_{risk} collision risk analysis for left oblique UA overtaking encounters.

As shown in Fig. 5.12a, in a left oblique UA overtaking encounter, the UA in blue is heading to the north, the traffic aircraft in red is heading the northeast with a slower velocity, and their initial conditions are: the detected traffic bearing at 327 deg (the northwest), the traffic heading at 61 deg (the northeast), the south wind (0 deg) at 20 kt, the UA ground speed at 95 kt, and the traffic ground speed at 76 kt. A set of sample P_{risk} curves are drawn in Fig. 5.12b, where the red curve depicts the collision risk level $P_{risk}(Collision)$ over the evaluation time [0, 120] sec.

Similar to the performance analysis of previous UA overtaking encounters, risk assessment results for left oblique UA overtaking encounters at the first breach of

$P_{risk}(Collision) > 0.5$ in 100 runs on the fast-time simulation platform are listed in Table 5.8. In this encounter geometry, the DAA mitigation process is triggered to provide mitigation guidance to avoid the potential LoWC by the breach of the ranked range risk levels $P_{risk}(Range_{ranked})$ (i.e., $r < 2$ nmi and $V_s < 800$ ft). At the triggering time, the ranked penetration risk level is less than the threshold 0.5, but it almost reaches 0.5 with $P_{risk}(Penetration_{ranked}) = 0.42$, range rate $\dot{r} = -80.59$ kt and closing time $\tau_{mod} = 80$ sec. Moreover, the DAA triggering location is outside the WCAT boundary (1.93 nmi, based on the WCAT lookup table obtained in Chapter 4).

Table 5.8: Analysis results for encounters on the left oblique UA overtaking geometry.

Statistic	Unit	N	Mean	95% Containment	Standard Deviation	Min	Max
range (r)	nmi	100	1.96	± 0.0132	0.0066	1.95	1.99
range rate (\dot{r})	kt	100	-80.59	± 23.77	11.89	-137.81	-49.43
time (τ_{mod})	sec	100	79.27	± 22.50	11.25	46.33	126.16
horizontal separation (HMD)	nmi	100	0.76	± 0.44	0.22	0.03	1.40
vertical separation (V_s)	ft	100	402.15	± 44.99	22.50	338.40	458.93
$P_{risk}(Penetration_{ranked})$		100	0.42	± 0.10	0.05	0.24	0.52
$P_{risk}(Range_{ranked})$		100	0.60	0.00	0.00	0.60	0.60
$P_{risk}(Collision)$		100	0.60	0.00	0.00	0.60	0.60

5.4.5 Left-Converging Traffic

As shown in Fig. 5.13a, in a left-converging traffic encounter, the UA in blue is heading to the north, the traffic aircraft in red is heading the southeast, and their initial conditions are: the detected traffic bearing at 327 deg (the northwest), the traffic heading at 125 deg (the southeast), the south wind (0 deg) at 20 kt, the UA ground speed at 95 kt, and the traffic ground speed at 136 kt. A set of sample P_{risk} curves are drawn in Fig. 5.13b, where the red curve depicts the collision risk level $P_{risk}(Collision)$ over the evaluation time [0, 120] sec.

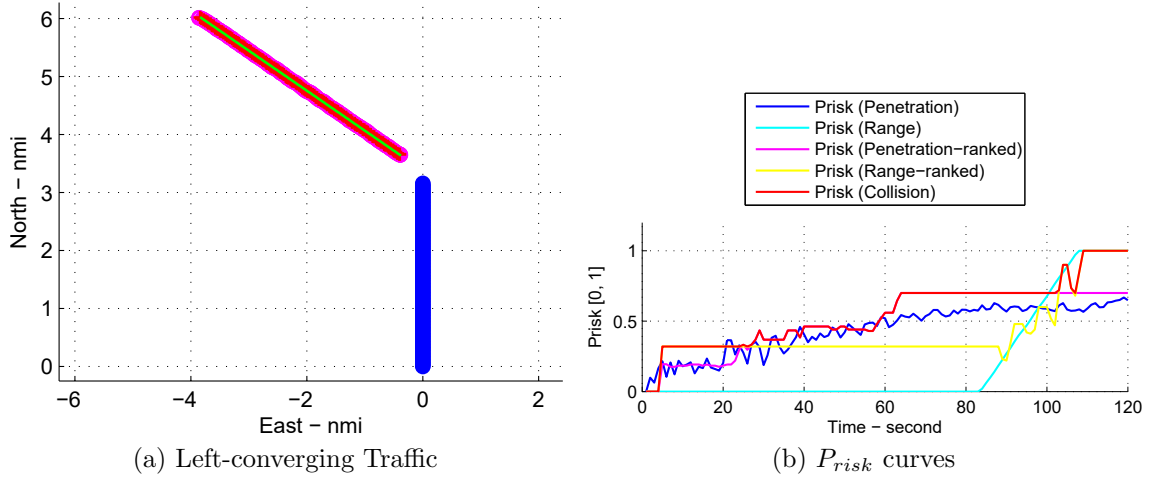


Figure 5.13: P_{risk} collision risk analysis for a left-converging traffic encounter.

Table 5.9: Analysis results for encounters with traffic on the left-converging geometry.

Statistic	Unit	N	Mean	95% Containment	Standard Deviation	Min	Max
range (r)	nmi	100	3.97	± 0.35	0.17	3.37	4.23
range rate (\dot{r})	kt	100	-197.30	± 18.68	9.34	-235.31	-172.00
time (τ_{mod})	sec	100	70.63	± 9.45	4.72	55.17	80.68
horizontal separation (HMD)	nmi	100	0.13	± 0.22	0.11	0.00	0.46
vertical separation (V_s)	ft	100	603.46	± 40.38	20.19	562.50	646.99
$P_{risk}(Penetration_{ranked})$		100	0.52	0.00	0.00	0.52	0.52
$P_{risk}(Range_{ranked})$		100	0.32	0.00	0.00	0.32	0.32
$P_{risk}(Collision)$		100	0.52	0.00	0.00	0.52	0.52

Similar to the performance analysis of previous head-on encounters, risk assessment results for left-converging traffic encounters at the first breach of $P_{risk}(Collision) > 0.5$ in 100 runs on the fast-time simulation platform are listed in Table 5.9. In this encounter geometry, the DAA mitigation process is triggered to provide mitigation guidance to avoid the potential LoWC by the breach of the ranked penetration risk level $P_{risk}(Penetration_{ranked})$ when the horizontal range $r < 3.97$ nmi (or the closing time $\tau_{mod} < 70.63$ sec), which is outside of the WCAT boundary (1.90 nmi, based on the WCAT lookup table obtained in Chapter 4).

5.5 Summary

In this chapter, we develop a new set of severity metrics to assess collision risk levels for small UA when traffic are penetrating from the outer encounter boundary (encounter surveillance cylinder) to the inner encounter boundary (NMAC cylinder), which are based on three penetration components: the closing time τ_{mod} , the horizontal separation HMD , and the vertical separation V_s . To overcome uncertainties from sensor measurements, a risk-ranking table method is also designed and introduced to provide robust risk assessment results for mitigation analysis. For the performance analysis, encounters on various geometries are performed on the fast-time simulation platform, and the analysis results show that the developed risk assessment metrics can be employed to evaluate potential collision risks and trigger the mitigation process during mid-air encounters.

With hazards identified in Chapter 4 and collision risks assessed in this chapter, the other two modules of the Avoid System, the mitigation strategy module and the performance analysis module, will be developed in the next chapter. The development will be focused on two types of mitigation strategies in UAS self-separation and collision avoidance, as well as the mitigation performance analysis metrics used on the fast-time simulation platform.

Chapter 6

Mitigation Analysis

In Chapter 4 and Chapter 5, we completed the development of the hazard identification module and the risk assessment module, the first two modules of the Avoid System on the fast-time simulation platform. In this chapter, we begin to implement the last two modules of the Avoid System, the mitigation strategy module and the performance evaluation module, as shown in the orange block and the pink block drawn in the green box in Fig. 6.1.

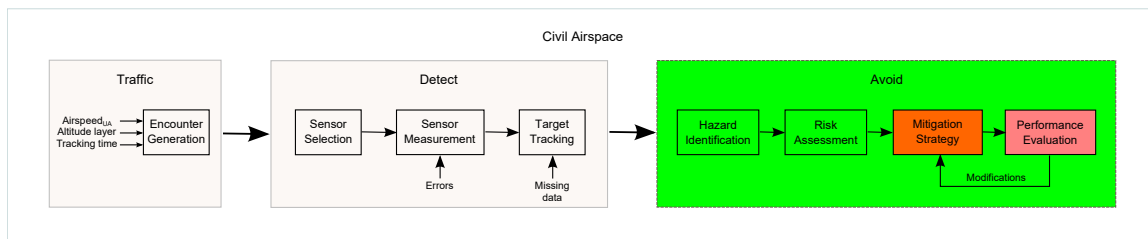


Figure 6.1: Block diagram for the fast-time simulation based analysis platform.

Two categories of mitigation strategies are developed in this chapter for self-separation and collision avoidance. In self-separation, a learning-based decision tree method is proposed to provide DAA guidance for small UA to avoid LoWCs or NMACs during mid-air encounters. In collision avoidance, a three-dimensional emergency evasive maneuvering algorithm is designed for small UA to avoid coming NMACs

when traffic are approaching the CAAT boundary in the hazard zone during mid-air encounters. Later in this chapter, to evaluate the mitigation performance of DAA systems, a set of risk ratio metrics are developed to perform statistical analysis over millions of simulated mid-air encounters on the fast-time simulation platform.

6.1 Introduction

As with the near-term solutions proposed in Chapter 1, for safety concerns about UAS operations in civil airspace, the PIC should make final decisions on whether maneuvers are required during mid-air encounters to avoid potential LoWCs or NMACs; however, it is not an easy task for the PIC, even an experienced pilot, to make such decisions for safe operations in civil airspace due to the complexities of mid-air encounter geometries, and uncertainties of sensor measurements on aircraft states such as traffic-detected bearings, headings, velocities, and accelerations, as well as on encountered environmental conditions, i.e., wind speed and wind direction. For example, when traffic are converging from the left rear of UA at the bearing region $[250^\circ, 265^\circ]$, as shown in Fig. 4.11 and Fig. 4.12, the WCAT is increased almost 25% in various wind conditions for UA operated at 75 kt, which often results in LoWCs because of inappropriate maneuvers chosen by the PIC based on previously successful experience from similar encounter geometries. As a result, a DAA guidance system is required to help the PIC assess collision risks quantitatively and make appropriate maneuvers to avoid potential LoWCs or NMACs in mid-air encounters.

For large UAS, the TCAS can be installed as a proven DAA guidance system to help the PIC make appropriate maneuvers to avoid potential collisions during mid-air encounters. For small UAS, the TCAS cannot be installed due to SWaP limitations. A light-weight ADS-B-based airborne DAA system and a portable ground

radar-based DAA system are therefore proposed in Chapter 1 to help small UAS choose appropriate horizontal maneuvers¹ to avoid LoWCs in UAS self-separation, and achieve the equivalent level of safety as manned aircraft in civil airspace. However, when self-separation fails (i.e., traffic have breached the hazard zone and are approaching the UA CAAT boundary), DAA guidance systems in collision avoidance are allowed to maneuver UA in any way in the three-dimensional space that is safe to avoid NMACs.

As regards the guidance for helping the PIC steer UA in self-separation, three core concerns must be considered in advance: when to maneuver, how to maneuver, and the length of time that maneuvers should last. These concerns are all related to maneuvering timing, turning direction, turn rate, and duration. A number of guidance methods have been reviewed and summarized for solving such questions in [114, 115]. For instance, a predefined guidance method is designed based on predefined rules to determine escape trajectories. This is efficient in specific encounters, but in most cases, it is less effective and less optimal than an optimized guidance method [116, 117]. As for the system response time, the predefined guidance method can provide an avoidance maneuvering solution immediately [115]. The optimized guidance method, on the other hand, usually requires extra computation time to search for the best solutions from all possible maneuvering options in mid-air encounters [118–121]. To overcome these drawbacks for real-time decision making, the TCAS selects the least-aggressive vertical maneuver within a limited set of potential climb or descent maneuvers that can provide adequate separation between aircraft in mid-air encounters [114, 122]. However, it cannot be directly adopted for DAA guidance systems because horizontal maneuvers have many more maneuvering options (e.g., various turn rates and heading changes) than vertical maneuvers.

¹Note that the TCAS has been designed to avoid potential mid-air collisions by vertical maneuvers. In case of miscommunication with existing TCAS-equipped aircraft, new DAA systems that are capable of horizontal maneuvers must expect to adapt themselves when necessary [2].

In this chapter, a novel learning-based decision tree method is proposed and designed to provide real-time DAA guidance without demanding extra computation time in searching for the best solutions from all possible maneuvering options. This method is inspired by a Google artificial intelligence (AI) program, AlphaGo, which has recently mastered the complex ancient Chinese board game, “Go”, defeating the best human “Go” game players in the last two years [123,124]. AlphaGo is not directly programmed to play “Go” games; instead, it is designed to learn how to play the game by a general purpose algorithm through analyzing millions of human expert-played “Go” games (supervised learning) and AlphaGo self-played “Go” games (reinforcement learning) [123]. By training through supervised learning and reinforcement learning, two knowledge-based statistical networks: the policy network (how to play the game in the next run) and the value network (how to evaluate the probability of winning the game with the current decision), are thus constructed to reduce the breadth and the depth of the MC searching tree to locate the best solutions in “Go” games [124].

It is true that AlphaGo is designed based on the optimization method and requires extra computation power over thousands of computers to play games. However, more importantly, its design strategy (two knowledge-based statistical networks: the policy network and the value network) as well as the strategy used by TCAS (a limited set of potential maneuvers) can be adopted in this paper to establish the learning-based decision tree method to provide real-time supervisory DAA guidance for small UAS.

6.2 Mitigation Strategy

In accordance with layered zones (i.e., the alert zone and hazard zone) defined for hazard identification in Chapter 4, DAA mitigation strategies are designed and developed in two categories for UA to avoid LoWCs or NMACs in mid-air encounters.

- **Self-separation** refers to the least disruptive horizontal maneuvers (i.e., the least impact on the planned flight mission) triggered by the PIC to avoid LoWCs or NMACs when traffic aircraft are penetrating the alert zone of UA.
- **Collision avoidance** refers to three-dimensional emergency evasive maneuvers triggered by DAA systems to avoid NMACs when traffic aircraft are approaching the CAAT boundary in the hazard zone of UA and NMACs are projected.

As discussed in Chapter 5, the collision risk level, $P_{risk}(Collision)$, is assessed into a normalized ratio in $[0, 1]$ when traffic aircraft are penetrating the alert zone of UA, i.e., from the least severe at 0 (remaining WC) to the most severe at 1 (NMAC projected in 35 seconds). By default, the self-separation mitigation process is activated when the collision risk level $P_{risk}(Collision) > 0.5$.

6.2.1 Self-separation

In this section, we design and develop a learning-based decision tree method to help the PIC determine appropriate horizontal maneuvers for UA to avoid LoWCs or NMACs in self-separation. As discussed in Section 6.1, for effective or optimal maneuvering, the optimized guidance method is preferred in self-separation; however, this method typically cannot be used to provide real-time DAA guidance for mid-air encounters since it often requires extra computation time to search for the best solutions from all possible maneuvering options (i.e., various maneuvering timings, turning directions, turn rates, and durations). To fix this issue, a learning-based decision tree method is proposed in this subsection to use knowledge learned from previous successful maneuvering decisions studied in mid-air encounters, to help small UAS DAA systems select optimized mitigation solutions in real-time for UAS self-separation.

As learned from the design strategies of TCAS and AlphaGo, we need to reduce the breadth of the decision tree (i.e., decision options at each choice point on the decision tree) for real-time decision making. In response to this request, we first design seven horizontal maneuvering options in various turn rates as shown in Fig. 6.2 and listed in Table 6.1 for UA to handle collision risks from low to high risk levels during mid-air encounters.

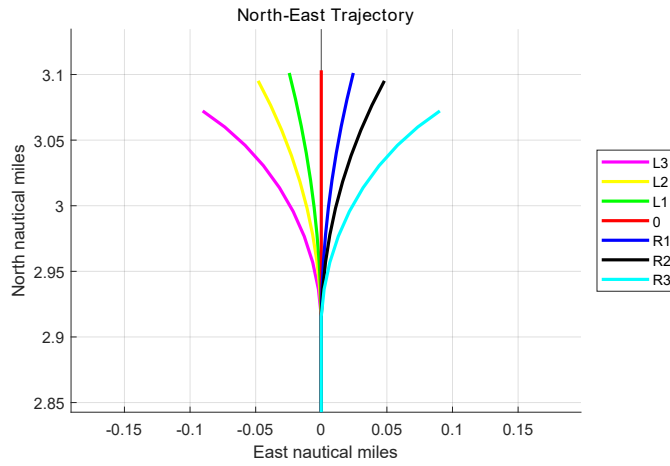


Figure 6.2: Diagram for risk-based horizontal maneuvering options.

Table 6.1: UA horizontal maneuvering options

Suggested heading changes (deg)	Collision risks	Maneuvering options	Heading changes (deg)	Turn rate (deg/sec)	Duration (sec)
$[-180, -60]$	High	$L3$	-60	-6	10
$(-60, -30]$	Medium	$L2$	-30	-3	10
$(-30, 0)$	Low	$L1$	-15	-1.5	10
0	Negligible	$Level$	0	0	10
$(0, 30)$	Low	$R1$	15	1.5	10
$[30, 60)$	Medium	$R2$	30	3	10
$[60, 180]$	High	$R3$	60	6	10

Note: negative for left turn, and positive for right turn; assume that a maximum 6 deg/sec level turn can be performed on the UA during operations.

In this solution, for example, a three-level decision tree can be minimized to only evaluate 7^3 (343) decisions for the self-separation guidance. However, when this solution is applied to deal with uncertainties on sensor measurements (i.e., aircraft headings, velocities, bearings, and wind conditions), it will not be scalable to provide real-time DAA guidance because the size of the decision tree is exponentially expanded with measurement uncertainties. Thus, we have to further improve our new method with the design strategy from AlphaGo; namely, **1)** maneuvering knowledge learned from the previously studied mid-air encounters in MC simulations in Chapter 4 is used to construct **a policy network** to further reduce the breadth of the decision tree for real-time decision making; **2)** the collision risk level, $P_{risk}(Collision)$, assessed and predicted throughout mid-air encounters is used to form **a value network** to reduce the depth of the decision tree and choose the best maneuvering solutions to provide online supervisory guidance for small UA to avoid potential LoWCs or NMACs in self-separation.

6.2.1.1 Maneuvering knowledge learning

Table 6.2: Datasets in the UA maneuvering knowledge base

Dataset	Parameters included
Traffic	Velocity, Detected bearing, Heading
UA	Velocity, Heading
Wind	Wind speed, Wind direction
Maneuvering options	Turning direction, Heading change
Encounter states	Range minimum (WCAT), Range rate, HMD , τ_{mod}

As mentioned in Subsection 4.4.2, MC simulations are carried out to locate WCAT boundaries for UA with traffic in various velocities and wind conditions, and simulation results (based on the DAIDALUS algorithm [101]) are saved in the database as listed in Table 6.2 (including five datasets: traffic states, UA states, wind conditions,

maneuvering options, and encounter states at the time when maneuvers are triggered).

The shortest traffic range (range minimum in encounter states) data are retrieved from the database to determine WCAT boundaries in Chapter 4; in this chapter, the database is treated as a knowledge base for future mid-air encounters. To begin with knowledge learning, we design a supervised learning (SL) method to extract the maneuvering experience from the knowledge base, and then construct the policy network to guide horizontal maneuvers in future mid-air encounters. For example, when the encounter input conditions are determined (e.g., Traffic states: velocity at 100 kt, detected bearing at 30° , and heading to 225° ; UA states: velocity at 75 kt and heading to 0° ; wind conditions: speed at 20 kt and direction to 0°), the suggested maneuvering option (i.e., the turning direction and the heading change) can be obtained from the knowledge base via a database querying operation (e.g., left turn and 36° heading change), and this suggestion is also adopted in the policy network for future similar mid-air encounters. However, in most cases, input conditions cannot be determined in as much detail as this example due to measurement uncertainties. As a result, database range querying operations are employed to retrieve all suggested heading changes from the knowledge base, and then the most probable maneuvering option (i.e., the highest likelihood from all suggested options) is selected for UA to handle measurement uncertainties during mid-air encounters.

For instance, when the detected traffic bearing is at $30^\circ \pm 5^\circ$ and the traffic relative heading is at $225^\circ \pm 5^\circ$, the range querying operation is performed with the detected traffic bearing $\beta_{\text{TRAFFIC}} \in [25^\circ, 35^\circ]$ and the traffic relative heading $\psi_{\text{TRAFFIC}} \in [220^\circ, 230^\circ]$ in the database, and then 81 corresponding database records are obtained and listed in Table 6.3.

Once a list of suggested heading changes is obtained, such as the list in Table 6.3, a likelihood analysis in Table 6.4 is introduced to summarize these suggested

Table 6.3: A sample database range query result from the knowledge base.

No	ID	Range rate (kt)	Heading change (deg)	Range minimum (nmi)
1	477747	-166.56	-36	1.86
2	477748	-166.19	-36	1.85
3	477749	-165.76	-30	1.85
4	477750	-165.29	-30	1.85
5	477751	-164.76	-30	1.84
6	477752	-164.19	-24	1.84
⋮	⋮	⋮	⋮	⋮
76	495030	-163.65	-42	1.83
77	495031	-163.33	-42	1.83
78	495032	-162.96	-36	1.83
79	495033	-162.55	-36	1.82
80	495034	-162.08	-30	1.82
81	495035	-161.56	-30	1.82

heading changes in seven angle regions (i.e., in $[-180^\circ, -60^\circ]$, $(-60^\circ, -30^\circ]$, $(-30^\circ, 0^\circ)$, 0° , $(0^\circ, 30^\circ)$, $[30^\circ, 60^\circ)$, and $[60^\circ, 180^\circ]$) with respect to seven predefined maneuvering options in Table 6.1 (i.e., $L3$, $L2$, $L1$, $Level$, $R1$, $R2$, and $R3$). Finally, the suggested maneuvering option is chosen based on the highest likelihood ratio among seven maneuvering options (e.g., $L2$ suggested in Table 6.4) for UA to avoid LoWCs or NMACs during mid-air encounters.

Table 6.4: Maneuvering options statistics

Suggested heading changes (degree)	Probable maneuvers likelihood	Maneuvering options	Maneuvering index	Most probable maneuvers
$[-180, -60]$	Num_{L3}/Num_{total}	$L3$	-3	(e.g., \checkmark if $\frac{Num_{L2}}{Num_{total}}$ is the highest likelihood ratio.)
$(-60, -30]$	Num_{L2}/Num_{total}	$L2$	-2	
$(-30, 0)$	Num_{L1}/Num_{total}	$L1$	-1	
0	Num_{Level}/Num_{total}	$Level$	0	
$(0, 30)$	Num_{R1}/Num_{total}	$R1$	1	
$[30, 60)$	Num_{R2}/Num_{total}	$R2$	2	
$[60, 180]$	Num_{R3}/Num_{total}	$R3$	3	

In summary, this SL training process can be listed as follows:

1. Select a set of initial conditions for the UA and traffic in a mid-air encounter and

perform a range querying operation in the database with sensor measurement uncertainties, e.g., UA velocity ± 10 kt, traffic velocity ± 20 kt, detected traffic relative bearing $\pm 5^\circ$, traffic relative heading $\pm 5^\circ$, wind speed ± 10 kt, and wind direction $\pm 20^\circ$, to acquire a list of suggested maneuvering options from the knowledge base, as depicted in Table 6.3.

2. Perform the likelihood analysis of suggested maneuvering options on the list; namely, they are counted by heading changes in seven angle regions, e.g., if one of the suggested maneuvering options on the list has a heading change at -36° in $(-60^\circ, -30^\circ]$, then the likelihood counter Num_{L2} is increased by 1 (i.e., $Num_{L2} = Num_{L2} + 1$). Similarly, Num_{L3} , Num_{L1} , Num_{Level} , Num_{R1} , Num_{R2} , and Num_{R3} are counted; and $Num_{total} = Num_{L3} + Num_{L2} + Num_{L1} + Num_{Level} + Num_{R1} + Num_{R2} + Num_{R3}$.
3. The most probable maneuver on the list (with the highest likelihood ratio) is selected as the suggested maneuvering option to construct the policy network for the mid-air encounter defined in Step 1 (e.g., in Table 6.4, $L2$ is selected when $\frac{Num_{L2}}{Num_{total}}$ is the highest likelihood ratio among seven maneuvering options).

To construct the entire policy network in accord with all previously studied mid-air encounters in Chapter 4, we design and carry out an MC tree search (using the above SL training process) throughout the entire knowledge base at a predefined resolution (i.e., every 1° for relative bearings and relative headings from 0° to 360° , every 50 kt for velocities from 50 kt to 300 kt, 20 kt wind in every 45° from 0° to 360°). It is true that the MC tree search requires a large amount of processing time for the millions of range querying operations in the database; however, once the SL training process is completed, the trained policy network can be loaded into the computer memory (RAM) to provide real-time supervisory guidance for the decision making

at each choice point on the decision tree. A sample policy network is visualized for a north heading 75 kt UA in a 2D colormap in Fig. 6.3a, where the vertical axis is traffic headings $[0^\circ, 360^\circ)$; the horizontal axis is traffic-detected bearings $[0^\circ, 360^\circ)$; and maneuvering options are colored as their indexes given in Table 6.4 (i.e., -2 for *L2* left turn in blue, 0 for *Level* no turn in green, 2 for *R2* right turn in red; or, in short, negative indexes for left turns in cool colors and positive indexes for right turns in warm colors). With the traffic detected bearing and heading, this 2D colormap can be used as a lookup table to provide turning guidance. For example, a UA in Fig. 6.3b is operated in north heading (0°) at 75 kt under 20 kt south wind (0°), and a 50 kt traffic is detected at 20° bearing in 300° heading. The policy network in Fig. 6.3a suggests the UA taking a *L3* left turn to avoid a potential LoWC.

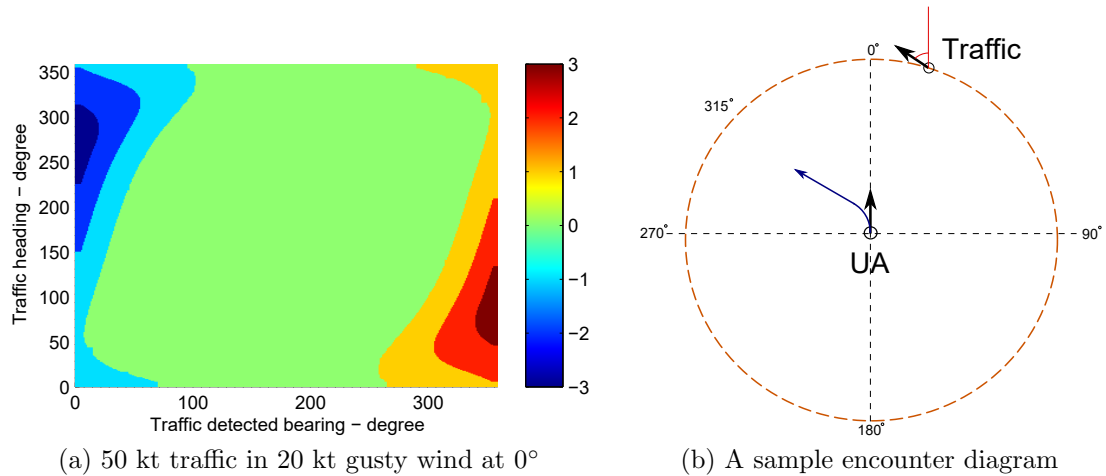


Figure 6.3: Example for using a policy network to provide turning guidance in a mid-air encounter.

More trained policy network diagrams are displayed in Fig. 6.4 for UA maneuvering options in various velocities and wind conditions. Figs. 6.4a, 6.4c, 6.4e, and 6.4g are policy network diagrams for traffic at various velocities in 20 kt gusty south wind (direction at 0°), where most suggested maneuvering options are symmetric. Figs.

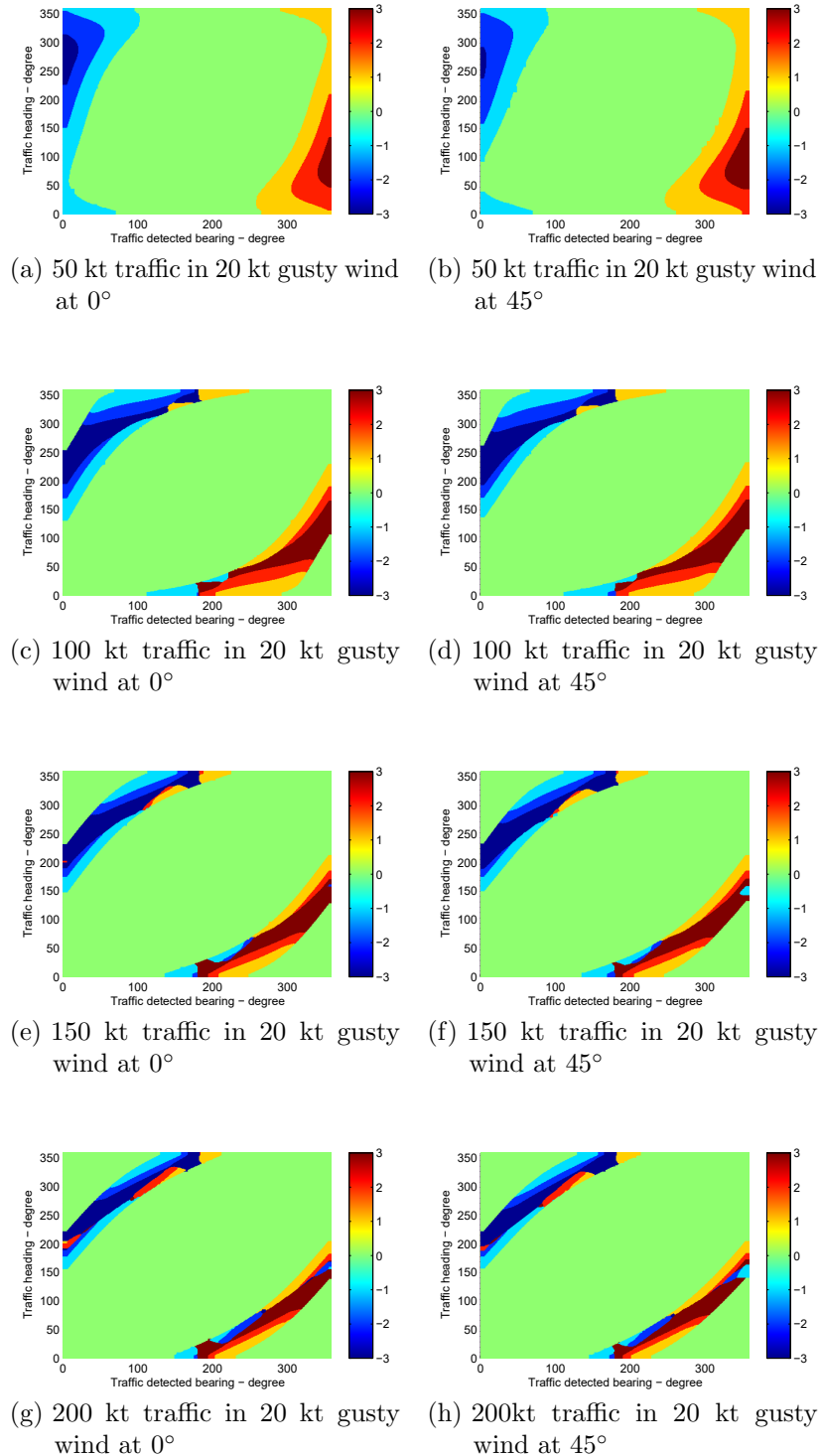


Figure 6.4: Sample policy network diagrams for UA maneuvering options in various velocities and wind conditions (UA: velocity at 75 kt and heading to the north; Legend: negative indexes for left turns in cool colors and positive indexes for right turns in warm colors).

6.4b, 6.4d, 6.4f, and 6.4h are policy network diagrams for traffic at various velocities in 20 kt gusty southwest wind (direction at 45°), where most suggested maneuvering options are not symmetric (with left shifts), in comparison with the ones in 20 kt gusty south wind (direction at 0°).

6.2.1.2 Smart decision tree method

In this subsection, we begin to develop a smart decision tree method (SDTM) to provide real-time DAA guidance for small UA to avoid LoWCs or NMACs in self-separation. In the SDTM, the maneuvering policy network is employed at each choice point (CP) to guide the decision making, reduce the breadth of the decision tree, and save time on the evaluation of decisions. Moreover, metrics designed in Chapter 5 for assessing collision risks in mid-air encounters, e.g., collision risk levels, are used to establish a value network to evaluate mitigation performance of suggested maneuvering options, to reduce the depth of the decision tree, as well as to choose the best maneuvers on the decision tree for real-time supervisory guidance.

As shown in Fig. 6.5, a binary decision tree is constructed based on the trained policy network and the value network, where choice points on the decision tree are set at every time interval (i.e., $\Delta t = 10$ sec) because UA typically need extra time to settle down with state changes in case of a loss of controllability or stabilizability. At each choice point, the UA has two options: either taking a maneuver suggested by the policy network (1), or remaining on/returning to the level flight (0). In addition, the decision tree is constructed in three to six hierarchies upon mitigation performance evaluation results from the value network, which is in accord with the self-separation alerting time from the risk assessment module by the default entry condition when $P_{risk}(Collision) > 0.5$ (i.e., 30 to 60 seconds before LoWCs or NMACs).

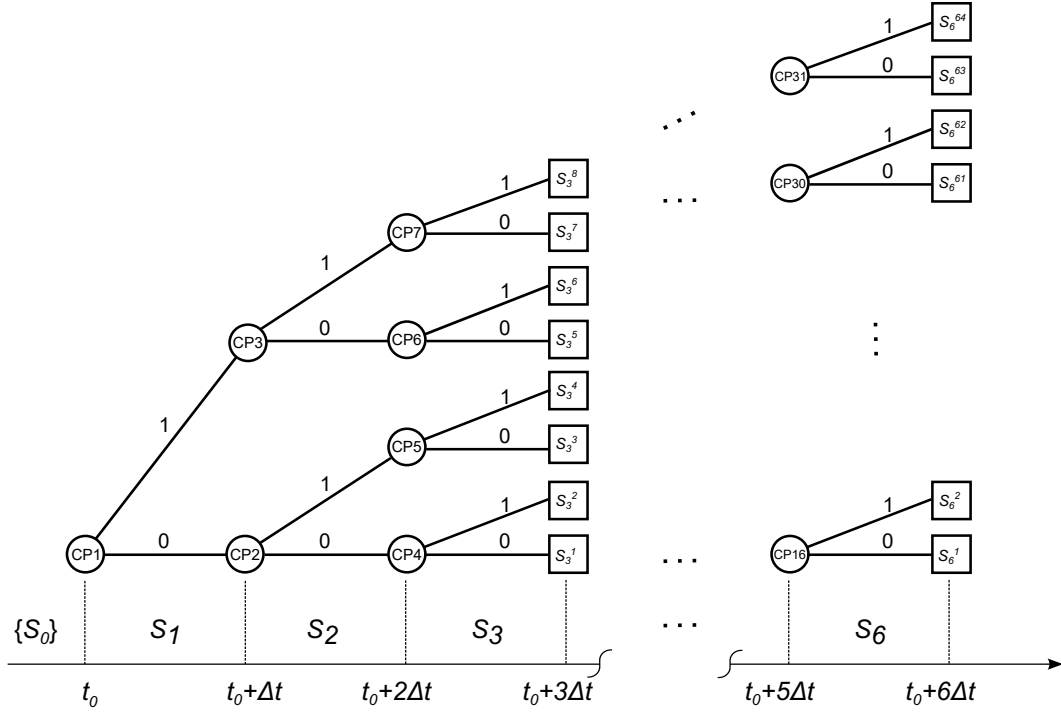


Figure 6.5: An execution of a decision tree with choice points at time interval Δt .

The learning-based SDTM is designed as follows:

System Inputs

Traffic states $X_{\text{TRAFFIC}_n} = [x_{\text{TRAFFIC}_n}, y_{\text{TRAFFIC}_n}, h_{\text{TRAFFIC}_n}, v_{\text{TRAFFIC}_x, n}, v_{\text{TRAFFIC}_y, n}, v_{\text{TRAFFIC}_h, n}]^T$,

UA states $X_{\text{UA}_n} = [x_{\text{UA}_n}, y_{\text{UA}_n}, h_{\text{UA}_n}, v_{\text{UA}_x, n}, v_{\text{UA}_y, n}, v_{\text{UA}_h, n}]^T$,

UA horizontal airspeed $v_{\text{UA}, \text{AS}_n}$,

estimated wind speed v_{WS_n} , estimated wind direction ψ_{WIND_n} ,

detected traffic bearing with respect to the UA β_{TRAFFIC_n} ,

horizontal range r_n , vertical separation V_{s_n} , τ_{mod_n} , $HMD_{\text{predicted}_n}$, $VMD_{\text{predicted}_n}$,

and collision risk level $P_{\text{risk}}(\text{Collision})_n$ at the time step n .

Control Variables

Generally, maneuvering states are $\mathbf{m} = [\dot{v}, \dot{h}, \dot{\psi}, t_m]$ for horizontal acceleration, vertical rate, turn rate, and time duration for maneuvering, respectively. In self-separation, horizontal maneuvers are selected, so maneuvering states can be simplified as $\mathbf{m} = [\dot{\psi}, t_m]$ with allowed horizontal maneuvering options listed in Table 6.1.

Specifications

In the construction of the smart decision tree, the first specification is to provide consistent maneuvers for DAA guidance in self-separation. For example, a left turn $L1$ maneuver is initiated at the first choice point, and then no right turn maneuvers will be selected at other choice points on the decision tree. The allowed maneuvering options are limited to left turns $L1$, $L2$, $L3$, and the level flight $Level$.

The second specification is to determine emergency shutdown conditions for self-separation mitigation. When traffic aircraft are approaching the CAAT boundary in the hazard zone and NMACs are projected, UA should exit from self-separation mitigation and enter collision avoidance mitigation to avoid coming NMACs.

Decision Tree Constructions

When self-separation mitigation is enabled, decision trees are constructed to predict encounter states from the present to the lookahead horizon (e.g., $3\Delta t = 30$ sec) during mid-air encounters [125]. As shown in Fig. 6.5, the policy network is used to determine maneuvering options at choice points on the decision tree; however, if the suggested maneuvering option is not consistent with the ones made at other choice points previously, an $L1$ or $R1$ maneuver will be selected to construct the decision tree upon maneuvering options selected at other choice points.

During the decision evaluation, predicted trajectories of both the UA and traffic for all suggested maneuvering options on the decision tree are generated according to trajectory generation equations in Eq. 4.5 - Eq. 4.13 under given wind conditions. Moreover, decision trees are constructed dynamically (i.e., in various hierarchies) upon evaluation results by the value network. Thus, decision trees are first constructed at three hierarchies with eight suggested maneuvering options, and later they are expanded up to six hierarchies with 64 suggested maneuvering options when $P_{risk}(Collision)_{Predicted} < 0.5$ has not been achieved on three-level decision trees.

System Outputs

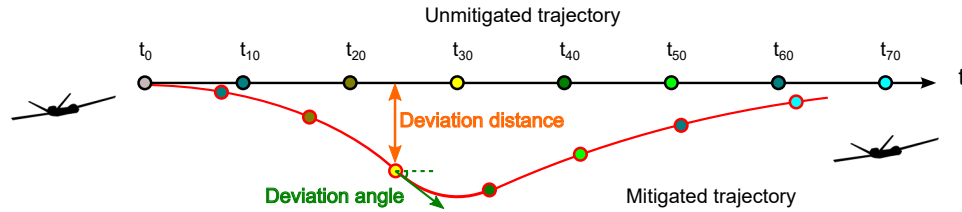


Figure 6.6: Trajectory deviation diagram (modified from [2]).

The learning-based decision tree method outputs the predicted collision risk level $P_{risk}(Collision)_{Predicted}$ and the predicted deviation (i.e., deviation distance and deviation angle) from the original flight course at the lookahead horizon (e.g., 30-second prediction in Fig. 6.6). In Table 6.5, sample analysis results of a three-level decision tree are listed for a head-on encounter in Fig. 6.7. To choose the best maneuvering options in Table 6.5 for UA to avoid potential LoWCs or NMACs, the DAA supervisory guidance should meet with the following conditions:

1. The predicted collision risk level $P_{risk}(Collision)_{predicted} < P_{risk}(Threshold)$ (0.5, the default collision risk level threshold).

2. The predicted $HMD_{predicted} > DMOD_{wc}$ (0.66 nmi).
3. The predicted horizontal range $r_{predicted} > DMOD_{Az}$ (2 nmi).

Thus, without considering system delays, four maneuvering options: 4, 6, 7, and 8 in Table 6.5 (i.e., $[0, L2, L1]$, $[L2, 0, L1]$, $[L2, L1, 0]$, and $[L2, L1, L1]$) can be selected for UA to avoid LoWC in the head-on encounter in Fig. 6.7.

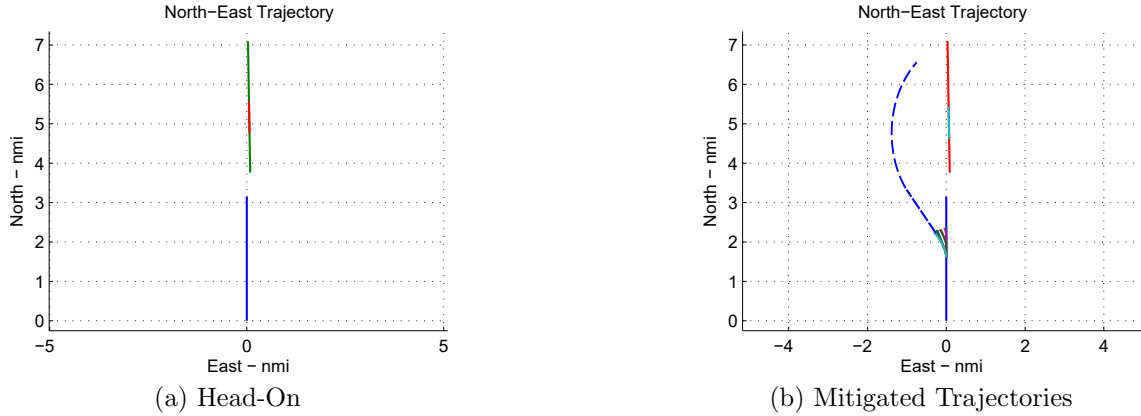


Figure 6.7: Sample mitigation analysis in a head-on encounter.

Table 6.5: List of sample analysis results from eight suggested maneuvering options on a three-level decision tree in a head-on encounter.

Option index	t_0	$t_0 + 10$	$t_0 + 20$	Predicted $P_{risk}(Collision)$ with delays				Deviation distance (nmi)	Deviation angle (deg)	Least disruptive maneuver
				0 sec	5 sec	10 sec	15 sec			
1	0	0	0	0.73	0.76	0.78	0.79	0.00	0.00	
2	0	0	L2	0.59	0.63	0.66	0.69	0.05	21.60	
3	0	L2	0	0.55	0.59	0.62	0.65	0.14	21.60	
4	0	L2	L1	0.43	0.48	0.52	0.56	0.16	32.69	
5	L2	0	0	0.51	0.55	0.58	0.61	0.23	21.60	
6	L2	0	L1	0.39	0.43	0.47	0.52	0.26	32.69	
7	L2	L1	0	0.37	0.41	0.45	0.49	0.29	32.69	✓
8	L2	L1	L1	0.24	0.29	0.35	0.40	0.31	44.10	

Note that the maneuvering option $[0, L2, L1]$ suggests that the PIC should command the UA to maintain level flight in $[t_0, t_0 + 10)$, take an $L2$ turn horizontal maneuver in $[t_0 + 10, t_0 + 20)$, and perform an $L1$ turn horizontal maneuver in $[t_0 + 20, t_0 + 30)$.

Decision Making

1. For suitable DAA guidance in UAS operations, system delays (i.e., delays from sensor measurements, data communications, pilot decisions, command executions and aerodynamic responses) have to be considered in the decision making. Thus, suggested maneuvering options should be able to handle system delays of 5 to 15 seconds [28]; namely, maneuvering options 4 and 6 in Table 6.5 are not suitable maneuvering options when system delays of 10 to 15 seconds are introduced in the prediction.
2. For better mitigation performance, the least disruptive maneuver should be chosen when more than one suitable maneuvering option is available on the decision tree. In this case, maneuvering option 7 (i.e., $[L2, L1, 0]$) in Table 6.5 is selected as the suggested DAA guidance for the PIC, because of less deviation from the original flight course (in both deviation distance and deviation angle) at the lookahead horizon $t_0 + 30$ seconds between maneuvering options 7 and 8 in Table 6.5.
3. For the cases when no maneuvering option can meet $P_{risk}(Collision)_{predicted} < 0.5$ on the six-level decision tree, the maneuvering option with the maximum $HMD_{predicted}$ should be selected as the suggested DAA guidance.

It is noted that the learning-based SDTM is designed to provide the best available DAA supervisory guidance to help the PIC avoid potential LoWCs or NMACs during mid-air encounters in real-time, rather than to determine the best solutions from all possible maneuvering options through MC simulations over a long period of time. Moreover, with the further improvement on the policy network constructed for real-time supervisory guidance, the learning-based SDTM will be able to provide better

maneuvering options that are converging to the optimal maneuvering options for small UA in self-separation.

6.2.2 Collision avoidance

When UA self-separation fails (i.e., when traffic aircraft are approaching the CAAT boundary in the hazard zone and NMACs are projected), the UA should exit from self-separation mitigation and enter collision avoidance mitigation to avoid coming NMACs. To help UA handle such emergencies in collision avoidance, we develop a three-dimensional evasive maneuvering algorithm which consists of two components: horizontal maneuvering strategy and vertical maneuvering strategy.

6.2.2.1 Horizontal maneuvering strategy in the three-dimensional evasive maneuvering algorithm

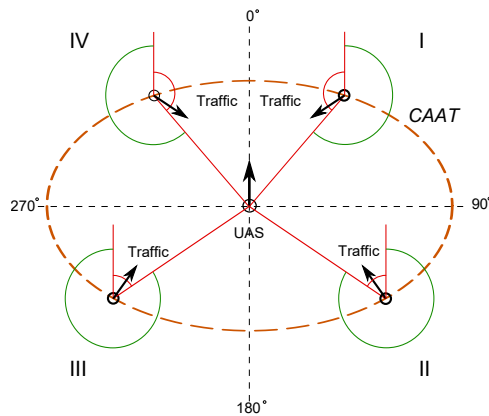


Figure 6.8: Horizontal maneuvering strategies in the three-dimensional evasive maneuvering algorithm.

In Fig. 6.8, once NMACs are projected and the break-ins are predicted on the CAAT boundary in the next five seconds, the evasive maneuvering algorithm evaluates collision risks and triggers horizontal maneuvers based on the traffic-detected relative

bearing and the traffic relative heading with respect to the UA in four quadrants from 0° to 360° . In each quadrant in Fig. 6.8, when traffic are heading to the red regions (displayed as the red arc areas), the algorithm starts to initiate evasive maneuvers to steer the UA to the safe regions which are far away from traffic potential heading areas and stay there until the horizontal range rate $\dot{r} > 0$ and the horizontal range $r > DMOD_{Az}$ (2 nmi) between the UA and traffic. Assume that maximum $2g$ turns (turn rate at $6^\circ/\text{sec}$) can be achieved on the UA. The UA horizontal maneuvering options at four quadrants in Fig. 6.8 are designed differently and their details are described as follows:

Evasive maneuvers in quadrant I

As shown in Fig. 6.9, the maneuvering strategy in quadrant I is to let the UA fly to safe waypoints in quadrant II, which are located at a position 90° off the traffic break-in bearings on the CAAT boundary in quadrant II. Upon the traffic break-in bearings, the UA make left turns or right turns to fly to the predefined safe waypoints. The UA make right turns when the break-in bearing is less than 45° ; and the UA make left turns when the break-in bearing is greater than 45° .

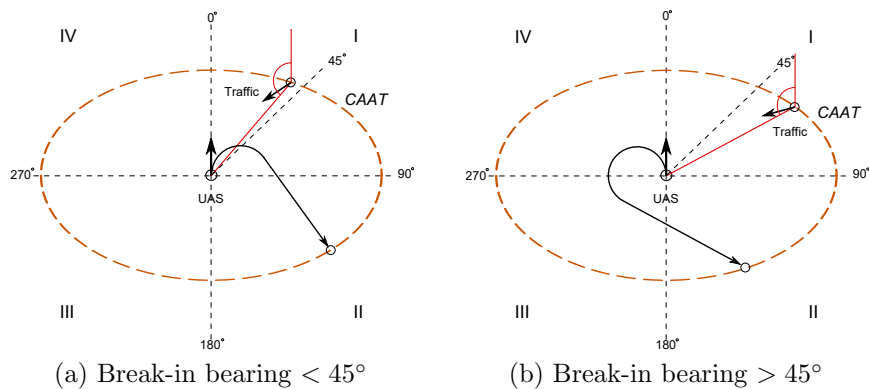


Figure 6.9: Evasive maneuvering strategy in quadrant I.

Evasive maneuvers in quadrant II and III

In Fig. 6.10, two maneuvering strategies are described for the cases when traffic are coming from the rear of the UA. In Fig. 6.10a, the UA make left turns to fly to the predefined safe waypoints in quadrant III when the traffic break-in bearing is in quadrant II (rear right of the UA). In Fig. 6.10b, the UA make right turns to fly to the predefined safe waypoints in quadrant II when the traffic break-in bearing is in quadrant III (rear left of the UA).

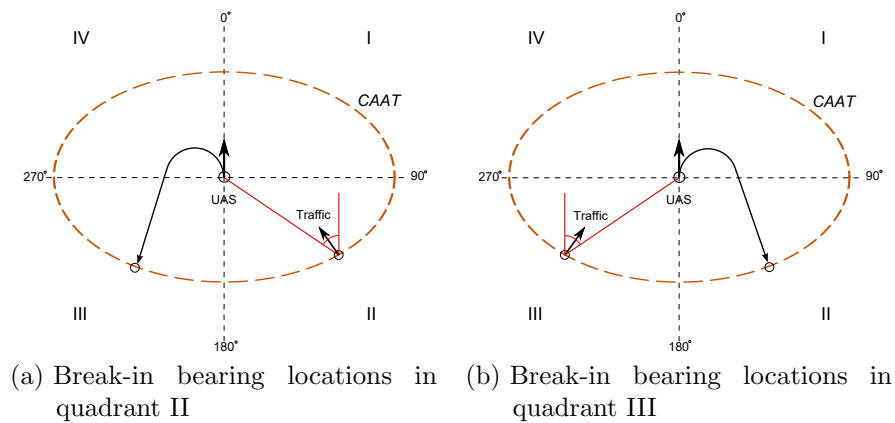


Figure 6.10: Evasive maneuvering strategies in quadrant II and quadrant III

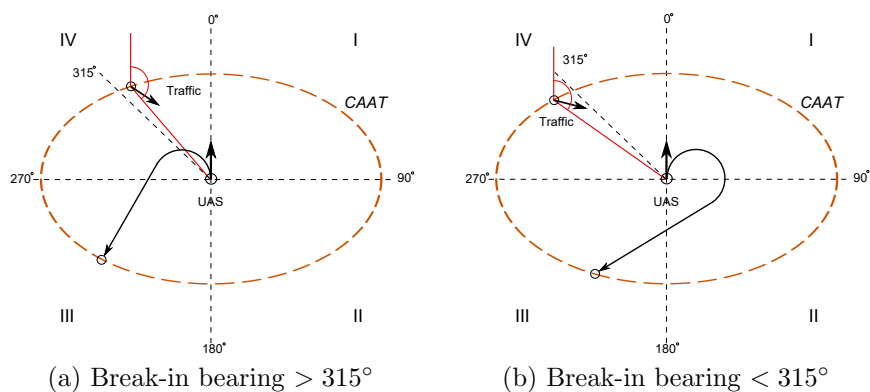


Figure 6.11: Evasive maneuvering strategy in quadrant IV

Evasive maneuvers in quadrant IV.

In Fig. 6.11, the UA make left turns to fly to the predefined safe waypoints in quadrant III when the break-in bearing is greater than 315° ; and the UA make right turns to fly to the predefined safe waypoints in quadrant III when the break-in bearing is less than 315° .

6.2.2.2 Vertical maneuvering strategy in the three-dimensional evasive maneuvering algorithm

In collision avoidance, horizontal and vertical maneuvers are performed at the same time so small UA can escape from emergencies as soon as possible. The vertical maneuvering strategy is designed based on the vertical separation d_h and the traffic vertical rate \dot{h}_{TRAFFIC} ; namely, it is to increase the vertical separation between the UA and traffic, so that the vertical separation at the horizontal CPA can be greater than 100 ft ($h_{\text{NMAC}} = \pm 100$ ft). This strategy is described in further detail with the corresponding diagrams for different encounter geometries in Table 6.6.

Table 6.6: Vertical maneuvering strategy

Geometric Classification	Action	Diagram
Traffic above UA $d_h > 0$	UA descending $\dot{h}_{\text{UA}} < 0$	
Traffic below UA $d_h < 0$	UA climbing $\dot{h}_{\text{UA}} > 0$	
Co-altitude and traffic climbing $d_h = 0$ and $\dot{h}_{\text{TRAFFIC}} > 0$	UA descending $\dot{h}_{\text{UA}} < 0$	
Co-altitude and traffic levelling $d_h = 0$ and $\dot{h}_{\text{TRAFFIC}} = 0$	UA descending $\dot{h}_{\text{UA}} < 0$	
Co-altitude and traffic descending $d_h = 0$ and $\dot{h}_{\text{TRAFFIC}} < 0$	UA climbing $\dot{h}_{\text{UA}} > 0$	

6.3 Performance Evaluation

As drawn in Fig. 6.1, the performance evaluation module is the last module of the Avoid System on the fast-time simulation platform, which is designed to evaluate the mitigation performance of DAA systems through millions of simulated mid-air encounters in civil airspace. With this evaluation module, analytical results are used to guide modifications and improvements for newly-developed mitigation solutions, and later, after a number of evaluation iterations, mitigation solutions can be fine-tuned and qualified on the fast-time simulation platform based on their mitigation performance. Finally, the performance evaluation results should be documented and further analyzed to help system developers work on continuous improvements [126], and to convince aviation authorities to grant approvals for integrating small UA into civil airspace in the near future.

6.3.1 Risk ratio definitions

In statistics, a risk ratio is an intuitive method to use to compare risk probabilities between two selected study groups with relatively low probabilities [127], which is similar to the case of violating encounters in all mid-air encounters. Hence, a risk ratio method is adopted in this subsection to carry out a variety of statistical collision risk analyses over mitigated encounters and unmitigated encounters among millions of simulated mid-air encounters in civil airspace [2, 128].

As drawn in Fig. 6.12, the set and related subsets defined in Table 6.7 are used to describe the risk ratios of mitigated and unmitigated encounters designed in this subsection for statistical mitigation performance analysis. Three risk ratios in equations Eq. 6.1, Eq. 6.2, and Eq. 6.3 are designed: *RiskRatio (mitigated)*, the risk ratio of

mitigated violating encounters is used to evaluate the overall performance of mitigation solutions; *RiskRatio (induced)*, the risk ratio of newly-induced violating encounters is used to locate problems in mitigation solutions and guide future improvements; and *RiskRatio (unresolved)*, the risk ratio of unresolved violating encounters is used to analyze incident reasons, such as late maneuvering timing or wrong maneuvering options.

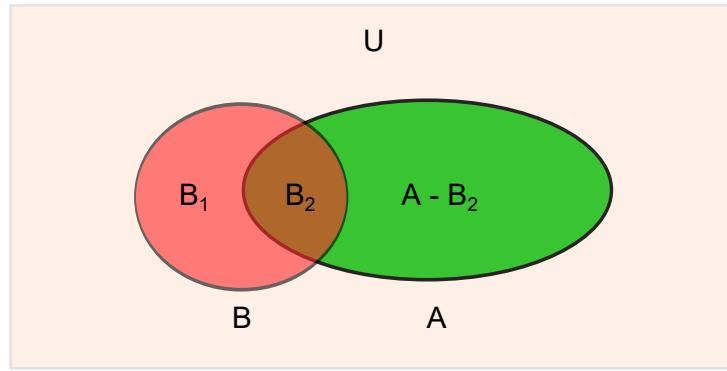


Figure 6.12: Mitigation risk ratio analysis diagram.

Table 6.7: Set and subset for the risk ratio analysis.

Name	Description
Set U	the total number of encounters in the risk ratio analysis,
Subset A	the total number of violating encounters without mitigation,
Subset B	the total number of violating encounters with mitigation,
Subset (A - B ₂)	the number of violating encounters avoided with mitigation,
Subset B ₁	the number of violating encounters newly induced with mitigation, and
Subset B ₂	the number of violating encounters unresolved with mitigation.

$$RiskRatio (mitigated) = \frac{P(\text{ViolatingEnc}_{mitigated})}{P(\text{ViolatingEnc}_{unmitigated})} = \frac{B/U}{A/U} = \frac{B}{A} \quad (6.1)$$

$$RiskRatio (induced) = \frac{P(\text{ViolatingEnc}_{induced})}{P(\text{ViolatingEnc}_{unmitigated})} = \frac{B_1/U}{A/U} = \frac{B_1}{A} \quad (6.2)$$

$$RiskRatio (unresolved) = \frac{P(\text{ViolatingEnc}_{unresolved})}{P(\text{ViolatingEnc}_{unmitigated})} = \frac{B_2/U}{A/U} = \frac{B_2}{A} \quad (6.3)$$

Where:

- $RiskRatio (mitigated)$ the risk ratio of mitigated violating encounters;
- $RiskRatio (induced)$ the risk ratio of newly-induced violating encounters;
- $RiskRatio (unresolved)$ the risk ratio of unresolved encounters;
- $P(\text{ViolatingEnc}_{mitigated})$ the probability of the violating encounters with mitigation;
- $P(\text{ViolatingEnc}_{unmitigated})$ the probability of the violating encounters without mitigation;
- $P(\text{ViolatingEnc}_{induced})$ the probability of the newly-induced violating encounters with mitigation; and
- $P(\text{ViolatingEnc}_{unresolved})$ the probability of the unsolved violating encounters with mitigation.

In Section 6.2, DAA mitigation strategies are introduced in two categories, self-separation and collision avoidance, so the statistical analysis for the performance evaluation is also performed based on these two categories.

6.3.1.1 Self-separation performance

Similar to the equations in Eq. 6.1, Eq. 6.2, and Eq. 6.3, the risk ratios for the mitigation performance analysis in self-separation are defined as follows:

$$RiskRatio_{ss} (mitigated) = \frac{P(\text{LoWC}_{mitigated})}{P(\text{LoWC}_{unmitigated})} = \frac{B/U}{A/U} = \frac{B}{A} \quad (6.4)$$

$$RiskRatio_{ss} (induced) = \frac{P(\text{LoWC}_{induced})}{P(\text{LoWC}_{unmitigated})} = \frac{B_1/U}{A/U} = \frac{B_1}{A} \quad (6.5)$$

$$RiskRatio_{ss} (unresolved) = \frac{P(\text{LoWC}_{unresolved})}{P(\text{LoWC}_{unmitigated})} = \frac{B_2/U}{A/U} = \frac{B_2}{A} \quad (6.6)$$

6.3.1.2 Collision avoidance performance

Similar to the equations in Eq. 6.4, Eq. 6.5, and Eq. 6.6, the risk ratios for the mitigation performance analysis in collision avoidance are defined as follows:

$$RiskRatio_{CA} (mitigated) = \frac{P(NMAC_{mitigated})}{P(NMAC_{unmitigated})} = \frac{B/U}{A/U} = \frac{B}{A} \quad (6.7)$$

$$RiskRatio_{CA} (induced) = \frac{P(NMAC_{induced})}{P(NMAC_{unmitigated})} = \frac{B_1/U}{A/U} = \frac{B_1}{A} \quad (6.8)$$

$$RiskRatio_{CA} (unresolved) = \frac{P(NMAC_{unresolved})}{P(NMAC_{unmitigated})} = \frac{B_2/U}{A/U} = \frac{B_2}{A} \quad (6.9)$$

6.3.2 Performance documentation

As listed in Table 6.8, not only the mitigation results but also the whole processes for risk assessment and mitigation strategy are documented in the database for further statistical analysis and incident investigations to ensure continuous safety assurance [126]. For example, they can be used by system developers to keep improving the performance of DAA systems, and by aviation authorities to grant approvals for integrating small UAS into civil airspace in the near future.

Table 6.8: Datasets documented for further performance analysis

Dataset	Parameters included
Traffic states	Horizontal velocity, Vertical rate, Detected bearing, Heading
UAS states	Horizontal velocity, Vertical rate, Heading
Wind conditions	Wind speed, Wind direction
Maneuvering options	Maneuvering command list, Range at maneuver triggered, Turning direction, Heading change, Vertical rate commanded
Encounter states	Range rate, $HMD(unmitigated)$, $V_s(unmitigated)$, $\tau_{mod}(unmitigated)$, $P_{risk}(Penetration)_{unmitigated}$, $P_{risk}(Range)_{unmitigated}$
Mitigation performance	Trajectory deviation, $HMD(mitigated)$, $V_s(mitigated)$, $\tau_{mod}(mitigated)$, $P_{risk}(Penetration)_{mitigated}$, $P_{risk}(Range)_{mitigated}$, LoWC, NMAC

6.4 Encounter Mitigation Performance Analysis

As shown in the system block diagram in Fig. 6.1, with the completion of the mitigation strategy module and the performance evaluation module in the last two sections, we construct a closed-loop mitigation performance analysis platform (i.e., the fast-time simulation based analysis platform). Through this platform, we begin to carry out a variety of mitigation performance analyses on specified encounter geometries as listed in Table 5.4 (e.g., a left-converging traffic encounter or a left oblique UA overtaking encounter), as well as evaluate the overall mitigation performance for the newly-developed DAA supervisory guidance on the fast-time simulation platform over millions of simulated repeatable mitigated and unmitigated encounters among a comprehensive set of encounter geometries [42]. These performance analyses are summarized in a series of case studies as follows:

Case study 1: mitigation decisions made by a three-level decision tree

Fig. 6.13a shows a pair of horizontal trajectories with a north heading UA and a left-converging traffic in a mid-air encounter, in which the initial conditions are: the detected traffic bearing at 327° (the northwest), the traffic heading at 125° (the southeast), the south wind (10°) at 20 kt, the UA ground speed at 95 kt, and the traffic ground speed at 136 kt. In this encounter, the mitigation enabling condition $P_{risk}(Collision) > 0.5$ is reached at the horizontal range $r = 4.02$ nmi when the predicted $\tau_{mod} = 72$ sec, $HMD = 0.08$ nmi (486 ft) and $V_s = 609$ ft. As listed in Table 6.9, the predicted collision risk levels at $(t_0 + 30)$ keep changing with various system delays considered in the decision making. Hence, to handle non-removable system delays of 5 to 15 seconds, maneuvering option 5 in Table 6.9 (i.e., $[R3, 0, 0]$, which indicates to take a $2g$ right turn at the first choice point for 10 seconds) is

selected as the least disruptive maneuver (according to the deviation distance and the deviation angle) for the UA to remain WC and achieve the new separation at $(t_0 + 30)$ with the horizontal range $r = 2.07$ nmi, $\tau_{mod} = 51$ sec, $HMD = 0.86$ nmi (5225 ft) and $V_s = 609$ ft. Later, as shown in Fig. 6.13b, a simple left turn can be used to return the UA back to the original flight course.

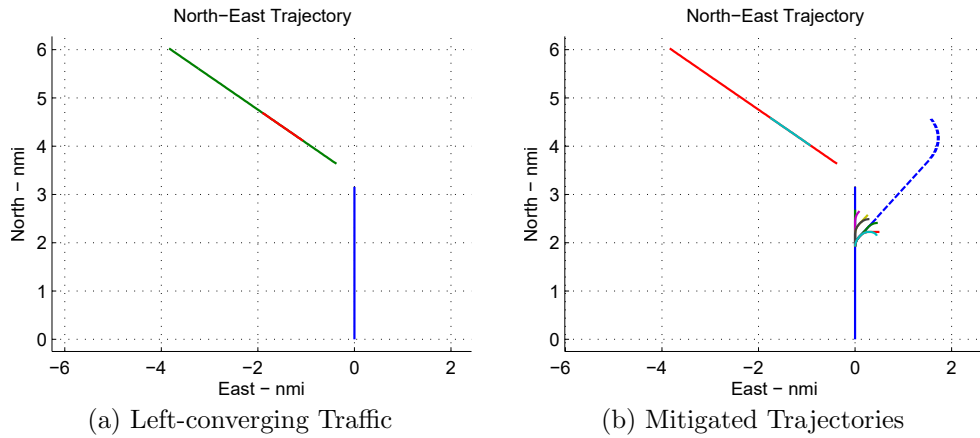


Figure 6.13: Mitigation performance analysis for a left-converging traffic encounter.

Table 6.9: Maneuvering options for the encounter with left-converging traffic by a three-level decision tree.

Option index	t_0	$t_0 + 10$	$t_0 + 20$	Predicted $P_{risk}(Collision)$ with delays				Deviation distance (nmi)	Deviation angle (deg)	Least disruptive maneuver
				0 sec	5 sec	10 sec	15 sec			
1	0	0	0	0.59	0.59	0.59	0.73	0.00	0.00	
2	0	0	R3	0.44	0.48	0.51	0.68	0.09	43.02	
3	0	R3	0	0.39	0.43	0.46	0.56	0.26	43.02	
4	0	R3	R3	0.12	0.21	0.30	0.50	0.30	90.28	
5	R3	0	0	0.22	0.37	0.41	0.45	0.44	43.02	✓
6	R3	0	R3	0.05	0.14	0.22	0.37	0.47	90.28	
7	R3	R3	0	0.00	0.09	0.18	0.27	0.51	90.28	
8	R3	R3	R3	0.00	0.00	0.02	0.23	0.45	149.80	

Case study 2: mitigation decisions made by a six-level decision tree

Fig. 6.14a shows a pair of horizontal trajectories with a north heading UA and a left oblique traffic in a UA overtaking encounter, in which the initial conditions are: the detected traffic bearing at 327° (the northwest), the traffic heading at 61° (the northeast), the south wind (10°) at 20 kt, the UA ground speed at 95 kt, and the traffic ground speed at 76 kt.

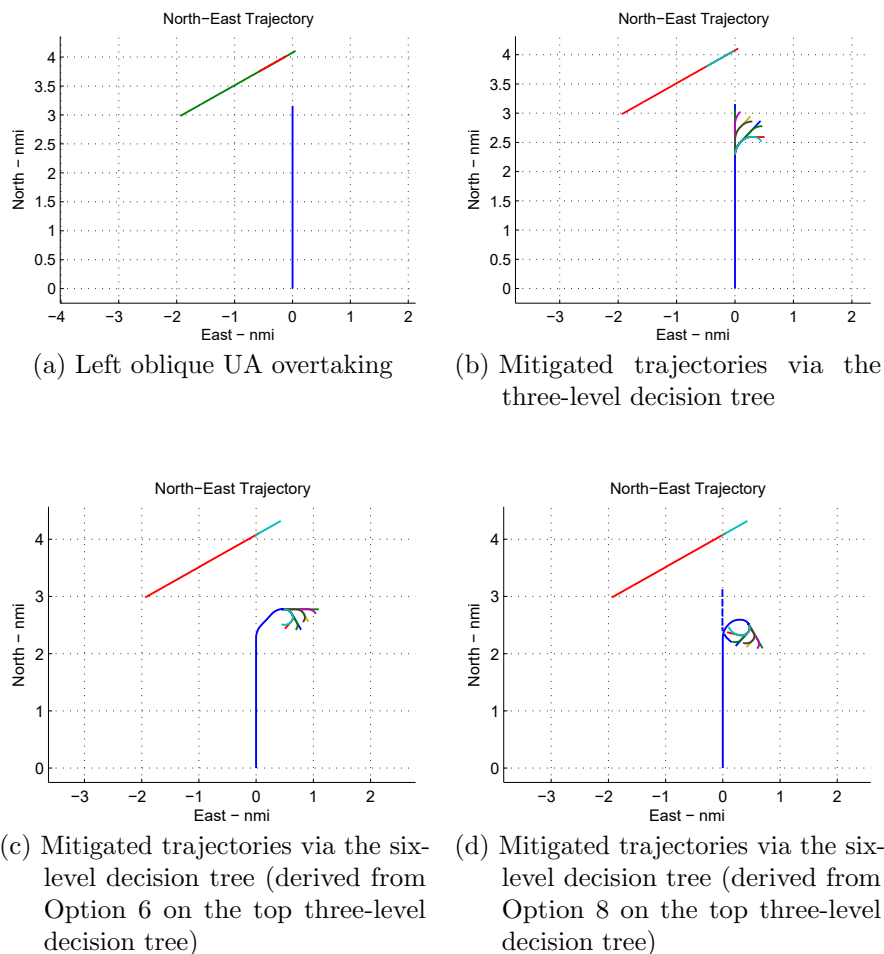


Figure 6.14: Mitigation performance analysis for a left oblique UA overtaking encounter.

In this encounter, the mitigation enabling condition $P_{risk}(Collision) > 0.5$ is reached at the horizontal range $r = 2$ nmi when the predicted $\tau_{mod} = 79$ sec, HMD

= 0.72 nmi (4375 ft) and $V_s = 401$ ft. At the beginning, a three-level decision tree is first constructed for the mitigation process with eight maneuvering options listed in Table 6.10 and their probable maneuvering trajectories drawn in Fig. 6.14b. However, as seen in Table 6.10, the predicted collision risk levels at $(t_0 + 30)$ are all greater than 0.5 on this three-level decision tree, so it requires a further six-level decision tree to make a final maneuvering decision for the UA to remain WC in this encounter (e.g., eight new three-level decision trees are constructed under the eight outputted maneuvering options of the top three-level decision tree).

Table 6.10: Maneuvering options for the left oblique UA overtaking encounter by the top three-level decision tree.

Option index	t_0	$t_0 + 10$	$t_0 + 20$	Predicted $P_{risk}(Collision)$ with delays				Predicted HMD (nmi)	Predicted range (nmi)
				0 sec	5 sec	10 sec	15 sec		
1	0	0	0	1.00	1.00	1.00	1.00	0.70	1.03
2	0	0	R3	0.97	1.00	1.00	1.00	0.18	1.06
3	0	R3	0	0.87	0.96	1.00	1.00	0.36	1.16
4	0	R3	R3	0.82	0.90	0.98	1.00	1.24	1.24
5	R3	0	0	0.77	0.85	0.94	1.00	0.54	1.29
6	R3	0	R3	0.71	0.79	0.88	0.96	1.37	1.37
7	R3	R3	0	0.57	0.65	0.74	0.82	1.55	1.55
8	R3	R3	R3	0.54	0.62	0.70	0.78	1.60	1.60

According to the predictions in Table 6.11 and in consideration of various system delays in decision making, maneuvering option 62 in Table 6.11 (derived from maneuvering option 8 in Table 6.10; namely, [R3, R3, R3, R3, 0, R3]) is selected as the least disruptive maneuvering option from all the qualified maneuvering options (e.g., options 57 - 62) in Table 6.11 with the predicted collision risk levels at $t_0 + 60$. Note that maneuvering option 60 in Table 6.11 is another qualified maneuvering option with the deviation angle at 77.02° but it is not the least disruptive maneuver because of the larger deviation distance ($0.35 > 0.17$ nmi). As with the maneuvering trajectories predicted in Fig. 6.14d, the UA is almost back to the original flight course when maneuvering option 62 is selected.

Table 6.11: Maneuvering options for the left oblique UA overtaking encounter by the expanded six-level decision tree (for Option 6 and 8 on the top three-level decision tree).

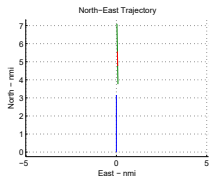
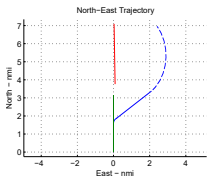
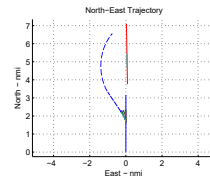
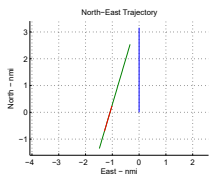
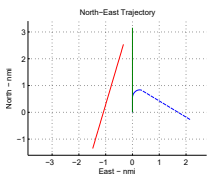
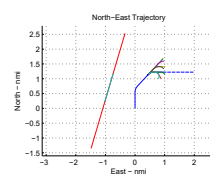
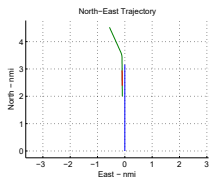
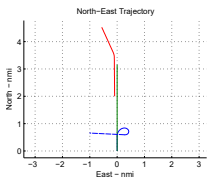
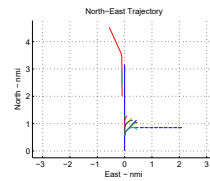
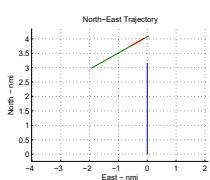
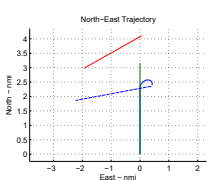
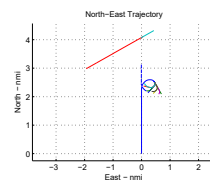
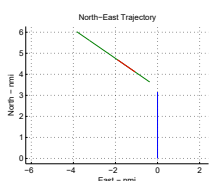
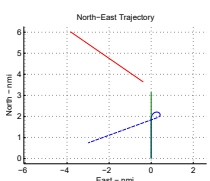
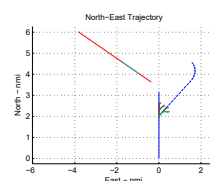
Option index	$t_0 + 30$	$t_0 + 40$	$t_0 + 60$	Predicted $P_{risk}(Collision)$ with delays				Deviation distance (nmi)	Deviation angle (deg)	Least disruptive maneuver
				0 sec	5 sec	10 sec	15 sec			
				\vdots	\vdots	\vdots	\vdots			
41	0	0	0	0.47	0.56	0.64	0.73	1.10	90.28	
42	0	0	R3	0.44	0.53	0.61	0.70	1.04	149.80	
43	0	R3	0	0.38	0.46	0.54	0.63	0.91	149.80	
44	0	R3	R3	0.39	0.47	0.55	0.64	0.82	138.19	
45	R3	0	0	0.31	0.39	0.46	0.55	0.79	149.80	
46	R3	0	R3	0.32	0.39	0.47	0.55	0.69	138.19	
47	R3	R3	0	0.36	0.43	0.50	0.58	0.50	138.19	
48	R3	R3	R3	0.41	0.48	0.55	0.63	0.44	77.02	
\vdots	\vdots	\vdots	\vdots	\vdots	\vdots	\vdots	\vdots	\vdots	\vdots	
57	0	0	0	0.08	0.16	0.23	0.31	0.70	149.80	
58	0	0	R3	0.09	0.16	0.23	0.32	0.60	138.19	
59	0	R3	0	0.12	0.19	0.26	0.34	0.41	138.19	
60	0	R3	R3	0.17	0.24	0.31	0.38	0.35	77.02	
61	R3	0	0	0.15	0.21	0.27	0.35	0.22	138.19	
62	R3	0	R3	0.19	0.26	0.32	0.39	0.17	77.02	✓
63	R3	R3	0	0.32	0.38	0.43	0.51	0.07	77.02	
64	R3	R3	R3	0.37	0.43	0.49	0.56	0.10	77.02	

Case study 3: mitigation decisions made by various mitigation methods

In this case study, for performance comparisons, we carry out a series of mitigation performance analyses over five typical encounter geometries as listed in Table 6.12 using two mitigation algorithms designed in Section 6.2: the mitigation algorithm based on the SDTM in Subsection 6.2.1 and the mitigation algorithm based on the Collision Avoidance Horizontal Maneuvering algorithm (CAHM) in Subsection 6.2.2. Note that the CAHM was originally designed for collision avoidance but it can be used for self-separation as well. In addition, the wind conditions for the encounters listed in Table 6.12 are 20 kt south winds (10°), and the mitigations are enabled with 15-second delays (i.e., 15 seconds after the mitigation enabling condition $P_{risk}(Collision) > 0.5$ is reached during mid-air encounters).

The performance comparisons on the maneuvering options and the trajectory deviations are described and listed in Table 6.12 with the corresponding diagrams.

Table 6.12: Mitigation performance comparison diagrams

No	Unmitigated Geometries	CAHM Mitigated	SDTM Mitigated
1	 <p>Head-On</p>	 <p>Right turn [R3, 15 sec] Deviation [68.32°, 0.52 nmi] at $t_0 + 30$</p>	 <p>Left turn [L2, L1, 0] Deviation [32.69°, 0.29 nmi] at $t_0 + 30$</p>
2	 <p>UA Overtaken</p>	 <p>Right turn [R3, 23 sec] Deviation [114.65°, 0.47 nmi] at $t_0 + 30$</p>	 <p>Right turn [R3, 0, 0, R3, 0, 0] Deviation [90.28°, 1.06 nmi] at $t_0 + 60$</p>
3	 <p>UA Overtaking</p>	 <p>Right turn [R3, 45 sec] Deviation [83.00°, 0.26 nmi] at $t_0 + 45$</p>	 <p>Right turn [R3, R3, 0] Deviation [90.28°, 0.51 nmi] at $t_0 + 30$</p>
4	 <p>Left Oblique UA Overtaking</p>	 <p>Right turn [R3, 42 sec] Deviation [102.06°, 0.31 nmi] at $t_0 + 42$</p>	 <p>Right turn [R3, R3, , R3, R3, 0, R3] Deviation [77.02°, 0.17 nmi] at $t_0 + 60$</p>
5	 <p>Left-converging Traffic UA Overtaking</p>	 <p>Right turn [R3, 40 sec] Deviation [115.84°, 0.35 nmi] at $t_0 + 40$</p>	 <p>Right turn [R3, 0, 0] Deviation [43.02°, 0.44 nmi] at $t_0 + 30$</p>

Based on the comparisons in Table 6.12, we can conclude as follows:

- The SDTM provides less disruptive and more efficient maneuvers for the UA to remain WC: either a lower turn rate during a similar turning time, or less turning time with a similar turn rate. For instance, in the head-on encounter in Table 6.12, the CAHM initiates a 15-second $2g$ right turn, and the SDTM triggers two consecutive left turns: a 10-second $1g$ left turn followed by another 10-second $0.5g$ left turn; namely, the SDTM provides lower turn rates for the UA to remain WC with smaller deviations from the original flight course (with a smaller deviation angle and deviation distance on the simulated maneuvering trajectories).
- The SDTM also intends to select a maneuvering option to help the UA return back to the original flight course easier, e.g., in the left oblique UA overtaking encounter in Table 6.12, the SDTM provides a maneuvering option with a longer turning time but it guides the UA to almost fly back to the original flight course. After the suggested maneuver is performed for 60 seconds, the traffic is outside of the hazard zone of the UA, so the SDTM can return the UA back to the previous flight immediately.

In addition, as shown in the maneuvering diagrams in Table 6.12, multiple suitable maneuvering options are usually available for the PIC to select during UA self-separation. The PIC can pick up them upon the preference of either the safest option or the most efficient option. Therefore, a diagram table like Table 6.12 can be used as a decision visualization method to guide the PIC to choose appropriate maneuvering decisions in consideration of wind conditions and system delays to avoid LoWCs or NMACs in mid-air encounters.

Case study 4: Risk ratio analysis for mitigation performance evaluation in UA self-separation

In this case study, for obtaining comprehensive risk ratio analytical results, 200 million mid-air encounters in a variety of geometries are generated and analyzed on the fast-time simulation platform, in which the wind conditions are set at 20 kt south winds (10°) and the SDTM is employed to provide mitigation solutions for UA self-separation. In Fig. 6.15, three LoWC risk ratios are calculated based on the risk ratio equations in Eq. 6.4, Eq. 6.5, and Eq. 6.6 defined in Subsection 6.3.1.1 (i.e., $RiskRatio_{ss} (mitigated)$, $RiskRatio_{ss} (induced)$, and $RiskRatio_{ss} (unresolved)$).

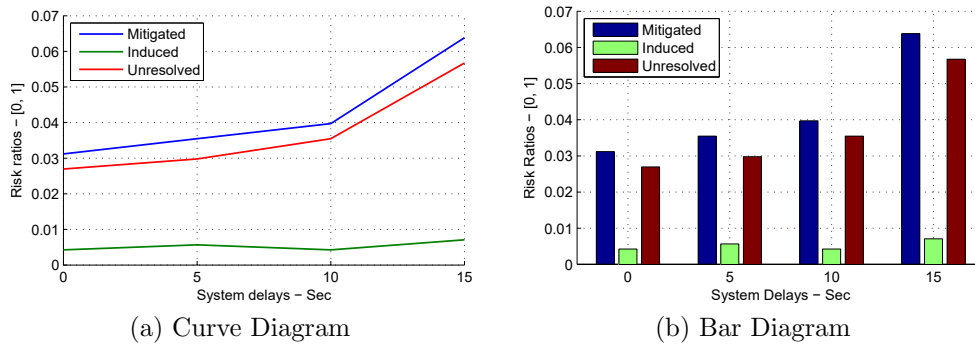


Figure 6.15: Mitigation performance analysis of LoWC risk ratios in UA self-separation.

The impact of LoWC risk ratios on various system delays (e.g., 0, 5, 10, 15 seconds) are also studied in the analytical statistics. For example, in Fig. 6.15, the mitigated LoWC risk ratios stay at [0.03, 0.04] when system delays are within [0, 10] seconds, whereas they are almost doubled when system delays are more than 15 seconds. As the induced LoWC risk ratios are always close to constant in Fig. 6.15, the big increases of mitigated LoWC risk ratios come from the large amount of unresolved LoWCs during mid-air encounters. In other words, the more system delays in the mitigation process the more unresolved LoWCs during mid-air encounters; or, the fewer system delays the better mitigation performance in UA self-separation. As a result, a mitigation

supervisory guidance system like the SDTM becomes essential for the PIC to reduce the decision-making time involving in choosing suitable mitigation solutions to avoid LoWCs or NMACs in UA self-separation.

In addition, as mentioned in Subsection 6.3.2, the newly-induced and unresolved LoWC encounters are also saved in the database for further investigation and analysis to improve the mitigation performance of DAA systems. For example, in the UA overtaken encounter drawn in Fig. 6.16a, the UA and traffic fly to the north at 75 kt and 175 kt, respectively. The self-separation mitigation is triggered when the collision risk level $P_{risk}(Collision)$ is greater than 0.5 (i.e., $r = 2$ nmi, $HMD = 0.11$ nmi, $V_s = 335$ ft, and $\tau_{mod} = 81$ sec). As shown in the projection, the UA will be in LoWC in 46 sec; however, in consideration of system delays, the UA may not be able to fly to the west far enough to prevent LoWC even with a steep left turn (e.g., $HMD_{t_0+46} = 0.62$ nmi, which is still within the minimum LoWC boundary, $DMOD_{wc}$ at 4000 ft or 0.66 nmi).

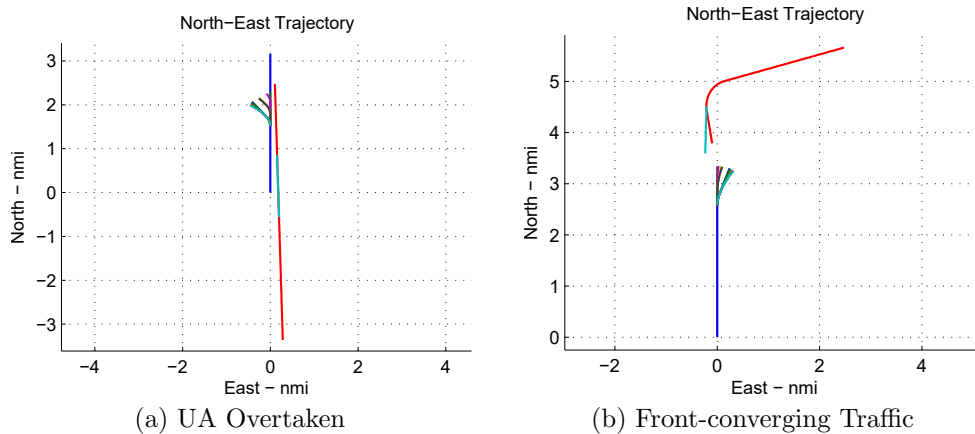


Figure 6.16: Sample diagrams for unresolved LoWC encounters in risk ratio analysis due to system delays.

Fig. 6.16b shows another unresolved LoWC encounter, where the right-converging traffic has a sudden left turn and heads to the UA. In this encounter, the collision risk

level $P_{risk}(Collision)$ is changed from 0 to 0.9 in 20 sec during the traffic's sudden left turn. Meanwhile, HMD is also changed from 2.02 nmi to 0.03 nmi and τ_{mod} is changed from 78 sec to 40 sec. Thus, the UA bounds to LoWC in terms of the late alerting time involving instinctive system delays.

Case study 5: Risk ratio analysis for mitigation performance evaluation in UA collision avoidance

In this case study, for NMAC risk ratio analysis, five million mid-air encounters in a variety of geometries are generated and analyzed on the fast-time simulation platform, in which the wind conditions are set at 20 kt west winds (86°) and the three-dimensional evasive maneuvering algorithm is employed to avoid potential NMACs in UA collision avoidance. In Fig. 6.17, three NMAC risk ratios are calculated based on the risk ratio equations in Eq. 6.7, Eq. 6.8, and Eq. 6.9 defined in Subsection 6.3.1.2 (i.e., $RiskRatio_{ca}(mitigated)$, $RiskRatio_{ca}(induced)$, and $RiskRatio_{ca}(unresolved)$).

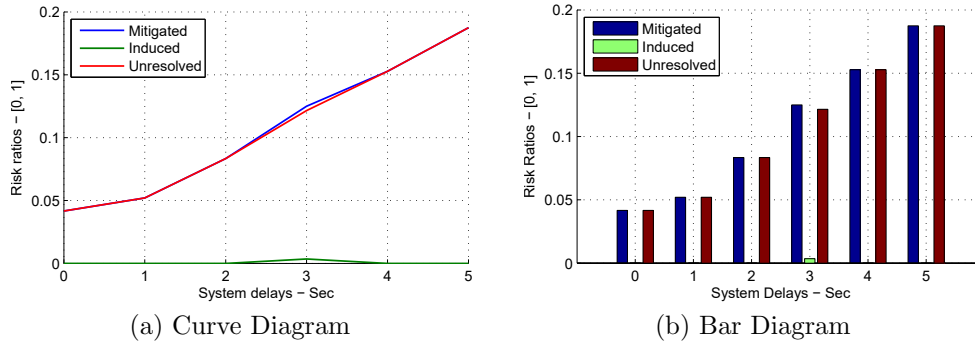


Figure 6.17: Mitigation performance analysis of NMAC risk ratios in UA collision avoidance.

The impact of the NMAC risk ratios on various system delays (e.g., 0, 1, 2, 3, 4, 5 seconds) at the breach of the CAAT boundary are studied in the analytical statistics. As shown in Fig. 6.17, the mitigated NMAC risk ratios are almost in proportion to the system delays introduced in UA collision avoidance. For example,

with five-second system delays, the mitigated NMAC risk ratios are increased to almost 0.2; thus, only 80% potential NMACs can be avoided in UA collision avoidance. In other words, mitigation performance in UA collision avoidance cannot be maintained with system delays. Therefore, as designed and suggested in Subsection 6.2.2, the collision avoidance mitigation should be automatically triggered five seconds before the breach of the CAAT boundary of UA to overcome non-removable system delays from sensor measurements, data communications and aircraft aerodynamic responses.

For further investigation and analysis, all newly-induced and unresolved NMAC encounters are saved in the database. For example, in the UA overtaken encounter drawn in Fig. 6.18a, the UA (green) and traffic (red) fly to the north at 75 kt and 80 kt, respectively. The collision avoidance mitigation is triggered when the traffic approaches to 800 ft behind the UA. A NMAC will occur when the system delay is introduced for more than five seconds (because the UA cannot fly to the east far enough).

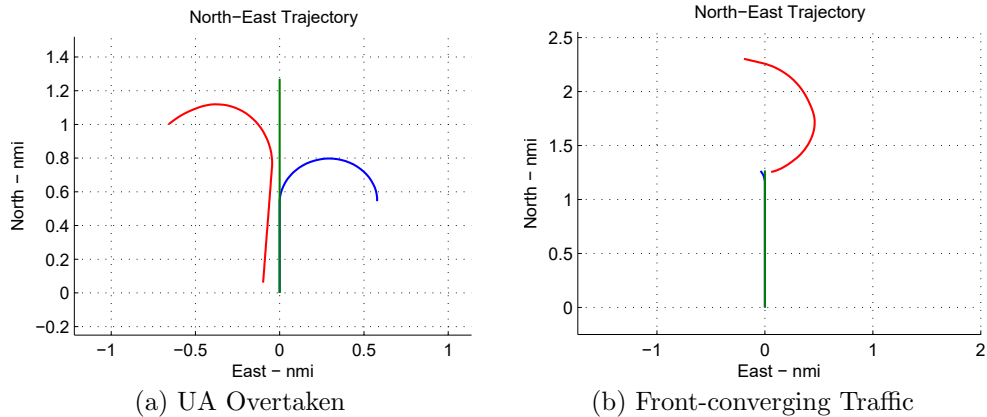


Figure 6.18: Sample diagrams for unresolved NMAC encounters in risk ratio analysis due to system delays.

Fig. 6.16b shows another unresolved NMAC encounter, where the traffic has a sudden right turn and heads to the UA. In this encounter, the traffic is outside the

CAAT boundary in most of the time of the encounter; however, when the traffic engages a sudden turning maneuver, heads to the UA, and almost approaches the CAAT boundary of the UA, in consideration of system delays, there will be not enough alert time for the UA to prevent NMAC from such maneuvering traffic.

6.5 Summary

In this chapter, we complete the development of the mitigation strategy module and the performance evaluation module for the fast-time simulation platform. Two mitigation solutions are developed in the mitigation strategy module for small UA to avoid LoWCs or NMACs in self-separation and collision avoidance. A learning-based decision tree method is developed to help the PIC carry out the decision making on choosing mitigation solutions for UA self-separation, and a three-dimensional evasive maneuvering algorithm is developed to help UA escape from emergencies in UA collision avoidance. Finally, three risk ratios are introduced in the performance evaluation module to help system developers evaluate the mitigation performance, locate the hidden limitations in mitigation algorithms, and work on continuous improvements on DAA systems for the future approval of integrating small UAS into civil airspace.

Millions of simulated mid-air encounters are generated and analyzed on the fast-time simulation based analysis platform to evaluate and qualify the mitigation performance of the DAA supervisory guidance developed for small UA in self-separation and collision avoidance. At the same time, all the mitigation solutions obtained during the performance evaluation and qualification on the fast-time simulation platform are logged into the database for future further analysis and investigation.

Chapter 7

Experimental Work

With the development of DAA systems for small UAS in the RAVEN project, a variety of flight tests have been planned, scheduled, and performed at the RAVEN test site in Argentia, NL. During the flight tests, the theoretical approaches are tested and validated; at the same time, the testing results and difficulties in the flight tests also guide the direction of the theoretical approach in the next run, which is exactly the case for the research work conducted and achieved in Chapter 4-6.



Figure 7.1: UAS operation crew members and the GCS.

As the RAVEN project pictures show in Fig. 7.1, flight tests are team effort missions which require UA, GCS, and ground control crew members, e.g., external pilots (EPs), aerial vehicle operators (AVOs), ground supervisors, and ground spotters,

as well as a test site to carry out UA testing flights with the permission from Transport Canada under the SFOC.

7.1 RAVEN Unmanned Aircraft

7.1.1 Giant Big Stik Unmanned Aircraft

The Giant Big Stik (GBS) aircraft is originally an Almost-Ready-Fly (AFR) R/C fixed wing model aircraft from Great Planes. The engine and servos were selected and installed by the RAVEN project, and the detailed specifications are listed in Table 7.1. For UAS integration, the ArduPilot Mega (APM) 2.6 autopilot from 3D Robotics is used as the flight controller for the GBS UA. This APM autopilot is designed to use an external magnetometer to improve flight performance by allowing the compass module (or combined GPS with the compass) to be placed further away from sources of potential magnetic interference [129]. The GCS obtains the telemetry data and sends commands to the UA over the command and control link at 900 MHz. The EP uses a hand-held controller at 2.4 GHz for the manual override.

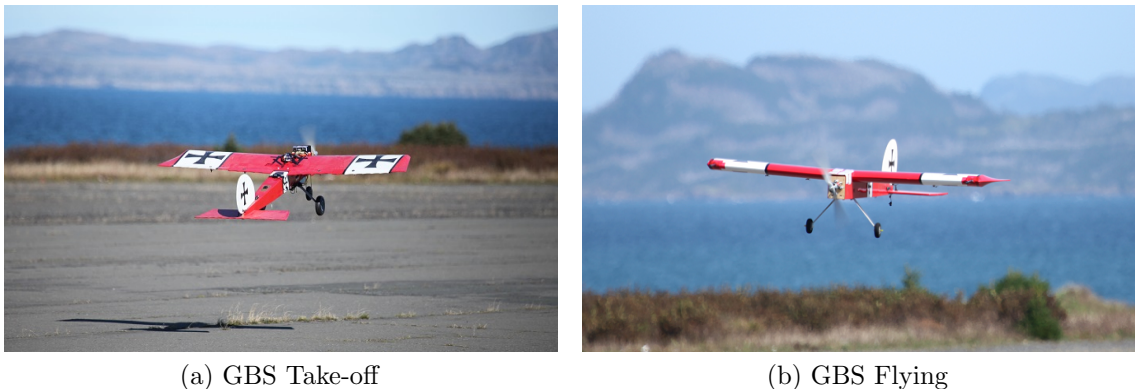


Figure 7.2: Giant Big Stik aircraft take-off and flying.

The GBS UA is an aerobatic aircraft flying at a wide airspeed range in [30, 100]

kt. With a RAVEN custom-made 2-liter fuel tank, this UA can be airborne at a 50 kt cruise speed for one hour without refuelling.

Table 7.1: Giant Big Stik aircraft specifications.

Aircraft	Parameters	Specifications
Airframe	Wingspan	2045 mm
	Wing area	97.93 dm ²
	Length	1385 mm
	Empty weight	7 kg
	Maximum take-off weight	10 kg
Engine	Model	DLE-30
	Displacement	30.5 cc
	Performance	3.7 hp at 8500 rpm
	Fuel	87-93 Octane Gasoline with a 30:1 gas/2-stroke (2-cycle) oil mixture
Propellers	Ignition	Electronic 6V
	Model	XOAR Wood PJA Natural
	Size	18x8, 18x10, 19x8, 20x8

7.1.2 Vector-P Unmanned Aircraft

The Vector-P aircraft is a professional composite UA with an endurance from 30 minutes to six hours depending on the payload and fuel configurations on the UA [130]. The detailed specifications are listed in Table 7.2. For UAS integration, the MicroPilot 2128g autopilot is used as the flight controller for the Vector-P UA. This autopilot is designed to support long-range communication (LRC) between the UA and GCS [131]. The GCS obtains the telemetry data and sends commands to the UA over the command and control link at 900 MHz. The EP uses a hand-held controller at 2.4 GHz for the manual override.

The Vector-P UA is a pusher propeller aircraft which reduces the aerodynamic disturbance at the front of the aircraft [132] and provides a relatively large payload bay in the fuselage for various payload configurations. With a RAVEN custom-made 5-liter fuel tank, this UA can be airborne at a 75 kt cruise speed for one hour without



(a) Vector-P Take-off



(b) Vector-P Flying

Figure 7.3: Vector-P aircraft take-off and flying.

refuelling.

Table 7.2: Vector-P aircraft specifications.

Aircraft	Parameters	Specifications
Airframe	Wingspan	2565 mm
	Length	2300 mm
	Empty weight	15 kg
	Maximum take-off weight	25 kg
Engine	Model	3W-75iUS
	Displacement	75.22 cc
	Performance	7.5 hp at 8500 rpm
	Fuel	87-93 Octane Gasoline with a 50:1 gas/2-stroke (2-cycle) oil mixture
	Ignition	Electronic 6-8.5V
Propellers	Model	Biela Carbon Props
	Size	22x12, 24x10

7.2 RAVEN Flight Test Site

Due to safety concerns, the flight tests are carried out under the SFOC at the RAVEN flight test site, an abandoned former US naval base in Argentia, NL. As shown in Fig. 7.4, there is a large amount of flat open space on the runway areas for short range visual-line-of-sight (VLOS) flight tests, as well as adjacent areas above the ocean for long-range beyond-visual-line-of-sight (BVLOS) flight tests.

It usually takes about one and a half hours on the highway from the RAVEN project office in St. John's, NL to the test site in Argentia, NL. A three thousand square-foot hangar space is also rented by the RAVEN project at the Argentia test site for the storage and local workshop to prepare flight missions and repair aircraft parts during the flight tests.

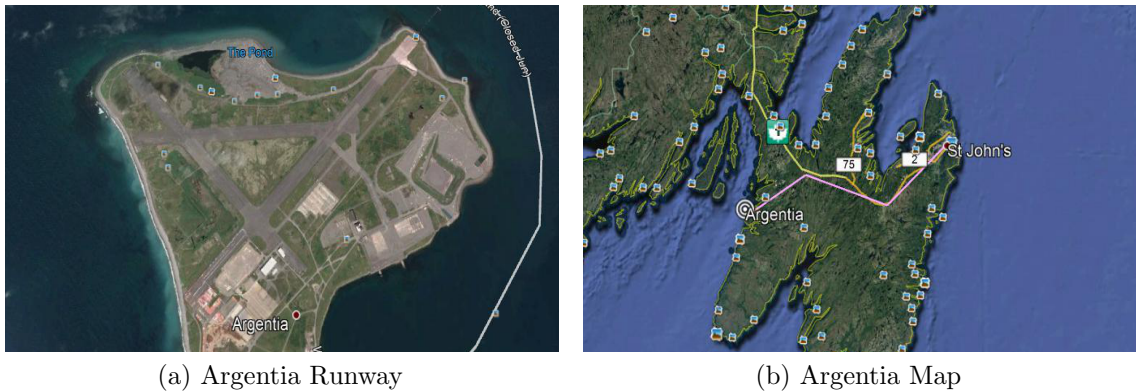


Figure 7.4: The RAVEN project test site in Argentia, NL.

7.3 UA Synchronization for Mid-air Encounters

Achieving repeatable pre-defined air-to-air encounter flights is an essential task to collect data for the development of DAA systems at the beginning of the research, as well as to test and validate newly developed DAA systems later on for the completion of the research work. To obtain the most effective and repeatable mid-air encounters, two UA have to be synchronized to meet together at a predefined location and altitude at the same time; namely, this requirement can be summarized as UA four-dimensional (4D) synchronization during mid-air encounters [37, 38].

At the early stage of the RAVEN project two UA 4D synchronization was attempted by using two EPs and two AVOs on the ground. This effort failed due to too many errors occurring in this manual process. For example, errors occurred when trying to

use the human eye to estimate aircraft position and altitude, the wind effect blowing the aircraft off-track could not be compensated for correctly, and errors occurred due to the time delay experienced during communications between the EP and the AVO. Furthermore, it was very difficult to achieve repeatable air-to-air synchronized encounters using this manual 4D synchronization method. In a twenty-minute flight, data from only one or two encounters were validated for data analysis. Most of the flight time was wasted. To overcome these drawbacks, an automatic encounter trajectory control algorithm is designed and developed to achieve two UA automatic 4D synchronization during mid-air encounters at different encounter angles and in gusty wind conditions.

7.3.1 System Schematic for UA 4D Synchronization

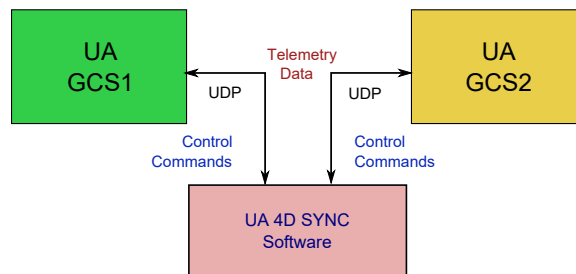


Figure 7.5: UA 4D synchronization system schematic diagram

When two UA are switched to autopilot control after manual take-off, two GCSs are used to monitor the status of the autopilot on the UA and to command the UA to change waypoints, cruise speed, altitude, etc. As shown in Fig. 7.5, the UA 4D synchronization algorithm communicates with the two aircraft GCSs over the UDP network. After analyzing the telemetry data from the two UA, the synchronization algorithm sends out synchronization commands to the two GCSs to control the two UA for synchronized flight.

7.3.2 System Design for UA 4D Synchronization

To synchronize two UA in the air, the UA 4D synchronization algorithm first needs to acquire the current location, airspeed, altitude, heading, and next waypoint of each of the two UA from telemetry data on the UDP network of two GCSs.

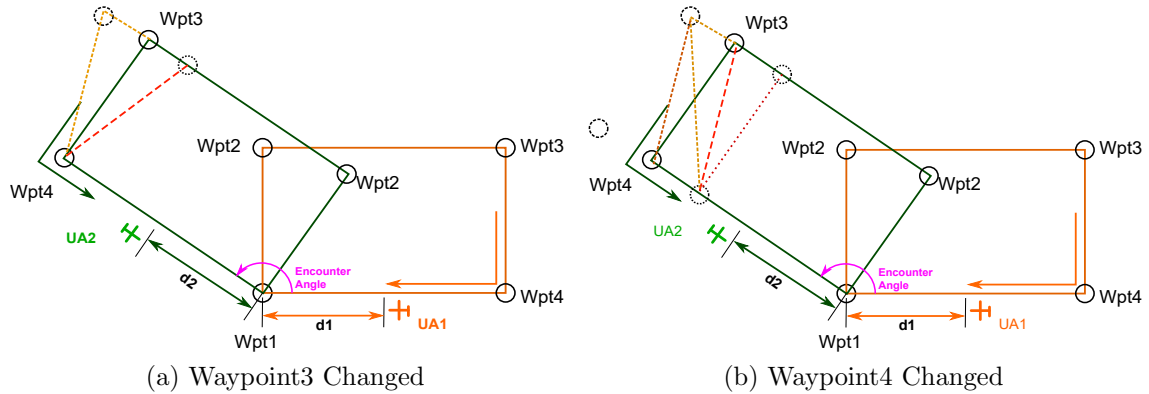


Figure 7.6: UA 4D synchronization system design diagram.

As shown in Fig. 7.6, UA2's rectangular circuit (green color) can be rotated around Waypoint 1 to achieve desired encounter angles from 0 to 360 degrees at Waypoint 1. The main control algorithm is used to minimize the distance error between the two aircraft and their target waypoint ($d1-d2$). Namely, when the two aircraft head to the same waypoint number and the error ($d1-d2$) closes to zero, the two aircraft are 4D synchronized. Indeed, this control variable, i.e., distance error to the target waypoint, also includes the implied wind effects in the control loop automatically so the 4D synchronization algorithm does not need the AVO to manually update the changing wind information during the synchronization.

If a large disturbance occurs, the algorithm not only changes the aircraft airspeed but also automatically changes the location of the target waypoint to make up for the limitation in the UA airspeed range. For example, in Fig. 7.6a, when UA1 reaches its Waypoint 3, and UA2 is still too far away from its Waypoint 3, the algorithm will

automatically shorten UA2's distance to its Waypoint 3 by moving UA2's Waypoint 3 to UA2's current location and command UA2 to head to its Waypoint 4, as UA1 is doing. On the other hand, when UA2 is flying too fast, the new algorithm will move its target Waypoint 3 further away to wait for UA1 to catch up to its Waypoint 3. In Fig. 7.6b, the same control theory is imposed on UA2's Waypoint 4 as well. By changing the locations of UA2's Waypoint 3 and Waypoint 4, the control variable, i.e., the distance error to the target waypoint, will be small enough to be minimized when the two aircraft head to their Waypoint 1 and a synchronized 4D encounter at the location of Waypoint 1 is achieved.

7.3.3 Test Results for UA 4D Synchronization

Robust performance of UAV 4D synchronization has been achieved in flight tests at the RAVEN project test site. As shown in Fig. 7.7a, the UA 4D synchronization software moves UA2's Waypoint 3 closer when UA1 has reached its Waypoint 3 (top corner of the orange rectangular circuit). After the distance error is minimized after Waypoint 3, UA2 is able to catch up to UA1 and have a synchronized 135-degree encounter at Waypoint 1 as shown in Fig. 7.7b.

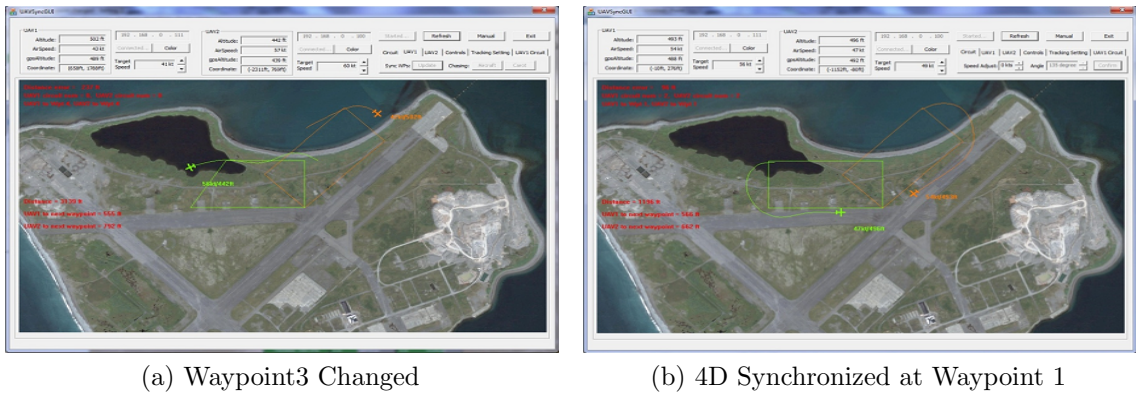


Figure 7.7: UA 4D synchronization testing results.

7.4 Development of ADS-B Based Cooperative ACAS

Since 2011, the RAVEN project has partnered with R-Cubed Engineering for the use of their All-Weather Sense and Avoid System (AWSAS) shown in Fig. 7.8. AWSAS is an ADS-B technology-based system which transmits ADS-B positional information on 978 MHz and receives ADS-B radio transmissions on both 978 MHz ES and 1090 MHz. The AWSAS unit also has an onboard Digital Signal Processor (DSP). During the development of the RAVEN ADS-B based ACAS, the UA collision avoidance algorithm designed in Subsection 6.2.2 is implemented on the AWSAS DSP processor which analyzes the ADS-B traffic information and sends out collision avoidance guidance commands to the autopilot on the host UA in order to initiate evasive avoidance maneuvers whenever the traffic is approaching the CAAT boundary and potential NMACs are predicted [35, 36].



Figure 7.8: AWSAS Box Diagram.

7.4.1 System Design for ACAS

As shown in Fig. 7.9, the host UA and the traffic UA are both equipped with AWSAS boxes so that the air traffic information can be exchanged between two UA via 978 MHz RF communication. AWSAS is connected to the autopilot on the UA via either PWM signals or RS232 serial communications.

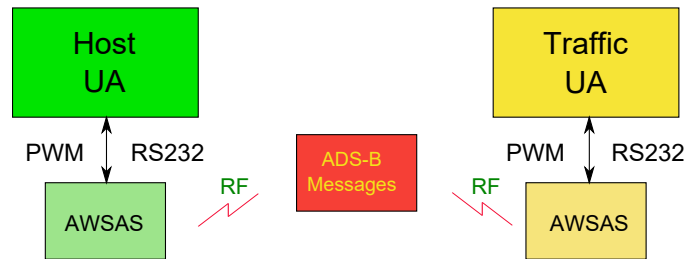


Figure 7.9: Cooperative ADS-B based ACAS schematic diagram.

On the AWSAS DSP processor, the UA collision avoidance algorithm has been implemented in the C language and compiled into the runtime code for real-time DSP running, where the decoded GPS positions are first converted into the local Cartesian coordinates (x, y, h) by Eq. 3.1 - Eq. 3.6 in Chapter 3, and then fed to the UA collision avoidance algorithm for analysis and decision making. Once collision avoidance maneuvers are required and selected during mid-air encounters, the AWSAS DSP processor sends out three control variables to the autopilot on the UA, i.e., the turn rate, the heading change, and the vertical rate, to initiate evasive maneuvers for collision avoidance.

7.4.2 Results for Initial ACAS Flight Tests

After the initial ADS-B based cooperative ACAS prototype is developed and tested on the ground, a series of airborne ACAS flight tests have been scheduled and performed

at the RAVEN test site in Argentinia, NL to check the system performance of both the hardware and the software, i.e., the ADS-B transmitter and receiver, the ADS-B antenna positions on the UA, the communication protocol between the autopilot and AWSAS, as well as the collision avoidance algorithm implemented on the AWSAS DSP processor.

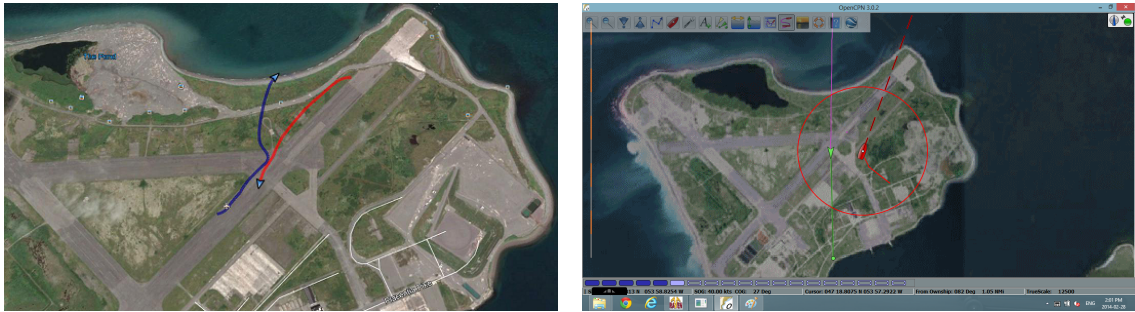
As shown in Fig. 7.10, two GBS UA sit on the runway before the ACAS flight tests, where the AWSAS box is mounted on the upper nose of the GBS UA.



Figure 7.10: Initial flight tests for ACAS.

During the flight tests, two EPs first take off two UA manually and hand over to two AVOs for autopilot flights, then the UA 4D synchronization software developed in Section 7.3 is used to align two UA to enter the pre-defined encounter in a short period of time (e.g., two minutes). Once two UA are aligned, the UA 4D synchronization software releases the flight control to the ACAS for collision avoidance mitigation.

The maneuvering trajectories in Fig. 7.11a demonstrate a successful automatic collision avoidance maneuver triggered by the ACAS on the runway areas in a head-on encounter. Moreover, usually only a set of flight statuses from the UA can be displayed on a computer screen on the GCS, either the host UA or the traffic UA, thus for increasing the encounter situation awareness during flight tests, an ACAS monitoring



(a) Head-on encounter trajectories from the recorded autopilot flight logs (b) ACAS GUI on the GCS for monitoring

Figure 7.11: Initial test results for ACAS.

graphic user interface (GUI) is developed for AVOs as shown in Fig. 7.11b, where the red box is the host UA and the green triangle is the traffic UA. Before the maneuver is engaged, the host UA is heading to the northwest (315°) and the traffic UA is heading to the south (180°). At the time the turn is triggered, the traffic UA detected bearing to the host UA is around 20° ; therefore, the right turn avoidance is triggered and shown in Fig. 7.11b. In addition, Fig. 7.12 shows air-to-air pictures at mid-air encounters during ACAS flight tests, where the traffic UA are detected in red eclipses.



(a) No maneuver required for traffic UA on the top (b) Left turn maneuver triggered for a co-altitude traffic UA in the front

Figure 7.12: Encounter pictures in ACAS flight tests.

7.4.3 Hardware-in-loop ACAS Testing Platform

More than a dozen automatic collision avoidance maneuvers have been successfully achieved on the RAVEN UA at the RAVEN test site during short range Visual Line of Sight (VLOS) flight tests; however, due to the high cost of UA and flight operations, numerous all-direction encounter tests with aircraft in various airspeed ranges cannot be performed as required; therefore, a hardware-in-loop (HIL) ACAS testing platform is designed and constructed for intensive ACAS functional testing in the RAVEN project lab.

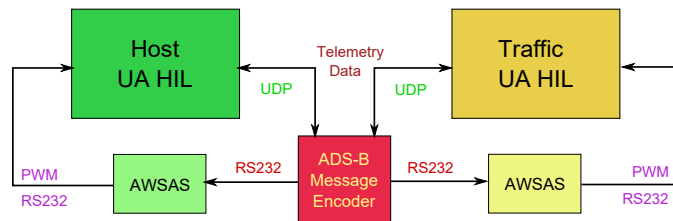


Figure 7.13: The HIL ACAS testing platform schematic diagram.

As shown in Fig. 7.13, real-time aircraft telemetry data from two (i.e., host UA and traffic UA) separate HIL simulators are fed into the ADS-B message encoder and converted into real-time ADS-B messages. AWSAS boxes receive the ADS-B messages from the RS232 serial communication link instead of the 978 MHz RF link. The PWM signals or RS232 data are the outputs from the AWSAS boxes that command the autopilot to control the host UA to make proper maneuvers if needed.

In Fig. 7.14, the two laptops on the left are HIL systems for the host UA and the traffic UA, where the GCS software communicates with the autopilot and the simulated UA in FlightGear [133], a visualized aircraft model and flight environment simulator software. The ADS-B message encoder software is running on the laptop on the right. At the same time, this laptop is also used to display received ADS-B



Figure 7.14: The HIL ACAS testing platform in the lab.

messages on the map where two UA are flying. When used in the HIL simulators as described above, UA in various airspeed ranges can be simulated and flown in all direction encounter geometries aligned by the UA 4D synchronization software as required. The UA collision avoidance algorithm behaves exactly as it would when installed on a UA during real flight tests. This means future actual test flights using this avoidance algorithm should achieve the same results as observed during HIL simulator testing.

7.4.4 ACAS HIL Test Results

Thousands of NMAC encounters in a variety of geometries have been performed on the HIL ACAS testing platform with 90% successful collision avoidance results during ACAS HIL tests. Most unsolved NMACs occur when traffic UA emerge from three pairs of symmetric bearing regions on the UA CAAT boundary as the red arcs marked in Fig. 7.15 (i.e., $30^\circ \pm 10^\circ$ and $60^\circ \pm 10^\circ$ in Quadrant I, $110^\circ \pm 10^\circ$ in Quadrant II, $250^\circ \pm 10^\circ$ in Quadrant III, as well as $330^\circ \pm 10^\circ$ and $300^\circ \pm 10^\circ$ in Quadrant IV).

Upon the UA trajectories depicted in Fig. 7.15, most unresolved NMACs ($d < R_{\text{NMAC}} = 500 \text{ ft}$) are because of the late triggering on the required collision avoidance

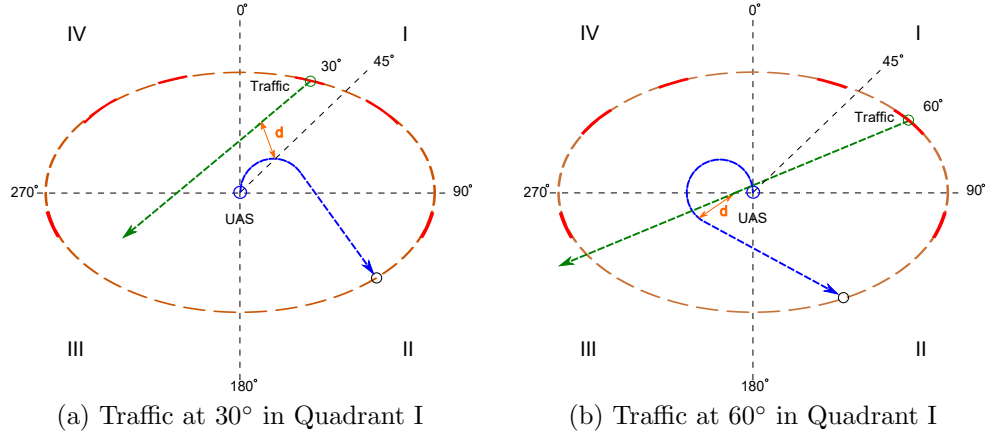


Figure 7.15: Diagrams for unresolved NMACs in Quadrant I in ACAS HIL tests.

maneuvers; in other words, the collision avoidance algorithm fails to estimate wind effects on small UA in collision avoidance. The HIL testing results indeed have guided research work on the CAAT boundary localization in winds for small UA (i.e., the research work to determine the CAAT boundaries in various wind conditions in Chapter 4), as small UA are more affected in winds during horizontal maneuvers than manned aircraft and large UA.

In addition, the HIL flight test is extremely time consuming in terms of the time to set up the UA on the HIL simulator and the time to carry out the pre-defined mid-air encounter. It takes about 20 minutes per encounter on the HIL simulator. As a result, the HIL flight test is good for system development, e.g., the system functional test for the newly-developed DAA systems; however, for system evaluation and qualification, it is better to design a fast-time evaluation and qualification platform to perform millions of simulated encounters in computer processor ticks (e.g., in one ten-millionth of a second [134]), instead of actual clock ticks in seconds on the HIL testing platform.

7.5 Ground Portable Radar for Non-Cooperative Traffic

Since 2014, the RAVEN project has worked with Seamatica Aerospace (SMA) for the use of their Zeus ground portable radar. As shown in Fig. 7.16, the Zeus radar is based on OEM hardware originally designed for airborne weather detection. It operates at X-band (permitting physically small and light-weight RF hardware to be employed) and makes exclusive use of solid state technology. The Zeus radar also uses long pulses with linear frequency modulation (LFM) pulse compression to increase the energy on target while maintaining a tight range resolution [14].

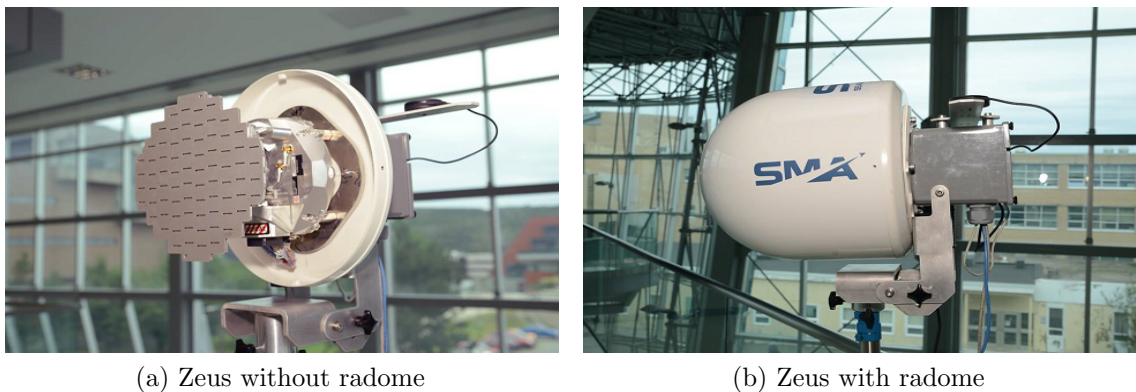


Figure 7.16: Zeus ground portable radar assembly [13].

Table 7.3 summarizes the key specifications of the Zeus hardware. It is noted that the selected pulse duration (coupled with internal processing delays) results in a blind range of approximately 0.5 nmi (an area within visual range). During target tracking, the antenna scan rate results in an average target update interval of 2.5 seconds, which is reasonable for a low-flying GA aircraft (altitude below 5000 feet).

Table 7.3: Zeus ground portable radar specifications and settings.

Parameter	Value
Centre Frequency	9375 MHz
Peak Transmit Power	40 W
Pulse Repetition Frequency (PRF)	3750 Hz
Pulse Duration	3.41 μ s
Pulse Bandwidth	4688 kHz
Antenna Gain	25.8 dBi
Antenna Half Power Beamwidth (HPBW)	9°
Antenna Scan Extents	$\pm 60^\circ$
Antenna Scan Rate	48°/sec
Antenna Tilt	+3°
Minimum Detectable Signal (PD = 0.7, PFA = 10^{-6})	-127 dBm

7.5.1 Test Procedure

To check the radar detection performance, a field flight test is performed at Witless Bay Line, NL as shown in Fig. 7.17. Seven flight plans are drawn in different colors on the map in Fig. 7.17, including three approaching maneuvers, three crossing maneuvers and a circular maneuver as listed in Table 7.4.

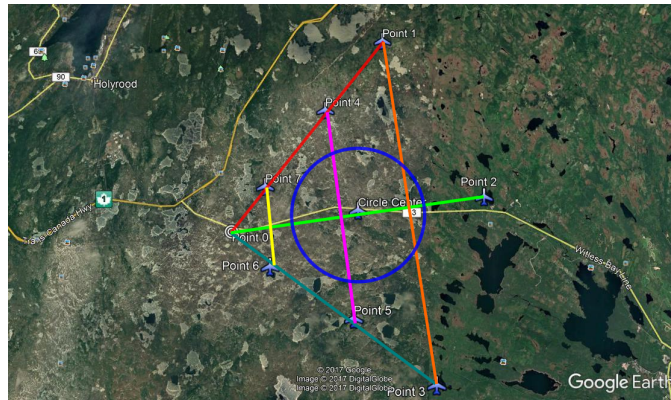


Figure 7.17: Witless Bay Line radar test flight plan on the map.

The traffic aircraft consists of a small, single engine float plane with a cruise airspeed of 120 kt at 2000 ft and a typical radar cross section (RCS) on the order of 1 m². The Zeus radar is installed at the Point 0 position on the map in Fig. 7.17 and

aligned with the road (i.e., the heading angle at 80°). In addition, a GPS recorder is placed in the aircraft to obtain GPS positions and tracks for analysis.

Table 7.4: Summary of radar test flight plan.

Flight No	Flight Plan	Track Heading	Track Color
1	Point 1 fly to Point 0	215°	Red
2	Point 2 fly to Point 0	260°	Green
3	Point 3 fly to Point 0	305°	Cyan
4	Point 3 fly to Point 1	350°	Orange
5	Point 4 fly to Point 5	170°	Magenta
6	Point 7 fly to Point 6	170°	Yellow
7	Circle (1.5 nmi radius)	N/A	Blue

7.5.2 Test Results

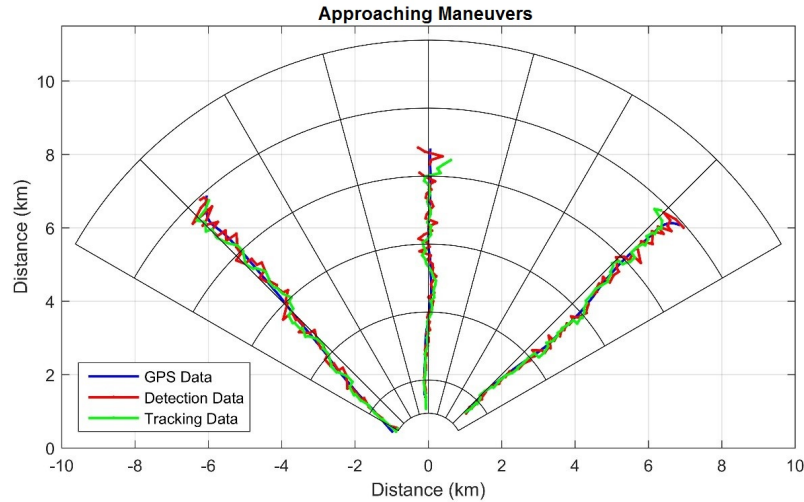


Figure 7.18: Results for the approaching maneuvers [14]. Distances are relative to the radar, bearings are relative to the 80° radar pointing angle, the range rings interval is 1 nmi and the scan spoke interval is 15° .

Results for the three approaching maneuvers are shown in Fig. 7.18. All of the results are plotted such that the range is taken to be relative to the radar location and the bearings are relative to 80° . In each approaching maneuver, three scans are

required to establish track, and track is maintained for the complete maneuver. There are only two instances of missed detections: one during Flight 2 (Point 2 fly to Point 0) at a range of approximately 4.2 nmi and another during Flight 3 (Point 3 fly to Point 0) at a range of 3.3 nmi. This suggests that the detection reliability is very high over these areas.

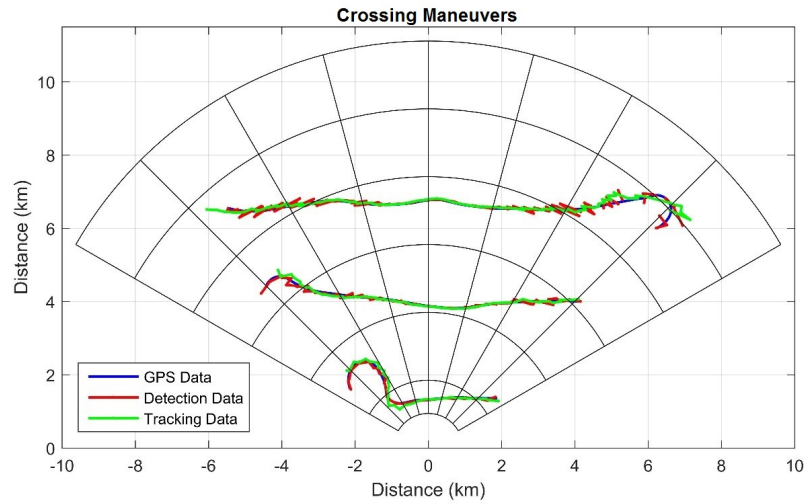


Figure 7.19: Results for the crossing maneuvers [14]. Distances are relative to the radar, bearings are relative to the 80° radar pointing angle, the range rings interval is 1 nmi and the scan spoke interval is 15° .

Similar results are obtained for the crossing maneuvers, as shown in Fig. 7.19. In particular, the two near paths exhibit perfect detection performance and strong tracking performance with minimal false tracks. However, the furthest path (Point 3 fly to Point 1) is found to exhibit reduced detection performance when the target range exceeds 4.5 nmi.

Finally, the results for the circular maneuver are shown in Fig.7.20. This data exhibits strong performance with no missed detections. Furthermore, track is maintained throughout the maneuver despite occasionally significant deviations in the detected target position relative to the GPS track.

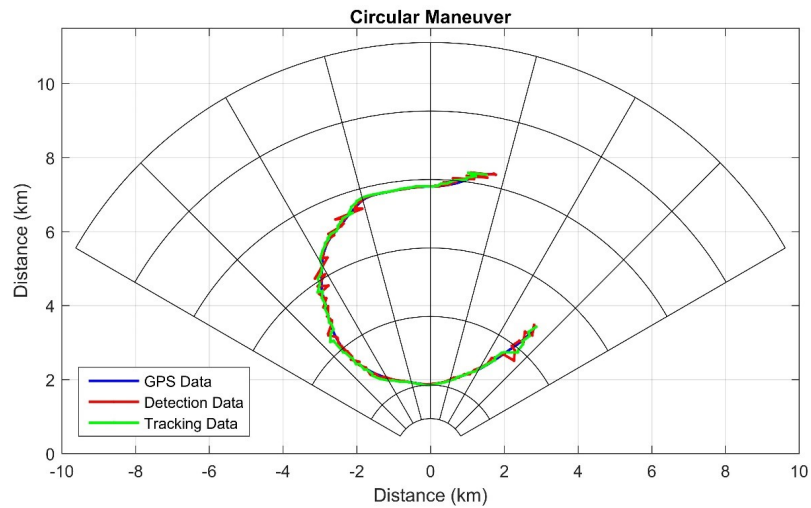


Figure 7.20: Results for the circular maneuver [14]. Distances are relative to the radar, bearings are relative to the 80° radar pointing angle, the range rings interval is 1 nmi and the scan spoke interval is 15° .

The detection and tracking performance of the Zeus radar system is tested against a representative GA target performing a variety of maneuvers over land clutter. Results indicate excellent detection reliability when the target is within 4.5 nmi. Approaching 5 nmi is found to result in drop in detection probability, which can most likely be attributed to multipath fading [14]. In summary, the test is successful and serves as a key step on the path to developing a practical ground portal radar system.

7.6 BVLOS Flight Tests

To fully research UAS operations in normal air traffic scenarios, the RAVEN UA have to be able to fly in a large airspace to simulate real air traffic. However, such flights are not allowed by the initial visual-range SFOC obtained from Transport Canada that governs RAVEN flight operations in the VLOS range, because extra safety features have to be installed on the UA to prevent the UA from flying away from the area assigned by the SFOC when UA fly out of the visual range of the EP. For example, in the RAVEN BVLOS SFOC application, extended communication links, a First-Person View (FPV) video system, a flight termination system (FTS) [40], and Geo-fence and Return-To-Launch (RTL) functions enabled in the autopilot are added to prove to Transport Canada that the RAVEN project has the capability to prevent the UA from flying-away during a BVLOS mission [41]. As a result, the RAVEN project is granted an SFOC for BVLOS flights over the ocean at the RAVEN test site in the Argentina area from Transport Canada as the red box region (3 nmi by 4 nmi) defined on the map in Fig. 7.21.

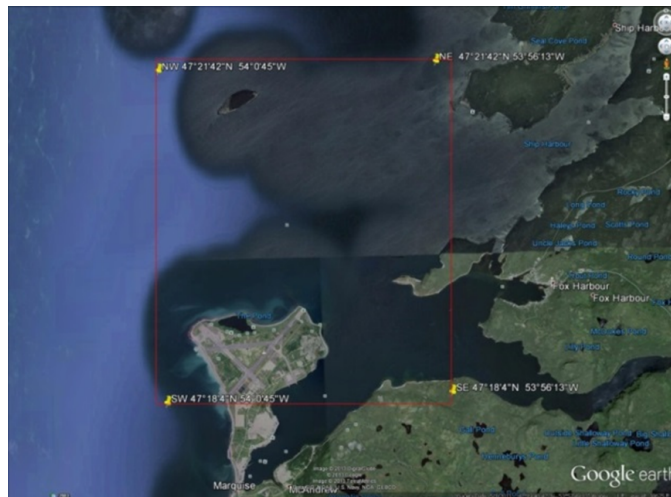


Figure 7.21: Map for the BVLOS operating area in Argentina, NL.

7.6.1 System Configuration for BVLOS UAS

As shown in Fig. 7.22, additional FTS and FPV systems are installed on the UA and integrated with its built-in autopilot and R/C control systems. Three RF links are used for BVLOS flights: a 900 MHz link is used for the communication between the UA autopilot and the GCS by the AVO; a 2.4 GHz link is used for R/C manual control by the EP; and a 5.8 GHz link is used for the real-time airborne video transmission by the EP and the AVO. The FTS checks the healthy status of the 900 MHz and 2.4 GHz links. If both links are lost for more than two minutes, the FTS will kill the engine to prevent the unmanned aircraft from flying away. At ranges beyond the visual range of the EP (approximately 0.25 nmi) and within the R/C link range (approximately 1 nmi), the FPV video system can help the EP control the aircraft to fly home (using manual R/C control) if the autopilot system fails. At ranges beyond the R/C link range, the FPV system allows the AVO to visually monitor the progress of the flight and the status of the onboard systems.

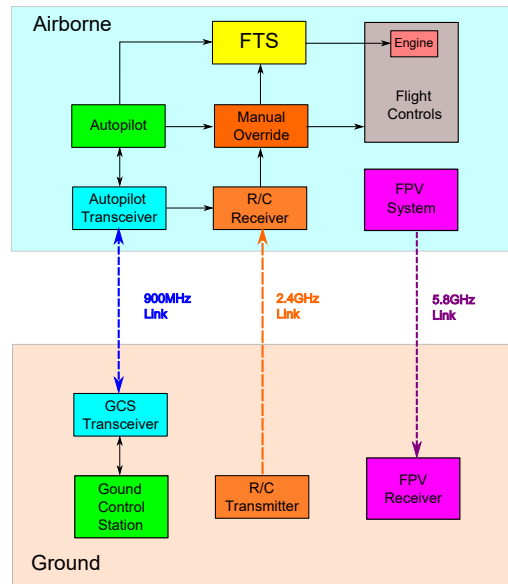


Figure 7.22: System configuration for BVLOS UAS.

7.6.2 Link-loss Failure Action Plan for BVLOS Flights

During BVLOS flights, link-loss failures are the main factors that might lead a UA to fly away. Table 7.5 describes how R/C, Autopilot (AP), and FPV link-loss failures are handled during BVLOS flights.

Table 7.5: Link-loss failure cases in BVLOS flights.

Case	R/C Link	AP Link	FPV Link	ACTION
Case 1	✓	✓	✓	<ul style="list-style-type: none"> • Mission continues; • Location of UA is known at all times via AP and FPV links.
Case 2	×	×	✓	<ul style="list-style-type: none"> • Timeout counter starts; • Location of UA is known at all times via FPV link; • During the timeout period UA should head back towards the launch location; if either the R/C or AP link is not regained, at end of the timeout period the engine is killed and the UA will impact the ground/water; • If during the timeout period a reliable R/C or AP link is regained, then the timeout counter is disabled and subsequent action is as per Case 5 or Case 7.
Case 3	×	×	×	<ul style="list-style-type: none"> • Timeout counter starts; • During the timeout period UA should head back towards the launch location; • If either the R/C or AP link is not regained, at end of the timeout period, the engine is killed and the UA will impact the ground/water; • If during the timeout period a reliable R/C or AP link is regained, then the timeout counter is disabled and subsequent action is as per Case 6 or Case 8.
Case 4	✓	✓	×	<ul style="list-style-type: none"> • Mission continues; • Location of UA is known at all times via AP link.
Case 5	×	✓	✓	<ul style="list-style-type: none"> • Mission continues; • Location of UA is known at all times via AP and FPV links; • At the end of the mission, UA is directed to landing point/safe area by uploading a new AP flight plan via AP link; • If the R/C link has not been regained when UA arrives at landing point, the engine is killed and the UA will impact the ground in a safe area; • If the R/C link has been regained when UA arrives at the landing point, EP lands UA under R/C control.
Case 6	×	✓	×	<ul style="list-style-type: none"> • Mission continues; • Location of UA is known at all times via AP link; • At the end of the mission, UA is directed to a landing point/safe area by uploading a new AP flight plan via AP link; • If the R/C link has not been regained when UA arrives at the landing point, the engine is killed and the UA will impact the ground in a safe area; • If the R/C link has been regained when UA arrives at the landing point, EP lands UA under R/C control.
Case 7	✓	×	✓	<ul style="list-style-type: none"> • UA should head back towards the launch location; • Location of UA is known at all times via FPV link; • When UA arrives at the pre-programmed safe area, EP takes R/C control and lands; • If UA is not heading in the correct direction, EP immediately takes R/C control and flies UA and lands.
Case 8	✓	×	×	<ul style="list-style-type: none"> • If UA is within visual range of the EP, then the EP takes R/C control and lands the UA in a safe area; • If EP is not successful or if UA is beyond visual range of the EP, the EP will shut off the R/C transmitter, thus inducing an R/C link failure. Then, the situation becomes the same as Case 3.

7.6.3 BVLOS Flights

As flight logs show in Fig. 7.23, BVLOS flights are conducted out and back from the take-off point on the runway to Fox Island in Placentia Bay, a distance of approximately 2.5 nmi each way. The cruise altitude achieved is approximately 1200 ft above MSL. During BVLOS flights, the UA can only be seen during the takeoff and landing at the runway area. Once the UA climb to above 800 ft, the EPs and AVOs have to rely on the AP and FPV links to monitor the attitude, position, and status of the UA at the GCS and control the UA to carry out the flight missions for the research on BVLOS flight operations, i.e., UA self-separation mitigation and collision avoidance mitigation for small UAS.



Figure 7.23: BVLOS flights at the RAVEN project test site in Argentia, NL.

In BVLOS flight operations, the EP is the Pilot-in-Command (PIC) for the UA during manual takeoff and landing, and the AVO is the PIC for the rest period of time during the autopilot flight (e.g., 55 minutes in a 60-minute BVLOS flight). In addition to continued monitoring of the attitude, position, and status of the UA at the GCS, the PIC/AVO should check the ACAS GUI for potential LoWCs or NMACs

during mid-air encounters. When LoWCs are predicted, the PIC/AVO needs to make maneuvering decisions for self-separation mitigation to avoid potential LoWCs. However, in consideration of wind effects on small UA level maneuvers, it is very difficult for the PIC/AVO to determine an appropriate mitigation solution in a short period of time (e.g., 30 seconds) to answer three fundamental questions “when to maneuver”, “how to maneuver”, and “how long for the maneuver”, according to the horizontal range, the detected relative bearing, the heading and the closing speed to the UA on the ACAS GUI. As a result, it is necessary to have a DAA guidance system to help the PIC/AVO reduce the workload and improve the mitigation performance during BVLOS flight operations. This indeed guides the research work carried out in Chapter 5 and Chapter 6.

7.7 Summary

Numerous VLOS and BVLOS UA flights are successfully carried out at the RAVEN test site in Argentinia, NL to test and validate the newly-developed ADS-B based cooperative ACAS for small UAS. During flight tests, the UA 4D synchronization control software and the ACAS HIL testing platform are also developed as required to facilitate the system functional testing work in the development of the ADS-B based cooperative ACAS. In addition, a ground portable radar test is performed at Witless Bay Line, NL to check the radar performance on detecting non-cooperative mid-air traffic nearby UAS operating areas.

The testing results and difficulties in the flight tests also direct the new theoretical approaches discussed in Chapter 4 - 6, i.e., the impact of wind effects on the WCAT/CAAT boundaries for small UAS in self-separation and collision avoidance, and a set of real-time DAA supervisory guidance for small UAS during mid-air encounters.

Chapter 8

Conclusion and Future Work

8.1 Contributions

This thesis develops a closed-loop simulation based evaluation and qualification environment with all the elements involved in the development of DAA systems for small UAS, and carries out the experimental work for DAA implementation and flight tests. Later, credited with lessons learned from the experimental work and the efficiency of the newly-developed fast-time simulation platform, three major contributions for hazard identification, risk assessment, and mitigation solution are designed, developed, modified and improved to provide real-time DAA mitigation guidance for small UAS with other traffic during mid-air encounters in civil airspace. As described in Fig. 8.1, the research work in this thesis is a creative and coherent combination of the incremental technological contributions based on theoretical foundations, such as dynamic programming, small UAS aerodynamics, supervised learning, data mining, discrete event system, and limited lookahead strategies. The core contribution “risk-based supervisory guidance for DAA involving small UAS” became the title of this thesis and can be summarized in the following sub-areas:

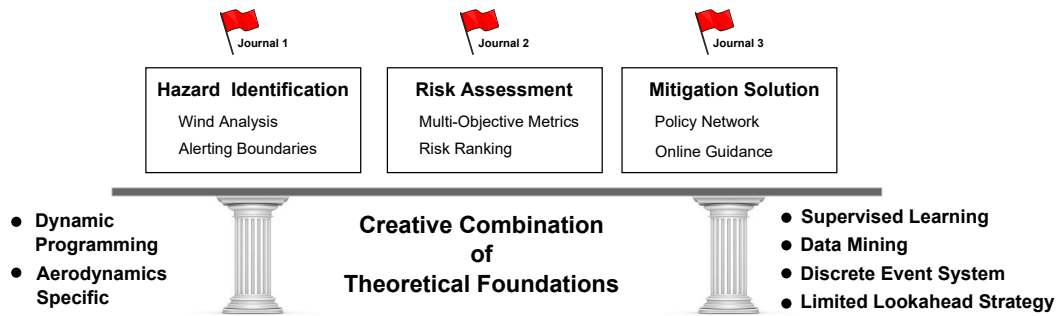


Figure 8.1: Diagram for three major contributions in this thesis.

8.1.1 Modelling

A series of mathematical models are designed in the thesis through Chapter 2 to Chapter 6 during the development of DAA modules for the fast-time simulation platform, i.e., the encounter generation model, the sensor measurement model, the target tracking model, the hazard identification model, the risk assessment model, the mitigation strategy model, as well as the performance evaluation model. Through these models, a closed-loop evaluation and qualification environment is constructed for DAA systems of small UAS, where mid-air encounters are simulated, traffic are detected and tracked, collision risks are assessed, mitigation maneuvers are suggested, and mitigation performance is analyzed and recorded for further analysis and investigation.

8.1.2 Analysis Platform

From Chapter 2 through to Chapter 6, the fast-time simulation-based analysis platform is developed to exercise encounter geometries, qualify the performance and reliability of mitigation solutions, and perform statistical analysis over millions of simulated mid-air encounters from a set of repeatable high-fidelity aircraft encounters in civil

airspace in a short period of time. The completion of this simulation platform reduces the turnaround time of the performance evaluation for DAA systems, facilitates the modifications and improvements of the newly-developed DAA systems, and helps them achieve the ultimate goal of an equivalent level of safety as human pilots on manned GA aircraft.

8.1.3 Situation Awareness

Wind effects are introduced in the mathematical analysis for hazard identification in Chapter 4 to determine the ever-changing outer and inner safety boundaries, i.e., WCAT and CAAT boundaries, in various wind conditions for small UAS in self-separation and collision avoidance. In addition, a set of time-based and range-based metrics, i.e., $P_{risk}(\tau_{mod})$, $P_{risk}(HMD)$, and $P_{risk}(V_s)$, are designed for risk assessment in Chapter 5 to evaluate encounter collision risks in real-time and provide normalized risk levels, i.e., $P_{risk}(Penetration)$, $P_{risk}(Range)$, and $P_{risk}(Collision)$, for oncoming air traffic during mid-air encounters. With a decision synthesis on both safety boundaries and collision risks, appropriate DAA mitigation enabling times are selected for small UAS to initiate maneuvers to avoid potential LoWCs or NMACs with other nearby traffic in civil airspace.

8.1.4 Mitigation Solutions

In Chapter 6, two types of mitigation solutions are designed and developed for small UAS to provide DAA maneuvering guidance during mid-air encounters; namely, self-separation solutions suggested by the learning-based SDTM, and collision avoidance solutions derived from the three-dimensional emergency evasive maneuvering algorithm. With millions of simulated mid-air encounters in civil airspace on the fast-time

simulation platform, these two mitigation solutions are tested, modified and qualified in Chapter 6 in numerous encounter geometries with various uncertainties on sensor measurements, wind effects and system delays.

8.1.5 Performance Ranking

For aircraft safety, the airworthiness of the UAS can be evaluated and certified by the existing standards and regulations for the manned GA aircraft, but for DAA systems, there are no standards and regulations provided by aviation authorities at present. Thus, a set of new analytical metrics, i.e.,

$RiskRatio_{ss}$ (*mitigated*), $RiskRatio_{ss}$ (*induced*), $RiskRatio_{ss}$ (*unresolved*),

$RiskRatio_{ca}$ (*mitigated*), $RiskRatio_{ca}$ (*induced*), and $RiskRatio_{ca}$ (*unresolved*),

are introduced for DAA systems in Chapter 6 to establish a performance ranking system for small UAS integration in civil airspace with manned GA aircraft. This performance ranking system will guide the researchers and system developers toward achieving the certification of newly developed DAA systems for small UAS, and help aviation authorities evaluate the risk levels of integrating small UAS in civil airspace.

8.1.6 Implementation and Flight Tests

The theoretical approaches achieved in the thesis are integrated into an effort of implementing DAA systems in Chapter 7 to provide a safe operation environment for small UAS in civil airspace. A ground portal radar system and an ADS-B based ACAS are developed and integrated (with the RAVEN team of which the author is a member) to provide the ability to detect both cooperative and non-cooperative traffic in the surveillance volume. During the system testing of the ACAS, a HIL simulator was designed and constructed for system ground tests and pilot training,

and a 4-dimensional (4D) encounter synchronization control system was also designed and developed for improving the efficiency of flight tests in the field.

8.2 Future Work

Future work could begin with further improvement of the knowledge base for SDTM decision making to cover more wind conditions, more traffic velocities, and more UA velocities in civil airspace, which will be an essential prerequisite for obtaining future approval for integrating small UAS into civil airspace. The current knowledge base was obtained from the MC simulation work carried out in Chapter 4 only for the UA operated at a 75 kt cruise speed in 20 kt gusty winds from eight wind directions, and the traffic operated at six cruise speeds with 50 kt increments from 50 kt to 300 kt. As a result, more MC simulations have to be carried out to improve the knowledge base for more accurate supervisory guidance in mid-air encounters.

The second item for future work could be to migrate the MC simulation computation platform from the centralized computing system (e.g., a single powerful computer system with an Intel Core-i7 CPU, 32 GB RAM and 256 GB SSD [135]) to the distributed computing system or cloud computing system (e.g., Amazon AWS, Microsoft Azure and Google Cloud Platform [136]) to have the planned MC simulations performed and completed in a short period of time, because current commercial cloud computing systems can scale resources elastically with the demand from MC simulations when needed, i.e., large amounts of data storage and compute time from an almost infinite pool of resources [137]. On the contrary, as an example, the knowledge base constructed in Chapter 4 took almost a month of computation time on the centralized computing system to run through all possible maneuvers to locate the least disruptive maneuvers for each of the simulated mid-air encounters. Moreover,

the supervised learning in Chapter 6 also required a significant amount of time (i.e., days) to form the policy network for maneuvering options because of range-querying operations from the database on the centralized computing system, which is another unquestioned reason to use cloud computing, rather than the current centralized computing, to carry out the future task of further improving the knowledge base for small UAS DAA guidance in mid-air encounters.

The third item for future work could be to research reinforcement learning (RL) methods to improve SDTM decision making through self-learning on successful mitigation solutions achieved by either the first choice of the SDTM or the preference of the PIC over millions of simulated mid-air encounters in civil airspace on the fast-time simulation platform. Similar to the SL knowledge base derived from the MC simulations, the successful mitigation solutions on the fast-time simulation platform will be sorted and saved in the RL knowledge base in the uniform distribution for each encounter scenario; namely, only one successful mitigation solution is selected as the maneuvering option based on the first choice of the SDTM or the preference of the PIC for each encounter case in the RL knowledge base. Later, the RL policy network could be generated and synthesized with the previously obtained SL policy network for the new SDTM to provide more adaptive guidance solutions in DAA decision making.

After the first three future works are completed and qualified on the fast-time simulation platform, as depicted in Fig. 8.2, the fourth item for future work could be to employ this fast-time simulation platform to determine the sensor requirements, i.e., minimal operational performance standards (MOPS) for detection sensors. Bruno Miranda Artacho, a Master's student in the RAVEN project, has employed the initially-developed fast-time simulation platform from this thesis to determine the radar detection range required for assisting small UAS in achieving an equivalent level of safety as manned aircraft in civil airspace. In the future, more sensor performance

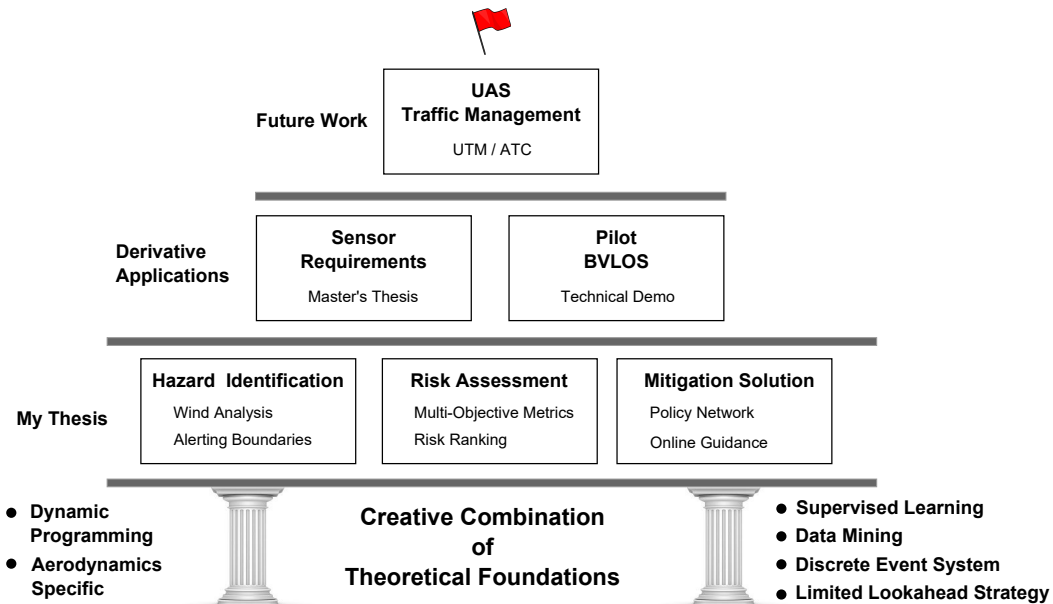


Figure 8.2: Diagram for future recommendations.

requirements on different parameters could be determined by the advanced fast-time simulation platform from this future work.

The fifth task for future work could be to implement the newly-developed SDTM into DAA systems to provide online supervisory guidance for small UAS in mid-air encounters. During the implementation of the RAVEN ACAS in Chapter 7, the UAS collision avoidance algorithm was implemented on the onboard microcontroller (i.e., TI TMS320C28343 microcontroller [138]). To implement both self-separation and collision avoidance mitigation algorithms into the next generation of small UAS DAA systems, a higher-performance processor platform should be chosen for the development, e.g., TI BeagleBone Black ARM Cortex-A8 platform with a TI real-time operating system (RTOS), 1GHz ARM Cortex-A8 processor, 512 MB RAM, and 4 GB flash storage [139]. In this case, for the SL and RL policy networks up to 150 MB obtained from the second and the third future work, they can be directly loaded into the system memory (RAM)

to provide online supervisory guidance in real-time regardless of database querying operations. In addition, the ACAS HIL testing platform developed in Chapter 7 can also be used to test and verify the performance of the new DAA systems on both software and hardware levels over a variety of encounter geometries.

The sixth task for future work could be to carry out the validation flight tests for the newly-developed small UAS DAA systems in the field. The initial flight tests can be performed at the RAVEN project test site in Argentia, NL; however, due to the RAVEN SFOC restriction on BVLOS flights, the true BVLOS flight tests could be held in a UAS test range (authorized by Transport Canada, e.g., the test range in Alma, QC) to comprehensively test and verify the system performance of the newly-developed small UAS DAA systems in a variety of encounter geometries as required.

The ultimate goal of this thesis has been added on the top of the research tree in Fig. 8.2. To implement the near-term solution of integrating small UAS into civil airspace, the current thesis could be extended for small UAS operations from a single GCS to a local ATC facility to help air traffic controllers manage small UAS air traffic at the level above 2000 ft with manned air traffic in the region. In the future, with more small UAS operational data obtained at low-altitude (e.g., below 400 ft [140]), more accurate small UAS encounter models could be developed for the future fast-time simulation platform, in turn, small UAS DAA systems could be further researched and tested on the future fast-time simulation platform for the UAS Traffic Management (UTM) environment proposed by the Federal Aviation Administration (FAA) and the National Aeronautics and Space Administration (NASA) [141].

Bibliography

- [1] Radio Technical Commission for Aeronautics (RTCA), “Minimum Operational Performance Standards (MOPS) for Air-to-Air Radar for Traffic Surveillance,” Document No: RTCA/DO-366, Washington, DC, RTCA, Inc., May 2017. xi, 48, 49
- [2] —, “Minimum Operational Performance Standards (MOPS) for Detect and Avoid (DAA) Systems,” Document No: RTCA/DO-365, Washington, DC, RTCA, Inc., May 2017. xi, xv, xvi, 3, 6, 7, 9, 23, 28, 47, 55, 56, 58, 74, 75, 76, 78, 79, 88, 100, 113, 120
- [3] G. Limnaios, N. Tsourveloudis, and K. P. Valavanis, *Sense and Avoid in UAS: Chapter 1 Introduction*. John Wiley & Sons, Ltd, 2012, pp. 1–34. [Online]. Available: <http://dx.doi.org/10.1002/9781119964049.ch1> xiii, 1, 2
- [4] “Air Surveillance Radar Tower (ASR-9),” Wiley|Wilson, Dec. 2017. [Online]. Available: <http://www.wileywilson.com/project/fort-lauderdale-air-surveillance-radar-tower-asr-9/> xiii, 15
- [5] D. De and P. K. Sahu, “A novel approach towards the designing of an antenna for aircraft collision avoidance system,” *AEU - International Journal of Electronics and Communications*, vol. 71, pp. 53–71, Jan. 2017. [Online]. Available: <http://www.sciencedirect.com/science/article/pii/S1434841116308056> xiii, 16

- [6] Federal Aviation Administration (FAA), “Introduction to TCAS II Version 7.1,” U.S. Department of Transportation, Tech. Rep., Feb. 2011. [Online]. Available: https://www.faa.gov/documentLibrary/media/Advisory_Circular/TCAS%20II%20V7.1%20Intro%20booklet.pdf xiii, 17
- [7] J. Zimmerman, “ADS-B 101: What It Is And Why You Should Care,” *Air Facts*, Jan. 2013. [Online]. Available: <http://airfactsjournal.com/2013/01/ads-b-101-what-it-is-and-why-you-should-care/> xiii, 18
- [8] A. Zeitlin, “Progress on Requirements and Standards for Sense & Avoid,” The MITRE Corporation, Tech. Rep., 2010. [Online]. Available: https://www.mitre.org/sites/default/files/pdf/10_2799.pdf xiii, 6, 24, 25
- [9] D. G. Hull, *Fundamentals of Airplane Flight Mechanics*. Springer-Verlag Berlin Heidelberg, 2007. xiii, 26
- [10] M. J. Kochenderfer, J. K. Kuchar, L. P. Espindle, and J. D. Griffith, “Uncorrelated encounter model of the national airspace system,” Massachusetts Institute of Technology, Lincoln Laboratory, Project Report ATC-345, 2008. [Online]. Available: http://www.ll.mit.edu/mission/aviation/publications/publication-files/atc-reports/Kochenderfer_2008_ATC-345_WW-18178.pdf xiii, 29, 30, 33
- [11] Y. Kosuge and T. Okada, “Bias estimation of two 3-dimensional radars using kalman filter,” in *Advanced Motion Control, 1996. AMC '96-MIE. Proceedings., 1996 4th International Workshop on*, vol. 1, Mar. 1996, pp. 377–382 vol.1. xiv, 41
- [12] W. A. A. M. Bierbooms, “Constrained stochastic simulation of wind gusts for wind turbine design,” Ph.D. dissertation, Delft University Wind Energy Research

- Institute, 2009. [Online]. Available: <https://repository.tudelft.nl/islandora/object/uuid:f1d17514-77c0-4ed1-88ff-c46a1006f66d?collection=research> xv, 66
- [13] “Zeus Radar System,” Seamatica Aerospace Limited, May 2016. [Online]. Available: <http://www.seamatica.ca/zeus-radar-system.html> xvii, 151
- [14] C. Rouse, “SEM SensorTECH Project: Zeus Radar Test Report,” Seamatica Aerospace Limited, Tech. Rep., 2016. xviii, 151, 153, 154, 155
- [15] R. Botzum, *50 Years of Target Drone Aircraft*. Northrop, Ventura Division, Aircraft Group, 1985. 1
- [16] P. Bergen and D. Rothenberg, *Drone Wars: Transforming Conflict, Law, and Policy*. New America Foundation, 2009. 1
- [17] T. Cox, C. Nagy, M. Skoog, and I. Somers, “Civil UAV Capabilities Assessment,” National Aeronautics and Space Administration, Tech. Rep., Dec. 2004. [Online]. Available: https://www.nasa.gov/centers/dryden/pdf/111761main_UAV_Capabilities_Assessment.pdf 1
- [18] G. Fasano, D. Accado, A. Moccia, and D. Moroney, “Sense and avoid for unmanned aircraft systems,” *IEEE Aerospace and Electronic Systems Magazine*, vol. 31, no. 11, pp. 82–110, 2016. 1, 2, 3
- [19] Federal Aviation Administration (FAA), “Sense and Avoid (SAA) for Unmanned Aircraft Systems (UAS),” FAA Sponsored Sense and Avoid Workshop, Tech. Rep., Nov. 2009. 2, 23
- [20] —, “Air Traffic Organization Policy, SUBJ: 5-2-9 UNMANNED AIRCRAFT SYSTEMS (UAS) LOST LINK,” Oct. 2016. [Online]. Avail-

able: https://www.faa.gov/documentLibrary/media/Notice/N_JO_7110.724.5-2-9_UAS_Lost_Link.pdf 3

- [21] Transport Canada (TC), “Staff Instruction,” Document No: SI 623-001, May 2017. [Online]. Available: <https://www.tc.gc.ca/eng/civilaviation/standards/general-recavi-uav-4161.html> 3
- [22] “Chapter 8 Monte Carlo Simulation,” Probabilistic Engineering Design, Mechanical & Aerospace Engineering, Missouri University of Science and Technology, Mar. 2017. [Online]. Available: http://web.mst.edu/~dux/repository/me360/me360_lecture8.html 5
- [23] Federal Aviation Administration (FAA), “Integration of Civil Unmanned Aircraft Systems (UAS) in the National Airspace System (NAS) Roadmap,” Nov. 2013. [Online]. Available: https://www.faa.gov/uas/media/uas_roadmap_2013.pdf 6
- [24] Radio Technical Commission for Aeronautics (RTCA), “SC-228, Minimum Operational Performance Standards for Unmanned Aircraft Systems,” Dec. 2017. [Online]. Available: <https://www.rtca.org/content/sc-228> 7
- [25] —, “SC-147, Traffic Alert & Collision Avoidance System (TCAS),” Dec. 2017. [Online]. Available: <https://www.rtca.org/content/sc-147> 7
- [26] C. Swider, “RTCA SC-228 & DAA standards development,” in *2014 Integrated Communications, Navigation and Surveillance Conference (ICNS) Conference Proceedings*, Apr. 2014, pp. 1–25. 7
- [27] S. P. Cook, D. Brooks, R. Cole, D. Hackenberg, and V. Raska, “Defining well clear for unmanned aircraft systems,” in *AIAA Infotech @ Aerospace*, ser. AIAA

- SciTech Forum. American Institute of Aeronautics and Astronautics, Jan. 2015. [Online]. Available: <https://doi.org/10.2514/6.2015-0481> 7
- [28] S. Baillie, W. Crowe, E. Edwards, and K. Ellis, “Small RPAS Best Practices for BVLOS,” Oct. 2016. [Online]. Available: <https://www.unmannedsystems.ca/download-usc-small-rpas-best-practices-document/> 9, 115
- [29] G. Manfredi and Y. Jestin, “An introduction to ACAS Xu and the challenges ahead,” in *2016 IEEE/AIAA 35th Digital Avionics Systems Conference (DASC)*, Sep. 2016, pp. 1–9. 9
- [30] M. P. Owen and M. J. Kochenderfer, “Dynamic logic selection for unmanned aircraft separation,” in *2016 IEEE/AIAA 35th Digital Avionics Systems Conference (DASC)*, Sep. 2016, pp. 1–8. 9
- [31] G. Manfredi, “ACAS Xu: Inside NUCLEUS,” RPAS CHAIR ENAC., Mar. 2017. 9
- [32] S. X. Fang, L. Rolland, and S. O’Young, “Mid-Air Collision Risk Assessment for Small UAS Detect-and-Avoid Systems,” *AIAA Journal of Air Transportation*, 2017 (Under Review). 11, 12
- [33] —, “Estimation of Minimum Alerting Boundaries in Winds for Small UAS Detect-and-Avoid Systems,” *AIAA Journal of Aerospace Information Systems*, 2017 (Accepted). 11, 12
- [34] —, “Online Risk-based Supervisory Maneuvering Guidance for Small UAS Detect-and-Avoid Systems,” *AIAA Journal of Guidance, Control, and Dynamics*, 2017 (Accepted). 11, 12

- [35] —, “Development and Implementation of ADS-B Based Cooperative Autonomous Collision Avoidance System,” in *Unmanned Systems Canada Conference, November 4-6, Montreal, QC*, Nov. 2014. 12, 144
- [36] S. X. Fang and S. O’Young, “ADS-B Based Cooperative Autonomous Collision Avoidance System (ACAS) Technical Report,” Raven Project, Memorial University of Newfoundland, Tech. Rep., Mar. 2014. 12, 144
- [37] S. X. Fang, D. Balage, M. V. Contarino, L. Rolland, and S. O’Young, “Development and Implementation of UAV 4D Synchronization Encounter Flights,” in *Unmanned Systems Canada Conference, November 3-5, Halifax, NS*, Nov. 2015. 12, 140
- [38] S. X. Fang and S. O’Young, “UAV 4-D Synchronization Technical Report ,” Raven Project, Memorial University of Newfoundland, Tech. Rep., Mar. 2014. 12, 140
- [39] S. X. Fang, L. Rolland, and S. O’Young, “Development of Small UAS Beyond-Visual-Line-of-Sight (BVLOS) Flight Operations: System Requirements and Procedures,” *Drones*, 2018 (Under Review). 12
- [40] S. X. Fang and S. O’Young, “Flight Termination System Technical Report,” Raven Project, Memorial University of Newfoundland, Tech. Rep., Mar. 2014. 12, 156
- [41] —, “Beyond Line of Sight (BLOS) Flight Mission Technical Report,” Raven Project, Memorial University of Newfoundland, Tech. Rep., Mar. 2014. 12, 156
- [42] A. Zeitlin, *Sense and Avoid in UAS: Chapter 2 Performance Tradeoffs and the Development of Standards*. John Wiley & Sons, Ltd, 2012, ch. 2, pp. 35–54.

- [Online]. Available: <http://dx.doi.org/10.1002/9781119964049.ch2> 14, 19, 24, 37, 124
- [43] European Organisation for the Safety of Air Navigation (EUROCONTROL), “Transponders in aviation,” May 2014. [Online]. Available: <https://www.eurocontrol.int/sites/default/files/publication/files/NetAlert-19.pdf> 15
- [44] J. J. Saia, M. L. Stone, and M. E. Weber, “A Description of the Interfaces between the Weather Systems Processor (WSP) and the Airport Surveillance Radar (ASR-9),” Massachusetts Institute of Technology, Lincoln Laboratory, Project Report ATC-259, 1997. [Online]. Available: https://www.ll.mit.edu/mission/aviation/publications/publication-files/atc-reports/Saia_1997_ATC-259_WW-15318.pdf 16
- [45] S. Henely, “TCAS II,” in *Digital Avionics Handbook, Second Edition - 2 Volume Set*, ser. Electrical Engineering Handbook. CRC Press, Dec. 2000. [Online]. Available: <http://dx.doi.org/10.1201/9781420036879.ch18> 16
- [46] J. Kuchar and A. Drumm, “The Traffic Alert and Collision Avoidance System,” *Lincoln Laboratory Journal*, vol. 16, no. 2, p. 277, 2007. 16
- [47] E. Williams, “Airborne Collision Avoidance System,” in *Proceedings of the 9th Australian Workshop on Safety Critical Systems and Software - Volume 47*, ser. SCS '04. Darlinghurst, Australia: Australian Computer Society, Inc., 2004, pp. 97–110. [Online]. Available: <http://dl.acm.org/citation.cfm?id=1082338.1082349> 16, 17
- [48] Federal Aviation Administration (FAA), “The Future of the NAS,” Jun. 2016. [Online]. Available: <https://www.faa.gov/nextgen/media/futureofthenas.pdf> 18

- [49] P. Duan, “ADS-B feasibility study for commercial space flight operations,” in *29th Digital Avionics Systems Conference*, Oct. 2010, pp. 3.A.1-1 – 3.A.1-11. 18
- [50] Radio Technical Commission for Aeronautics (RTCA), “Minimum Aviation System Performance Standards For Automatic Dependent Surveillance-Broadcast (ADS-B),” Document No: RTCA/DO-242A, Washington, DC, RTCA, Inc., Jun. 2002. 18
- [51] C. Zhao, J. Gu, J. Hu, Y. Lyu, and D. Wang, “Research on cooperative sense and avoid approaches based on ADS-B for unmanned aerial vehicle,” in *2016 IEEE Chinese Guidance, Navigation and Control Conference (CGNCC)*, Aug. 2016, pp. 1541–1546. 19
- [52] B. C. Karhoff, J. I. Limb, S. W. Oravsky, and A. D. Shephard, “Eyes in the Domestic Sky: An Assessment of Sense and Avoid Technology for the Army’s ”Warrior” Unmanned Aerial Vehicle,” in *2006 IEEE Systems and Information Engineering Design Symposium*, Apr. 2006, pp. 36–42. 19, 20
- [53] J. Utt, J. McCalmont, and M. Deschenes, “Development of a sense and avoid system,” in *Infotech@Aerospace*, ser. Infotech@Aerospace Conferences. American Institute of Aeronautics and Astronautics, Sep. 2005. [Online]. Available: <http://citeseerx.ist.psu.edu/viewdoc/download?doi=10.1.1.469.8012&rep=rep1&type=pdf> 19
- [54] L. Mejias, S. McNamara, J. Lai, and J. Ford, “Vision-based detection and tracking of aerial targets for uav collision avoidance,” in *2010 IEEE/RSJ International Conference on Intelligent Robots and Systems*, Oct. 2010, pp. 87–92. 19

- [55] G. Recchia, G. Fasano, D. Accardo, A. Moccia, and L. Paparone, “An Optical Flow Based Electro-Optical See-and-Avoid System for UAVs,” in *2007 IEEE Aerospace Conference*, Mar. 2007, pp. 1–9. 19
- [56] K. May and N. Krouglicof, “Moving target detection for sense and avoid using regional phase correlation,” in *2013 IEEE International Conference on Robotics and Automation*, May 2013, pp. 4767–4772. 19
- [57] D. Balage, G. Gamage, and S. O’Young, “EO/IR Non-Cooperative ACAS System Technical Report ,” Raven Project, Memorial University of Newfoundland, Tech. Rep., Mar. 2014. 19
- [58] C. Minwalla, P. Thomas, K. Ellis, R. Hornsey, and S. Jennings, “Range performance evaluation from the flight tests of a passive electro-optical aircraft detection sensor for unmanned aircraft systems,” *J. Unmanned Veh. Sys.*, vol. 4, no. 2, pp. 96–114, Feb. 2016. [Online]. Available: <http://dx.doi.org/10.1139/juvs-2014-0022> 19, 20
- [59] G. Koretsky, J. Nicoll, and M. Taylor, “A Tutorial on Electro-Optical/Infrared (EO/IR) Theory and Systems,” Institute for Defense Analysis, Jan. 2013, IDA Doc. D-4642. [Online]. Available: https://www.ida.org/idamedia/Corporate/Files/Publications/IDA_Documents/SED/ida-document-d-4642.pdf 20
- [60] T. Milkie, “Passive Acoustic Non-cooperative Collision Alert System (PANCAS) for UAV Sense and Avoid,” Dec. 2006, SARA, Inc. [Online]. Available: http://www.sara.com/ISR/acoustic_sensing/LOSAS.html 20
- [61] B. Harvey and S. O’Young, “Detection of continuous ground-based acoustic sources via unmanned aerial vehicles,” *J. Unmanned Veh. Sys.*, vol. 4, no. 2, pp.

83–95, Oct. 2015. [Online]. Available: <http://dx.doi.org/10.1139/juvs-2015-0029>
20

- [62] M. Devi, N. R. Dhabale, and Devishree, “Active and passive radar-location systems for the calculation of coordinates,” in *2017 International Conference on Innovative Mechanisms for Industry Applications (ICIMIA)*, Feb. 2017, pp. 770–773. 21
- [63] M. Skolnik, “Opportunities in radar-2002,” *Electronics Communication Engineering Journal*, vol. 14, no. 6, pp. 263–272, Dec. 2002. 21
- [64] C. Geyer, S. Singh, and L. Chamberlain, “Avoiding Collisions Between Aircraft: State of the Art and Requirements for UAVs operating in Civilian Airspace,” Jan. 2008, Robotics Institute, Carnegie Mellon University. [Online]. Available: <https://pdfs.semanticscholar.org/dff4/8511be1c9224c78bef8ee1ea090d59ea8fb4.pdf> 21
- [65] Federal Aviation Administration (FAA), “Memorandum of Agreement: For Industry Access to Aircraft Situation Display and National Airspace System Status Information Data,” Jul. 2014. [Online]. Available: http://www.fly.faa.gov/ASDI/asdidocs/ASDI_MOA_Ver_1.4a.pdf 21
- [66] R. Sabatini, A. Gardi, and M. A. Richardson, “LIDAR Obstacle Warning and Avoidance System for Unmanned Aircraft,” *International Journal of Mechanical, Aerospace, Industrial and Mechatronics Engineering*, vol. 8, no. 4, 2014. [Online]. Available: <http://waset.org/publications/9997995/lidar-obstacle-warning-and-avoidance-system-for-unmanned-aircraft> 21
- [67] S. Ramasamy, R. Sabatini, A. Gardi, and J. Liu, “LIDAR obstacle warning and avoidance system for unmanned aerial vehicle sense-and-avoid,” *Aerospace*

Science and Technology, vol. 55, pp. 344–358, Aug. 2016. [Online]. Available: <http://www.sciencedirect.com/science/article/pii/S1270963816301900> 21

- [68] R. Weibel, M. Edwards, and C. Fernandes, “Establishing a risk-based separation standard for unmanned aircraft self separation,” in *11th AIAA Aviation Technology, Integration, and Operations (ATIO) Conference*, ser. Aviation Technology, Integration, and Operations (ATIO) Conferences. American Institute of Aeronautics and Astronautics, Sep. 2011. [Online]. Available: <http://dx.doi.org/10.2514/6.2011-6921> 23
- [69] M. Johnson, E. R. Mueller, and C. Santiago, “Characteristics of a well clear definition and alerting criteria for encounters between uas and manned aircraft in class e airspace,” Eleventh USA/Europe Air Traffic Management Research and Development Seminar (ATM2015), 2015. [Online]. Available: http://www.atmseminar.org/seminarContent/seminar11/papers/388-Johnson_0123150804-Final-Paper-5-6-15.pdf 24
- [70] E. Theunissen, B. Suarez, and M. U. de Haag, “The impact of a quantitative specification of a well clear boundary on pilot displays for self separation,” in *2014 Integrated Communications, Navigation and Surveillance Conference (ICNS) Conference Proceedings*, Apr. 2014, pp. F2–1–F2–11. 24
- [71] E. Theunissen, M. U. de Haag, B. Suarez, and T. Kotegawa, “Refinement of a conflict probe algorithm and display to support well clear: Concept and implementation,” in *2014 IEEE/AIAA 33rd Digital Avionics Systems Conference (DASC)*, Oct. 2014, pp. 6A5–1–6A5–11. 24
- [72] S. M. Lee, C. Park, M. A. Johnson, and E. R. Mueller, “Investigating effects of well clear definitions on uas sense-and-avoid operations in enroute and transition

airspace,” in *2013 Aviation Technology, Integration, and Operations Conference*, ser. AIAA AVIATION Forum. American Institute of Aeronautics and Astronautics, 2013. [Online]. Available: <http://dx.doi.org/10.2514/6.2013-4308> 27

[73] Radio Technical Commission for Aeronautics (RTCA), “Minimum Operational Performance Standards (MOPS) for Traffic Alert and Collision Avoidance System II (TCAS II) Hybrid Surveillance,” Document No: RTCA/DO-300, Washington, DC, RTCA, Inc., Dec. 2006. 27

[74] D. H. Eberly, *3D Game Engine Design: A Practical Approach to Real-Time Computer Graphics*. Morgan Kaufmann, 2000. 28

[75] M. J. Kochenderfer, L. P. Espindle, J. K. Kuchar, and J. D. Griffith, “Correlated encounter model for cooperative aircraft in the national airspace system,” Massachusetts Institute of Technology, Lincoln Laboratory, Project Report ATC-344, 2008. [Online]. Available: http://www.ll.mit.edu/mission/aviation/publications/publication-files/atc-reports/Kochenderfer_2008_ATC-344_WW-18099.pdf 29

[76] A. J. Weinert, E. P. Harkleroad, J. D. Griffith, M. W. Edwards, and M. J. Kochenderfer, “Uncorrelated encounter model of the national airspace system version 2.0,” Massachusetts Institute of Technology, Lincoln Laboratory, Project Report ATC-404, 2013. [Online]. Available: <http://www.dtic.mil/cgi-bin/GetTRDoc?AD=ADA589697> 29, 33

[77] Z. Wang, R. Schultz, and F. Martel, “Reliability assessment of mid-air collision avoidance system for unmanned aircraft systems,” in *AIAA Infotech@Aerospace Conferences*, 2010. [Online]. Available: <http://dx.doi.org/10.2514/6.2010-3458> 32

- [78] “Geographic information systems,” Stack Exchange, Apr. 2017. [Online]. Available: <https://gis.stackexchange.com/questions/75528/understanding-terms-in-length-of-degree-formula> 39, 40
- [79] L. M. Bugayevskiy and J. P. Snyder, *Map projections : a reference manual*. London ; Bristol, PA: Taylor & Francis, 1995. 39, 40
- [80] J. P. Snyder, “Map projections: A working manual,” U.S. Government Printing Office, Washington, D.C., Tech. Rep., 1987. [Online]. Available: <http://pubs.er.usgs.gov/publication/pp1395> 39, 40
- [81] S. Zollo and B. Ristic, “On polar and versus Cartesian coordinates for target tracking,” in *Signal Processing and Its Applications, 1999. ISSPA '99. Proceedings of the Fifth International Symposium on*, vol. 2, 1999, pp. 499–502 vol.2. 40
- [82] “Object tracking using a Kalman filter (MATLAB),” May 2011. [Online]. Available: <https://blog.cordiner.net/2011/05/03/object-tracking-using-a-kalman-filter-matlab/> 42
- [83] M. O. Duffield, “Automatic Dependent Surveillance-Broadcast for Detect and Avoid on Small Unmanned Aircraft,” Master’s thesis, Brigham Young University, 2016. 42, 43
- [84] W. I. Tam, “Tracking Filters for Radar Systems,” Master’s thesis, University of Toronto, 1997. 42, 43
- [85] V. V. Uchaikin and V. M. Zolotarev, *Chance and Stability: Stable Distributions and their Applications*. Zeist, Netherland: VSP Science, 1999. 46

- [86] H. Tuo and H. Zhang, "Alerting Threshold Analysis of TCAS," *The Open Automation and Control Systems Journal*, no. 7, pp. 727–733, Jan. 2015. 46
- [87] R. A. Paielli and H. Erzberger, "Conflict probability estimation for free flight," *Journal of Guidance, Control, and Dynamics*, vol. 20, no. 3, pp. 588–596, May 1997. [Online]. Available: <http://dx.doi.org/10.2514/2.4081> 46, 74
- [88] S. Calhoun, W. Adams, and S. Smearcheck, "Special Committee (SC)-228 Alerting Analysis," CAL Analytics and RTCA, Nov. 2015, Case # 88ABW-2015-5596. 47
- [89] "Measurements and Error Analysis," the University of North Carolina at Chapel Hill, May 2017. [Online]. Available: http://www.webassign.net/question_assets/unccolphysmechl1/measurements/manual.html 48
- [90] US Department of Defense (DoD), "Global Positioning System Standard Positioning Service Performance Standard," Sep. 2008. 48
- [91] Federal Aviation Administration (FAA), "FAR 43 - Appendix E Altimeter System Test and Inspection," Sep. 2017. [Online]. Available: <http://www.faa-aircraft-certification.com/43-appendix-e.html> 48
- [92] Federal Aviation Administration (FAA) , "Code of Federal Regulations Part 23 - Airworthiness Standards: Normal, Utility, Acrobatic, and Commuter Category Airplanes," 1996. 50
- [93] J. Asmat, B. Rhodes, J. Umansky, C. Villavicencio, A. Yunas, G. Donohue, and A. Lacher, "Uas safety: Unmanned aerial collision avoidance system (ucas)," in *2006 IEEE Systems and Information Engineering Design Symposium*, Apr. 2006, pp. 43–49. 54

- [94] A. R. Lacher, D. R. Maroney, and A. D. Zeitlin, “Unmanned aircraft collision avoidance technology assessment and evaluation methods,” in *The 7th Air Traffic Management Research & Development Seminar*, 2007, pp. 1–10. 54
- [95] M. Gariel, F. Kunzi, and R. J. Hansman, “An algorithm for conflict detection in dense traffic using ads-b,” in *2011 IEEE/AIAA 30th Digital Avionics Systems Conference*, Oct. 2011, pp. 4E3–1–4E3–12. 61
- [96] E. Theunissen, B. Suarez, and F. Kunzi, “Well clear recovery for detect and avoid,” in *2016 IEEE/AIAA 35th Digital Avionics Systems Conference (DASC)*, Sep. 2016, pp. 1–10. 61
- [97] S. Vaidya and T. Khot, “Analysis of the tau concept used in aircraft collision avoidance through kinematic simulations,” in *2017 9th International Conference on Communication Systems and Networks (COMSNETS)*, Jan. 2017, pp. 431–436. 61
- [98] S. M. McGovern, S. B. Cohen, M. Truong, and G. Fairley, “Kinematics-based model for stochastic simulation of aircraft operating in the national airspace system,” in *2007 IEEE/AIAA 26th Digital Avionics Systems Conference*, 2007, pp. 3.B.2–1–3.B.2–11. 61
- [99] R. Bellman, *Dynamic programming*. Princeton University Press, 1957. 63
- [100] R. Robinett, D. Wilson, G. Eisler, and J. Hurtado, *Applied Dynamic Programming for Optimization of Dynamical Systems*. Society for Industrial and Applied Mathematics, Jan. 2005. [Online]. Available: <https://doi.org/10.1137/1.9780898718676> 63

- [101] C. Muñoz, A. Narkawicz, G. Hagen, J. Upchurch, A. Dutle, M. Consiglio, and J. Chamberlain, “Daidalus: Detect and avoid alerting logic for unmanned systems,” in *2015 IEEE/AIAA 34th Digital Avionics Systems Conference (DASC)*, Sep. 2015, pp. 5A1–1–5A1–12. 63, 104
- [102] “SQLite — Most Widely Deployed and Used Database Engine,” Hipp, Wyrick & Company, Inc. (HWACI), Oct. 2017. [Online]. Available: <https://www.sqlite.org/mostdeployed.html> 65
- [103] T. Lauderdale, “Probabilistic conflict detection for robust detection and resolution,” in *12th AIAA Aviation Technology, Integration, and Operations (ATIO) Conference and 14th AIAA/ISSMO Multidisciplinary Analysis and Optimization Conference*, ser. Aviation Technology, Integration, and Operations (ATIO) Conferences. American Institute of Aeronautics and Astronautics, Sep. 2012. [Online]. Available: <https://doi.org/10.2514/6.2012-5643> 74
- [104] C. E. van Daalen and T. Jones, “Fast conflict detection using probability flow,” *Automatica*, vol. 45, no. 8, pp. 1903–1909, 2009. [Online]. Available: <http://www.sciencedirect.com/science/article/pii/S000510980900209X> 74
- [105] A. Lambert, D. Gruyer, and G. S. Pierre, “A fast Monte Carlo algorithm for collision probability estimation,” in *2008 10th International Conference on Control, Automation, Robotics and Vision*, 2008, pp. 406–411. 74
- [106] A. Houénou, P. Bonnifait, and V. Cherfaoui, “Risk Assessment for Collision Avoidance Systems,” in *17th International IEEE Conference on Intelligent Transportation Systems (ITSC)*, 2014, pp. 386–391. 74
- [107] Y.-J. Chiang, J. T. Klosowski, C. Lee, and J. S. B. Mitchell, “Geometric algorithms for conflict detection/resolution in air traffic management,” in *Proceedings*

- of the 36th IEEE Conference on Decision and Control, vol. 2, Dec. 1997, pp. 1835–1840 vol.2. 74
- [108] A. Geser and C. Munoz, “A geometric approach to strategic conflict detection and resolution [atc],” in *Proceedings. The 21st Digital Avionics Systems Conference*, vol. 1, Oct. 2002, pp. 6B1–1–6B1–11 vol.1. 74
- [109] C. Santiago and E. R. Mueller, “Pilot Evaluation of a UAS Detect-and-Avoid Systems Effectiveness in Remaining Well Clear,” Aviation Systems Division, NASA Ames Research Center, Moffett Field, CA, USA, 2016. [Online]. Available: <http://techport.nasa.gov/file/6581> 74
- [110] J. Kay, E. Pratt, C. Santiago, and J. Warren, “Well Clear Penetration Severity Metrics Status Updates,” RTCA Workspace, Mar. 2016. 75
- [111] J. Kay and E. Pratt, “Severity of Loss of Well Clear,” RTCA Workspace, Mar. 2016. 78, 79
- [112] E. Theunissen, F. Kunzi, and B. Suarez, “Designing a robust detect and avoid alerting function,” in *2017 Integrated Communications, Navigation and Surveillance Conference (ICNS)*, Apr. 2017, pp. 3B3–1–3B3–10. 81
- [113] T. Rasche, “Prevention of Vehicle Interaction Collisions,” Hands-on Proximity Detection and Collision Avoidance Systems Workshop, 2010. [Online]. Available: <http://www.sacea.org.za/docs/Tilman-Rasche-prevention-of-vehicle-interaction-collisions.pdf> 84
- [114] J. K. Kuchar and L. C. Yang, “A review of conflict detection and resolution modeling methods,” *IEEE Transactions on Intelligent Transportation Systems*, vol. 1, no. 4, pp. 179–189, Dec 2000. 100

- [115] B. M. Albaker and N. A. Rahim, “A survey of collision avoidance approaches for unmanned aerial vehicles,” in *2009 International Conference for Technical Postgraduates (TECHPOS)*, Dec. 2009, pp. 1–7. 100
- [116] B. D. Carpenter and J. K. Kuchar, “A Probability-Base Alerting Logic for Aircraft on Parallel Approach,” Massachusetts Inst. of Tech.; Cambridge, MA United States, Tech. Rep., Apr. 1997, nASA-CR-201685. 100
- [117] M. C. Waller and C. H. Scanlon, Eds., *Proceedings of the NASA Workshop on Flight Deck Centered Parallel Runway Approaches in Instrument Meteorological Conditions*. NASA Langley Research Center; Hampton, VA United States, Dec. 1996, document ID: 19970011096. 100
- [118] R. Irvine, “The GEARS conflict resolution algorithm,” in *AIAA Guidance, Navigation, and Control Conference*, Boston, MA, Aug. 1998, pp. 786–796, aIAA-98-4236. 100
- [119] K. Bilimoria, H. Lee, Z.-H. Mao, and E. Feron, “Comparison of centralized and decentralized conflict resolution strategies for multiple-aircraft problems,” in *18th Applied Aerodynamics Conference*, ser. Fluid Dynamics and Co-located Conferences. American Institute of Aeronautics and Astronautics, Aug. 2000. [Online]. Available: <https://doi.org/10.2514/6.2000-4268> 100
- [120] L. Sun, J. D. Hedengren, and R. W. Beard, “Optimal trajectory generation using model predictive control for aerially towed cable systems,” *Journal of Guidance, Control, and Dynamics*, vol. 37, no. 2, pp. 525–539, Feb. 2014. [Online]. Available: <https://doi.org/10.2514/1.60820> 100
- [121] E. R. Mueller and M. Kochenderfer, “Multi-rotor aircraft collision avoidance using partially observable markov decision processes,” in *AIAA Modeling and*

- Simulation Technologies Conference*, ser. AIAA AVIATION Forum. American Institute of Aeronautics and Astronautics, Jun. 2016. [Online]. Available: <https://doi.org/10.2514/6.2016-3673> 100
- [122] Radio Technical Commission for Aeronautics (RTCA), “Minimum Operational Performance Standards for Traffic Alert and Collision avoidance System II (TCAS II),” Document No: RTCA/DO-185B, Washington, DC, RTCA, Inc., Jun. 2008. 100
- [123] E. Gibney, “Google AI algorithm masters ancient game of Go,” *Nature*, vol. 529, pp. 445–446, Jan. 2016. [Online]. Available: https://ai.arizona.edu/sites/ai/files/resources/gibney_2016_google_masters_go.pdf 101
- [124] D. Silver, A. Huang, C. J. Maddison, A. Guez, L. Sifre, G. van den Driessche, J. Schrittwieser, I. Antonoglou, V. Panneershelvam, M. Lanctot, S. Dieleman, D. Grewe, J. Nham, N. Kalchbrenner, I. Sutskever, T. Lillicrap, M. Leach, K. Kavukcuoglu, T. Graepel, and D. Hassabis, “Mastering the game of go with deep neural networks and tree search,” *Nature*, vol. 529, no. 7587, pp. 484–489, Jan. 2016. [Online]. Available: <http://dx.doi.org/10.1038/nature16961> 101
- [125] J. P. Millan, “Online discrete event control of hybrid systems,” phdthesis, Memorial University of Newfoundland, Oct. 2006. 112
- [126] K. Wackwitz and H. Boedecker, “Safety risk assessment for uav operation,” Drone Industry Insights — Safe Airspace Integration Project, Part One, Nov. 2015. [Online]. Available: <http://www.sarahnilsson.org/app/download/965208764/Safety-Risk-Assessment-for-UAV-Operation-Rev.-1.1.compressed.pdf> 120, 123
- [127] W. W. LaMorte, “Risk Ratios and Rate Ratios (Relative Risk),” Measures of Association, Boston University School of Public Health, Jun.

2016. [Online]. Available: http://sphweb.bumc.bu.edu/otlt/mph-modules/ep/ep713_association/ep713_association3.html 120
- [128] D. M. Asmar and M. J. Kochenderfer, "Optimized airborne collision avoidance in mixed equipage environments," Massachusetts Institute of Technology, Lincoln Laboratory, Project Report ATC-408, 2013. [Online]. Available: http://www.ll.mit.edu/mission/aviation/publications/publication-files/atc-reports/Asmar_2013_ATC-408_WW-26778.pdf 120
- [129] ArduPilot, "Archived:APM 2.5 and 2.6 Overview," Aug. 2017. [Online]. Available: <http://ardupilot.org/plane/docs/common-apm25-and-26-overview.html> 137
- [130] M. Tranchitella, S. Fujikawa, T. L. Ng, D. Yoel, D. Tatum, P. Roy, C. Mazel, S. Herwitz, and E. Hinkley, "Using Tactical Unmanned Aerial Systems to Monitor and Map Wildfires ," Jun. 2006. 138
- [131] MicroPilot, "MP2128 LRC2 MP2128 HELI-LRC2," Aug. 2017. [Online]. Available: <https://www.micropilot.com/products-mp2128lrc.htm> 138
- [132] D. Valyou, Z. Gibbons, S. Dhaniyala, and P. Marzocca, "Flight control, Data Acquisition, and Payload Integration for An Aerosol Sampling Unmanned Aerial Vehicle," Aug. 2017. 138
- [133] "FlightGear Flight Simulator," Dec. 2017. [Online]. Available: <http://www.flightgear.org/> 148
- [134] MicroSoft, "DateTime.Ticks Property," Aug. 2017. [Online]. Available: <https://msdn.microsoft.com/en-us/library/system.datetime.ticks.aspx> 150

- [135] O. Bastounis, “The 9 best computers of 2017: the best PCs ranked,” Aug. 2017. [Online]. Available: <http://www.techradar.com/news/computing/pc/10-of-the-best-desktop-pcs-of-2015-1304391> 165
- [136] M. Finnegan and S. Carey, “AWS vs Azure vs Google: What’s the best cloud platform for the enterprise?” Aug. 2017. [Online]. Available: <http://www.computerworlduk.com/it-vendors/microsoft-azure-vs-amazon-aws-public-cloud-comparison-which-cloud-is-best-for-enterprise-3624848/> 165
- [137] H. Wang, Y. Ma, G. Pratz, and L. Xing, “Toward Real-Time Monte Carlo Simulation Using a Commercial Cloud Computing Infrastructure,” *Physics in medicine and biology*, vol. 56, no. 17, pp. N175–N181, Aug. 2011. [Online]. Available: <http://www.ncbi.nlm.nih.gov/pmc/articles/PMC3431188/> 165
- [138] Texas Instruments (TI), “TMS320C28343 Delfino Microcontroller,” Aug. 2017. [Online]. Available: <http://www.ti.com/product/TMS320C28343> 167
- [139] —, “BeagleBone Black Development Board,” Aug. 2017. [Online]. Available: <http://www.ti.com/tool/BEAGLEBK> 167
- [140] P. Kopardekar and S. Bradford, “UAS Traffic Management (UTM) Research Transition Team (RTT) Plan,” NASA Ames Research Center, Tech. Rep., Jan. 2017. [Online]. Available: https://www.faa.gov/uas/research/utm/media/FAA_NASA_UAS_Traffic_Management_Research_Plan.pdf 168
- [141] T. Prevot, J. Rios, P. Kopardekar, J. E. Robinson III, M. Johnson, and J. Jung, “UAS Traffic Management (UTM) Concept of Operations to Safely Enable Low Altitude Flight Operations,” in *16th AIAA Aviation Technology, Integration, and Operations Conference*, ser. AIAA AVIATION

Forum. American Institute of Aeronautics and Astronautics, Jun. 2016.
[Online]. Available: <https://doi.org/10.2514/6.2016-3292> 168